Lateral and Vertical Nanoelectronic Devices Using Chemical Vapour Deposition Grown 2D Materials

Yingqiu Zhou

Supervised by Professor Jamie H. Warner

Department of Materials

Linacre College

University of Oxford

A thesis submitted for the degree of

Doctor of Philosophy

Declaration

The material contained within this thesis has not previously been submitted for a degree at the University of Oxford or any other university. The research reported within this thesis has been conducted by the author unless indicated otherwise.

Copyright Notice

Abstract

Lateral and Vertical Nanoelectronic Devices Using Chemical Vapor Deposition Grown 2D Materials

By Yingqiu Zhou

Linacre College

In pursuit of DPhil Degree, Trinity Term, 2018

In this thesis, field effect transistors (FETs), tunnel barrier transistors (TBTs), and photodetector based on monolayer and bilayer molybdenum disulphide (MoS_2) and tungsten disulphide (WS_2) 2D crystals, all synthesized using the bottom-up and scalable approach of chemical vapour deposition method (CVD), are studied. The devices are investigated in both lateral devices and vertical device configurations.

The first chapter of results probes the changes in FET performance at the grain boundaries (GBs) of WS_2 crystals, which are intrinsically formed during material growth and correlates it to the photoluminescence spectroscopy (PL) and Kevin Probe Microscopy (KPM) results. Nanoelectronic FETs are fabricated in pristine area, parallel to GBs, as well as perpendicular to GBs in order to understand the impact of GBs on the charge transport characteristics. The threshold voltage, which is a key FET variable is observed to shift towards the negative direction when a GB is parallel to the conductive channel compared with that of devices based on pristine WS_2, demonstrating that along the GB, the electronic properties are distinct and this causes modulation in the intrinsic FET behaviour.

The second chapter of results explores the use of graphene electrodes with a unique vertical stacked cross bar geometry. WS_2 is employed as the semiconducting photoactive layer sandwiched between two graphene electrodes to form vertical TBTs that also acts as photodetectors. The photo-generated charge carriers in WS_2 tunnel to top and bottom graphene electrodes with different probabilities, resulting in a net photocurrent. Increasing the thickness of WS_2 from monolayer to bilayer in the graphene/WS_2/graphene vertical devices leads to strong photovoltaic behaviour, which is observed due to the long lifetime of the interlayer exciton formed in photo-active bilayer as opposed to monolayer WS_2.

The third chapter of results demonstrates mixed heterobilayer (MoS_2:WS_2) stacks for vertical TBTs. In order to enhance the photovoltaic effect observed in the previous chapter in vertical devices, the bilayer photo-active WS_2 layer is substituted by MoS_2/WS_2. An atomic sharp type-II band alignment formed between the MoS_2/WS_2 interface is found to facilitate the formation of interlayer excitons with long lifetime through charge separation, which is understood to enhance strong photovoltaic effect. By reversing the MoS_2:WS_2 stack direction the direction of the photocurrent is observed to be dictated by the type-II interface rather than the differences in the magnitude of the tunnel barriers at the graphene interfaces.

Acknowledgements

First, I would like to thank my supervisor, Professor Jamie H Warner for giving me the opportunity to do research and providing invaluable guidance throughout my research. He taught me how to carry out researches, how to present research works clearly and encouraged me to overcome difficulties. Without his continuous optimism concerning this work, enthusiasm, encouragement and support, this study cannot be completed.

I also want to show my heartfelt appreciation to Dr. Ye Fan and Dr. Haijie Tan. I can still recall my very first day in Oxford. The passion towards research of both of you deeply attracted me. Ye developed all the techniques for device fabrication and measurements. Without his efforts, my research will not go very smoothly. Haijie is like a senior brother for me. He taught me all the techniques needed for my research and offered stimulating discussions. I would like to thank him for his friendship, empathy and sense of humor, which makes my time here interesting and fun.

I would also like to thank Wenshuo Xu, Yuewen Sheng, LinLin Hou and Qianyang Zhang for providing me samples with high quality for my research. I am also thankful for Dr. Shanshan Wang and Dr. Youming Rong for laying much of the groundwork in materials synthesis. Thanks to Qu Chen and Hefu Huang for their assistances and suggestions throughout my projects. I would like to say thanks to all my research colleagues for their constant encouragement. In particular, I am grateful to Dr. Paul Pattinson for his great maintenance of all the facilities in the cleanroom and his great smile really made my day in the cleanroom.

I should gratefully acknowledge the Chinese Scholarship Council for supporting my study in University of Oxford. I also thank all the staff in Materials Department and Linacre College for their support.

My sincere thanks go to all my friends in Oxford. In particular, I am grateful to Sha Li and Syed Ghazi Sarwat for accompanying me, encouraging me and enlightening me.

Last but not the least, I would like to thank my parents and my aunt for their love, caring and sacrifices for supporting me throughout my whole life.

Publications

Chapter 5

1. **Zhou, Y.;** Tan; H.; Sheng, Y.; Fan, Y.; Xu, W.; Warner, J.H. Utilizing Interlayer Excitons in Bilayer WS_2 for Increased Photovoltaic Response in Ultrathin Graphene Vertical Cross-Bar Photodetecting Tunneling Transistors. *ACS Nano,* 2018, *12 5*, 4669-4677.

Chapter 6

2. **Zhou, Y.;** Xu, W.; Sheng, Y.; Huang, H.; Zhang, Q.; Hou, L.; Shautsova, V.; Warner, J.H. Symmetry Control of Reversible Photovoltaic Current Flow in Ultrathin All 2D Vertically Stacked Graphene/MoS_2/WS_2/Graphene Devices, 2018 (Submitted)

Co-Author Papers

3. Tan, H.; Fan, Y.; **Zhou, Y.;** Chen, Q.; Xu, W.; Warner, J.H. Ultrathin 2D Photodetectors Utilizing Chemical Vapour Deposition Grown WS_2 With Graphene Electrodes. *ACS Nano*, 2016, *10 8*, 7866-73.

4. He, Z.; Xu, W.; **Zhou, Y.;** Wang, X.; Sheng, Y.; Rong, Y.; Guo, S.; Zhang, J.; Smith, J.M.; Warner, J.H. Biexciton Formation in Bilayer Tungsten Disulfide. *ACS Nano,* 2016, *10 2*, 2176-83.

5. Fan, Y.; Robertson, A.W.; **Zhou, Y.;** Chen, Q.; Zhang, X.; Browning, N.D.; Zheng, H.; Rümmeli, M.H.; Warner, J.H. Electrical Breakdown of Suspended Mono- and Few-Layer Tungsten Disulfide via Sulfur Depletion Identified by in Situ Atomic Imaging. *ACS Nano*, 2017, *11 9*, 9435-9444.

6. Chen, T.; **Zhou, Y.;** Sheng, Y.; Wang, X.; Zhou, S.C.; Warner, J.H. Hydrogen-Assisted Growth of Large-Area Continuous Films of MoS_2 on Monolayer Graphene. *ACS Appl. Mater. Interfaces,* 2018, *10 8*, 7304-7314.

Contents

Chapter 1 Introduction 1

1.1 Project Aim 1

1.2 Layout of this Thesis 1

Chapter 2 Literature Review 3

2.1 Introduction 3

2.2 Fundamental Properties of 2D Materials 5

2.2.1 Graphene 5

2.2.2 TMDs 9

2.2.3 2D Van der Waals Heterostructure (vdWHs) 18

2.3 Devices based on TMDs (WS_2, MoS_2) 23

2.3.1 Field-Effect-Transistor 23

2.3.2 Devices based on TMDs Vertical Heterostructure 27

2.4 Production Methods of 2D Materials based Heterostructures 39

2.4.1 Chemical Vapour Deposition (CVD) 40

2.4.2 Mechanical Exfoliation-Artificial Stacking Assembling 41

Chapter 3 Device Fabrication and Characterization 44

3.1 Introduction 44

3.2 2D Materials Synthesis 45

3.2.1 CVD Synthesis of Graphene 46

3.2.2 CVD Synthesis of WS_2 46

3.2.3 CVD Synthesis of MoS_2 47

3.3 Device Fabrication Process 48

3.3.1 2D Materials Transfer Method 48

3.3.2 Electron-Beam-Lithography 50

3.3.3 Reactive-Ion Etching 51

3.3.4 Metal Deposition 52

3.4 Materials Characterization 52

3.4.1 Optical Microscopy 52

3.4.2 Scanning Electron Microscopy (SEM) 53

3.4.3 Raman and Photoluminescence (PL) Characterization 53

3.4.4 Atomic Force Microscopy (AFM) and Kelvin Probe Microscopy (KPM) 54

3.5 Device Electrical Measurement 55

Chapter 4 Grain Boundaries Mediated Charge Transport in Monolayer WS_2 57

4.1 Introduction 57

4.2 Results and Discussions 58

4.2.1 Optical Characterization of WS_2 with GBs 58

4.2.2 Electrical Characterization of WS_2 with GBs 61

4.2.3 AFM and KPM Characterization of the WS_2 with GBs 64

4.3 Conclusion 66

4.4 Contribution Statement 66

Chapter 5 Utilizing Interlayer Excitons in Bilayer WS_2 for Increased Photovoltaic Response in Ultrathin Graphene Vertical Cross-Bar Photodetecting Tunneling Transistors 67

5.1 Introduction 67

5.2 Results and Discussion 68

5.2.1 Fabrication of Gr/WS_2/Gr Vertical Device 68

5.2.2 Raman and PL Characterization 70

5.2.3. Doping Levels of Gr_B and Gr_T in the Gr/WS_2/Gr Junction 73

5.2.4 Electrical and Opto-electrical Measurement of Gr/WS_2(1L)/Gr Vertical Heterostructure 74

5.2.5 Electrical and Opto-electrical Measurement of Gr/WS_2(2L)/Gr Vertical Heterostructure 79

5.3 Conclusion 84

5.4 Contribution Statement 84

Chapter 6 Symmetry Control of Reversible Photovoltaic Current Flow in Ultrathin All 2D Vertically Stacked Graphene/WS_2/MoS_2/Graphene Devices 85

6.1 Introduction 85

6.2 Results and Discussion 86

6.2.1 Fabrication of Gr/TMD Heterobilayer/Gr Vertical Device 86

6.2.2 Raman and PL Characterization 88

6.2.3 Opto-electrical Measurement 89

6.3 Conclusion 100

6.4 Contribution Statement 101

Chapter 7 Conclusion and Future Outlook 102

7.1 Thesis Summary 102

7.2 Future Outlook 103

Appendix A Supporting Information of Chapter 5 105

Appendix B Supporting Information of Chapter 6 107

References 109

Chapter 1 Introduction

1.1 Project Aim

This doctoral project aims to explore the electronics and optoelectronics application of chemical vapour deposition synthesized (CVD) two-dimensional (2D) transition metal dichalcogenides (TMDs). Specifically, vertical heterostructures involving MoS_2, WS_2 and graphene are fabricated for photodetectors and photovoltaics studies.

1.2 Layout of this Thesis

This thesis includes the research I conducted over the span of my four years DPhil study in the Department of Materials, University of Oxford. Chapter 2 provides a broad overview of properties of 2D materials, viz. TMD materials, graphene, and vertical heterostructures based on them t. A review of the optical and electronic properties of 2D materials, and the device applications based on their heterostructures are the main sections in this chapter. The methodology and equipment used for the research are introduced in chapter 3.

Chapter 4 highlights my work in discovering the influence of the GBs on the electrical performance of WS_2 based field-effect transistors: GBs are most common in CVD synthesized 2D materials as domains of different orientations grow and coalesce into each other, forming

into larger domains and eventually a film. We fabricated FETs on pristine WS_2, along the GBs and perpendicular to GBs, in order to study the effect of GB orientation on the electrical properties of FETs. Increased n-doping at the GB is found to induce a negative shift in the threshold voltage of the device, when the conductive channel is along the GB. Chapter 5 is focused on vertical heterostructure devices incorporating WS_2 and graphene for photovoltaic applications. The optical properties of the devices with monolayer and bilayer WS_2 as the photo-active layer are compared. Chapter 6 demonstrates vertical heterostructure photovoltaic devices with WS_2/MoS_2 as the photo-active layer and graphene as the conducting transparent electrode. The type-II energy band alignment between the TMDs is found to play an important role in generating the photo-voltage in the devices.

Chapter 7 highlights the summary of my DPhil work, and also presents the challenges and opportunities with future research on devices based on 2D materials.

Chapter 2 Literature Review

2.1 Introduction

Since the discovery of graphene in 2004, 2D materials, which can be single or few atoms thick, have received tremendous attention due to their outstanding physical and chemical properties. After a decade of research and development, 2D materials have expanded to a big family, based on the variety of electronic properties they possess, namely metallic, semi-metallic, semi-conducting, as well as insulating, with thickness dependent direct and indirect bandgaps. The compatibility of 2D materials fabrication process with the current complementary metal-oxide semiconductor (CMOS) processes, as well as their unique electrical,(*1*,*2*) optical,(*2*) thermal,(*3*) and mechanical properties(*4*, *5*) make them promising candidates for next-generation ultrathin electronics and optoelectronics devices, particularly for wearable and flexible technologies.

Graphene, a single layer of sp^2 bonded carbon atoms has very high carrier mobility,(*6*) is chemically inert (*7*) and has good mechanical flexibility(*8*, *9*). These properties make it useful for flexible electronics and as an electrode material for transparent and ultrathin 2D devices. With regard to these properties, graphene has found a host of applications, ranging from chemical(*10, 11*) and strain sensors(*12*, *13*) to transistors.(*14*) However, graphene has low

absorption of light, only 2.3% in the visible range. This follows from the absence of an intrinsic bandgap.(*15*) Although, a band-gap can be induced externally in graphene through high strain or electric field,(*16–18*) such approaches are energy-consuming and less practicable for application compared to direct band gap semiconductors.

Transition metal dichalogenides (TMDs), a promising complement of graphene, such as MoS_2 and WS_2 are recent 2D materials with an intrinsic bandgap, and for this reason have been intensively studied as photodetectors.(*19, 20*). Both of the MoS_2 and WS_2 are appealing due to their chemical and thermal stability,(*21*) tunable band-gap ranging from visible to UV,(*22*) large crystal size and possibility of forming uniform films using CVD method.(*23*)

A promising approach is to combine various 2D materials to form a sandwich, which was first described by Andrea Ferrari in 2013 IEDM conference. Without the constraints of lattice mismatching, 2D layered materials can be assembled together to form a wide range of heterostructure, including van der Waals vertical heterostructure and lateral heterostructure. The heterostructures make use of the unique properties of each component and offer a new platform with novel properties which do not exist in the components standalone. The variety of 2D materials combined with stacking sequences of layers provide a rich playground for manually creating ‘new materials’.

This chapter is focused on the development of the electronic and opto-electronic devices based on the 2D materials heterostructures. It starts with the review of the fundamental properties of 2D materials, including graphene, TMDs and the 2D materials-based van der Waals heterostructures. Then followed by the review of the devices based on TMDs and their heterostructures. The last part is the fabrication methods for the heterostructures composed of 2D materials.

2.2 Fundamental Properties of 2D Materials

In this chapter, the atomic structure, electronic properties and the optical properties of graphene, TMDs and the heterostructures based on graphene and TMDs are introduced. A thorough understanding of these properties of 2D materials is helpful for their application in electronic and optoelectronic devices.

2.2.1 Graphene

2.2.1.1 Electronic Properties of Graphene

It is very essential to get a basic understanding of the atomic and electronic structure of graphene before we go any further to discuss the electronic and optical properties of it, as most of the prominent properties of graphene can be derived from its unique band structure.

Band Structure

Monolayer graphene is honeycomb structure with each carbon atom connected to the nearest three carbon atoms through covalent bonds.(*6*, *15*, *24*) To be specific, in a carbon atom, four valence electrons play a major role in determining the electronic properties. Three orbitals, namely s, p_x, p_y, undergo sp^2 hybridization into three equivalent orbitals distributed with 120 degree angle between each other. These three hybridized orbitals form strong σ bonds with other surrounding carbon atoms, with the C-C bond length of 1.42Å.(*15*, *25*) The p_z electrons remained are distributed perpendicular to the atom plane, and form the π band (**Figure 2.1**a).(*26*) The energy of electrons in the π band is split into two states, with the π-state forming the valence band and the π^*-state the conduction band.(*24*, *25*, *27*) The conduction band and valence band meet at the Dirac point. In the vicinity of the Dirac point, the relationship between electron's energy and momentum is linear, as shown in **Figure 2.1**b, which can be described with an equation: $E(k) = \pm\hbar v_F|k|$.(*26*, *27*) Where $\hbar$ is the reduced Planck constant, v_F is the

fermi velocity, and the wave vector k is measured from the Dirac points. The linear relationship is similar to the Dirac equation for the Dirac fermion with massless property.(*28*) Hence, the electrons and holes with energy near Dirac point in graphene are theoretically massless.

Transport Properties of Graphene

The high carrier mobility of graphene is one of the most prominent properties which makes graphene so attractive as a material .(*29*) However, because of the ultrathin nature of graphene, its carrier mobility is very sensitive to intrinsic and extrinsic factors. In suspended graphene, mobility up to 200,000 $cm^2\ V^{-1}s^{-1}$ has been observed at room temperature at a carrier density of $2\times10^{11}\ cm^{-2}$, which is limited by the acoustic phonon scattering from the intrinsic graphene itself.(*30*, *31*) The defects in graphene can have a more significant influence on the mobility. The value been measured limited by the defects scattering reaches 15000 $cm^2\ V^{-1}s^{-1}$ within a wide temperature range (10k to 100k).(*28*) The carrier mobility decreases significantly when the graphene is sitting on amorphous SiO_2 substrate, on which the electrons of graphene experience strong scattering from the optical phonons of SiO_2. This further brings the mobility down from 200,000 $cm^2\ V^{-1}s^{-1}$ to less than 40000 $cm^2\ V^{-1}s^{-1}$ at room temperature.(*31*) The absorbed contaminates also cause scattering to the carriers.(*30*) In order to improve the carrier mobility in graphene, researchers use substrate with higher phonon frequencies, for example hBN, to sandwich graphene to isolate carriers from both substrate and contaminate scattering.(*32*) Up until now, graphene synthesized by chemical vapour deposition method typically presents low mobility mainly because of the high density of defects.(*33*, *34*) Besides the scattering effects, the charge carrier density also affects the mobility.(*24*, *29*) Normally, the mobility decreases with the increasing of carrier density for monolayer graphene, while for bilayer/trilayer counterparts, the mobility increases with the increase of carrier density.(*29*)

2.1.1.2 Optical Properties of Graphene:

The optical properties of graphene also attract tremendous interests. A free-standing monolayer graphene can transmit around 97% and absorb around 2.3% of the incident light over the visible range wavelength (**Figure 2.1**c).(*27*, *35*) The light-graphene interaction is strong, considering its atomic thickness. The absorption of monolayer graphene (0.3nm thick) is equivalent to that of 25 nm thick Si in the visible range. Its absorption can be modulated by electrical gating or chemical doping.(*36*, *37*) When the photon energy is less than $2E_F$, where E_F is the graphene fermi level, inter-band excitation is prohibited and intra-band excitation dominates the absorption (**Figure 2.1**d).(*37*) The substrates also have strong impact on the absorption of graphene by inducing multiple reflections and interferences.(*38*)

The large light transmission and high carrier mobility make graphene to be an excellent candidate for the conductive electrodes in electronic(*39*, *40*) and optoelectronic(*40–42*) applications, such as touch screens, solar cells and flat panel displays.

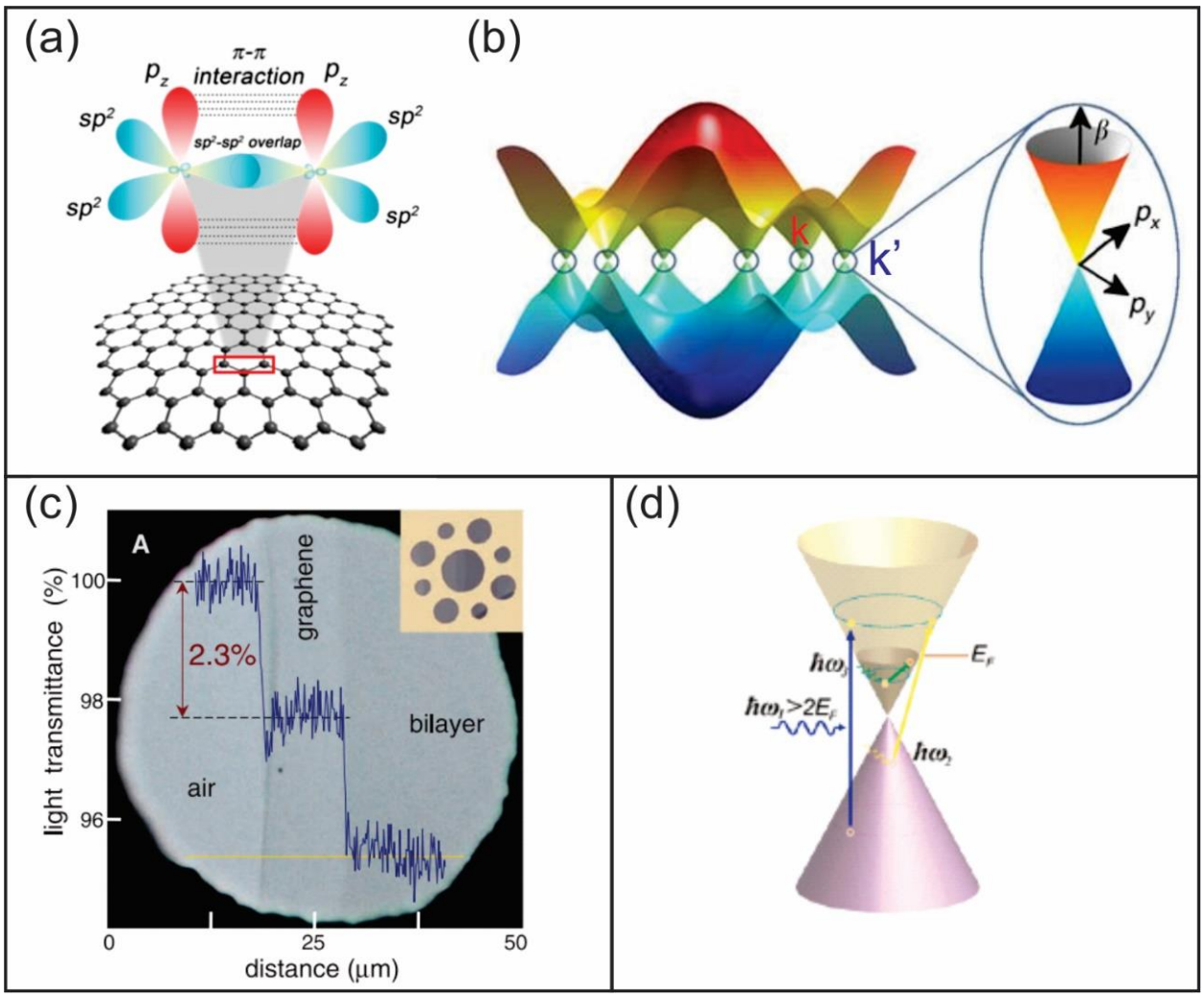

Figure 2.1 Atomic and electronic structure of graphene (a) The sp^2 hybridization of the carbon atoms and the bond formation in graphene. Reproduced with permission.(*26*) (b) The electronic band structure of monolayer graphene. The valance band and conduction band degenerate at Dirac point. Near the Dirac point, the energy is linearly dependent on the momentum. Reproduced with permission.(*43*) (c) The transmittance of suspended monolayer and bilayer graphene of white light. Reproduced with permission.(*35*) (d) Schematic diagram of the process of inter-band absorption of photon (ħw1), inter-band plasmon absorption(ħw2) and intra-band plasmon absorption (ħw3). w1, w2, w3 are the frequencies of incident photons. ħ is the reduced Planck constant. Reproduced with permission.(*37*)

2.2.2 TMDs

2.2.2.1 Electronic Properties of TMDs

Band Structure

Layered TMDs are a group of materials with transition metal (M) from group IV (Ti, Zr, Hf), group V (V, Nb, Ta) and group VI (Mo, W) covalently bonded with chalcogens (S, Se, Te), in the formula of MX_2 (**Figure 2.2**a).(*44*) The layered TMD materials are stacked with van der Waals interaction to form its bulk counterpart with interlayer spacing of 6.5Å.(*45*) Varying the stacking orientation of the adjacent TMD layers and the metal atom coordination creates three polytypes, namely 3R, 2H and 1T, as shown in **Figure 2.2**b.(*45*, *46*) 3R phase has rhombohedral symmetry, three layers per repeat unit and trigonal prismatic coordination. 2H phase has hexagonal symmetry, two layers per repeat unit and trigonal coordination. 1T phase has tetragonal symmetry, one layer per repeat unit and octahedral coordination. Among these three phases, 3R phase is found only in bulk compounds and easy to relax to 2H phase under mild heating. 2H phases are stable in nature and TMDs in this phase show semiconducting property. 1T is metallic and metastable in nature. 2H phase TMDs with the metal component being Nb and Ta exhibit metallic property(*47*) and TMDs including W and Mo are semiconductor.(*44*) This thesis is mainly focused on the 2H semiconducting TMDs.

MoS_2 and WS_2, both semiconductors, are two of the most extensively studied compounds.(*45, 48*) Their energy band structures change gradually with the number of layers.(*49–52*) For example, electronically, bulk WS_2 is an indirect gap semiconductor with the bandgap around 1.2eV, whereas a direct energy gap of ~2eV at the corners (K and K$'$ points) of the Brillouin Zone arises in monolayer WS_2.(*2*) Theoretical calculation of the band structure of MoS_2 shows when reducing MoS_2 from bulk to monolayer, quantum confinement results in an increase in the indirect gap energy at Γ point while the direct gap at K point remains almost

constant.(*52*, *53*) The thickness dependence of indirect bandgap near Γ point is mainly because the adjacent states are combinations of d-orbitals on Mo atoms and P_z orbitals on S atoms, which have strong interlayer coupling effect. On the other hand, the conduction band near K point is composed of d-orbitals on Mo atoms, which are sandwiched between S atoms, less influenced by the adjacent layer.(*52*) The changing MoS_2 energy band with the number of layers is shown in **Figure 2.2**c.(*52*)

Spin Splitting

Monolayer semiconducting TMDs, such as MoS_2 and WS_2, exhibit strong spin-orbit coupling induced band splitting and spin-valley interaction (**Figure 2.2**d).(*54*, *55*). Unlike their bilayer counterpart, monolayer TMDs are non-centrosymmetric.(*52*, *53*) The lack of spatial inversion symmetry, the confinement of the electrons in-plane and the large effective mass of carrier in the monolayer TMDs result to a strong spin-orbit splitting in the valence band: from Γ to K point, with the splitting energy ranges from 0.15 to 0.45 eV.(*54*)

Transport Properties of TMDs

In 2D TMD materials, similar to graphene, the charge carrier transport and scattering are confined in-plane. The main scattering mechanisms influencing the charge mobility in TMDs are similar to those of graphene mentioned earlier: 1) scattering from intrinsic phonons (*56*) 2) Coulomb scattering due to the impurities and defects(*57*, *58*) 3) phonon scattering from the interfaces (*59*) and 4) scattering due to material roughness.(*2*)

Scattering from phonons in TMDs becomes stronger with temperature.(*56*) In brief, there are two types of phonons- acoustic phonon and optical phonon. At low temperature (<100K), the acoustic phonon scattering dominates, while at high temperature, the optical phonon scattering dominates. So at room temperature, the mobility of TMDs as high as around 410 $cm^2V^{-1}s^{-1}$ has been calculated, which is limited by the scattering of optical phonons.(*56*) Coulomb scattering

is due to the defects and the impurities within the layer or on the surface of the materials and becomes dominant under low temperature.(*60*) Doping materials with ionic impurities is a popular method used to tune the charge carrier concentration and bandgap, but it also decreases the carrier mobility significantly through increased scatting .(*61*) As a result, it is very important to optimize the doping level of the materials to ensure the mobility for a particular device.

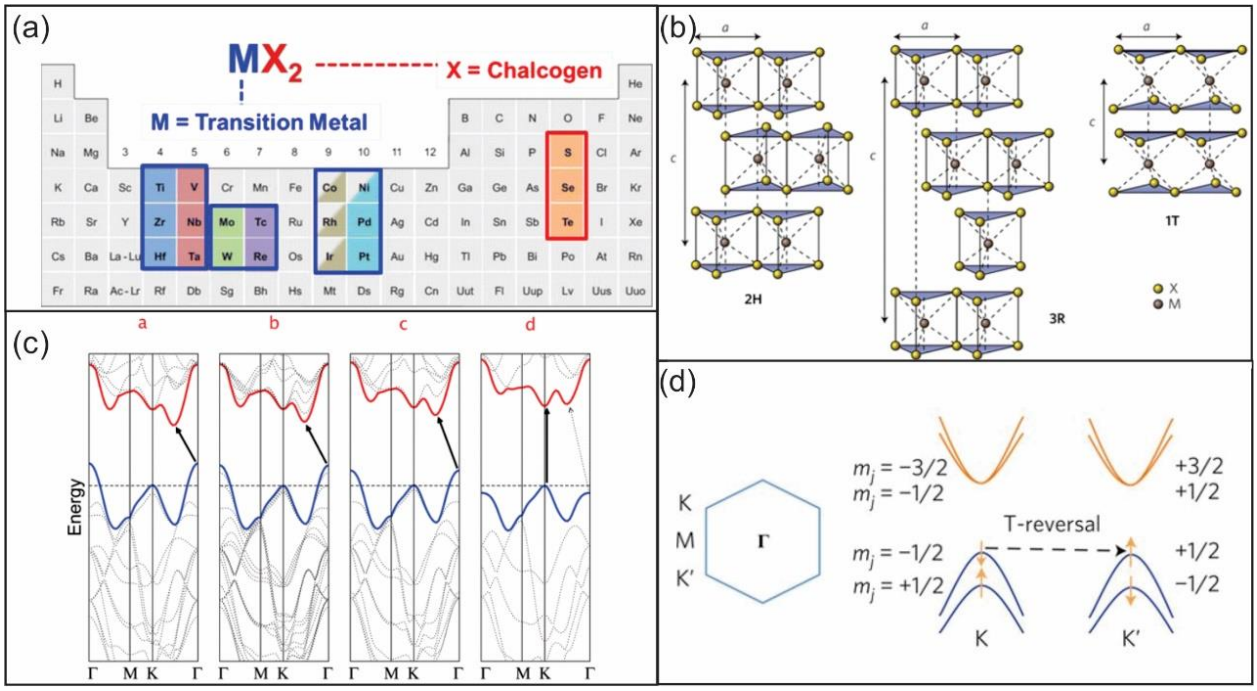

Figure 2.2 Atomic and electronic structure of TMD materials (a) Periodic table with 16 transition metal and 3 chalcogen elements highlighted for combination of transition metal dichalcogenides. Reproduced with permission.(*62*) (b) Schematic diagram of the three types of multilayer TMDs structure. 2H and 3R are composed of trigonal prismatic monolayer with different stacking sequences, with hexagonal symmetry for 2H and rhombohedral symmetry for 3R. 1T is composed of octahedral single layer stacking in tetragonal symmetry. Reproduced with permission.(*2*) (c) Energy band of MoS_2 changing from indirect to direct with the decrease of number of layers to monolayer (a to d corresponding to bulk to monolayer). Reproduced with permission.(*52*) (d) The valance band splitting of monolayer MoS_2 caused by spin-orbit coupling at K and K' valleys. The energy splitting between spin up and spin down states is 160meV. Reproduced with permission.(*63*)

2.1.2.2 Optical Properties

Exciton

When a photon is absorbed by TMD materials, an electron is excited from valence band to conduction band and a positively charged hole is left behind. The electron and hole are attracted to each other through electrostatic Coulomb force, forming exciton. The Coulomb interaction within exciton in bulk TMD materials is smaller than the energy of room temperature (25.7meV), which results in the easy dissociation of the excitons into free charge carriers.(*64*) So the optical properties of the bulk TMD materials are mainly determined by the electronic band structure at room temperature. While at low temperature, the excitons are still bounded, in which case, the optical properties of materials are determined by both the Coulomb interaction and the electronic band structure. When the thickness of the TMD materials decreases, the quantum confinement effect and the reduced dielectric screening enhance the Coulomb attractions between the excited electron and hole.(*64*) So in monolayer TMDs, excitonic effect plays an important role in determining the optical properties. Exciton binding energy is an important parameter to evaluate the strength of the Coulomb interaction within the exciton. It is calculated by subtracting the optical bandgap from the electronic bandgap. For monolayer TMDs, the exciton binding energy is as high as twice of that in the bilayer form. Theoretical calculation conducted by Tawinan *et al*. demonstrated that the exciton binding energy is 0.897eV for monolayer and 0.424 eV for bilayer MoS_2.(*64*)

Photoluminescence

The change of the indirect to direct bandgap and the increase of the bandgap energy of TMD materials from bulk to monolayer brings modulation in the optical properties, namely in photoluminescence,(*51*) absorption,(*65*) and photo-conductivities.(*53*) Photoluminescence is a light emission through electron-hole recombination after the absorption of photons with energy

higher than the optical bandgap. It is a fundamental method used to study the electronic and optical energy bandgap of TMDs.

For monolayer MoS_2, two PL peaks emerge at 1.9 eV (peak A) and 2.05 eV (peak B), originating from direct band (K-K') recombination.(*66*) The energy splitting of the two peaks arises from the valance-band splitting due to the spin-orbit coupling and lack of inversion symmetry, which we mentioned above. With increasing the thickness, an additional peak appears at a lower energy, that stems from indirect band (Γ-K).(*53*, *67*) At the meantime, the PL peaks from direct band recombination experience slight redshift due to the decrease of the electronic bandgap.(*53*) Quantum yield (QY) in multilayer TMDs also is quenched as extra phonons are needed for the indirect band exciton recombination to obey the momentum conservation.(*53*) **Figure 2.3**a shows the excitons recombination routes for both monolayer and bilayer TMDs. The differences of PL peaks and QY between monolayer and non-monolayer TMDs are thus reflections of the evolution of energy band of TMDs from indirect to direct with thickness decrease. **Figure 2.3**b shows the QY comparison of monolayer and multilayer WS_2. It is obvious that the QY in 4 layer WS_2 quenches significantly, and the intensity ratio between monolayer and bilayer is as high as 100.(*68*)

Many other external factors can tune the PL QY and also the PL peaks of the TMDs materials, such as strain,(*22*) chemical doping,(*69*) defects(*70*, *71*) and electric field.(*65*) Electrostatic modulation through a gate voltage is the most common way to tune the PL in the TMD based devices. By setting gate voltage to be negative or positive, the TMD materials can be p-doped or n-doped.(*72*) Excitons are prone to combine with excessive electrons or holes to form negative or positive trions with a lower energy, following the equation: $X^0 + e(h) = X^-(X^+)$, as shown in **Figure 2.3**c. Trion has lower energy than exciton, so if excessive electrons are induced in materials, peak of trion emerges at a lower energy, red-shifting the PL peak, shown in **Figure 2.3**d.(*72*)

Raman

Raman spectra can reveal the fundamental structural and vibrational properties of TMDs. For the monolayer layer (MoS_2 and WS_2), Raman active modes consist an out-of-plane mode A_{1g}, which only involves chalcogens atoms vibration, and two in-plane-modes E_{2g} (E^1_{2g} and E^2_{2g}), which involves the vibration of both transition metal and chalcogens atoms. **Figure 2.3**e shows the diagram of the three vibration modes. E^2_{2g} mode reflects the vibration of two rigid layers against each other and generates a Raman peak at very low frequency (<50 cm^{-1}), so the E^2_{2g} mode is absent in monolayer TMDs. Raman spectrum is used to determine the number of layers of TMDs as the Raman peaks shift as the number of layer changes.(*73*, *74*) **Figure 2.3**f shows typical Raman spectra of WS_2 with different number of layers. When increasing the numbers of layers of WS_2, the E^1_{2g} peak remains stable in frequency while the A_{1g} undergoes a blueshift, showing a lattice stiffening effect. This behavior is assumed to be the result of the decreased van der Waals interaction, which reduces the restoring force of the out-of-plane vibrational mode and enhances that of in-plane mode.(*75*) As a result, the frequency difference between E^1_{2g} and A_{1g} can be used as a useful indicator of the number of layers of TMDs materials. Raman spectrum can also reveal the doping of TMD materials.(*76*) The A_{1g} peak experiences broadening and redshift while E^1_{2g} remains almost constant when WS_2 is n-doped.

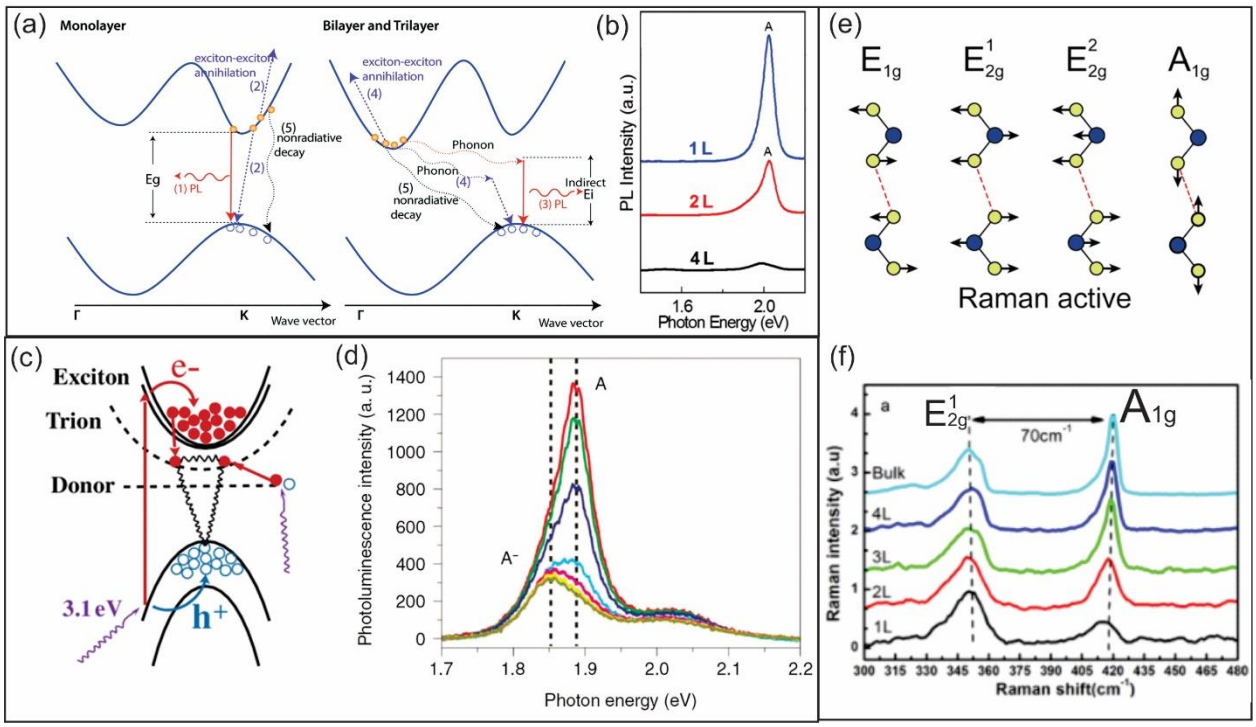

Figure 2.3 Photoluminescence and Raman of TMDs (a) Schematic diagram of mechanism of PL spectra in direct and indirect energy band. Reproduced with permission.(*77*) (b) PL intensity quenches with the increase of the number of layers of WS_2 sitting on SiO_2/Si. Reproduced with permission.(*68*) (c) Schematic of trion formation with excessive electrons in monolayer WS_2. Reproduced with permission.(*78*) (d) PL spectra of monolayer MoS_2 under different back-gate voltages. With the increase of the gate voltage, the A (exciton) peak evolves into two peaks, with a new A^- (trion) peak at lower energy. Reproduced with permission.(*72*) (e) Three in-plane and one out-of-plane Raman active vibration modes in TMDs. (f) Raman spectra of WS_2 with different number of layers. Reproduced with permission.(*75*)

2.1.2.3 Transition Metal Dichalcogenides Grain Boundaries

Chemical vapour deposition (CVD) method is one of the most promising synthesis approaches for wafer-scale, uniform two-dimensional MoS_2 and WS_2. However, the continuous films are polycrystals with grain size on the order of hundred micrometers, where GBs are widespread. An understanding of the nature of the GBs is therefore crucial as they can modulate the otherwise intrinsic properties of the 2D materials.

Atomic Structure of Grain Boundaries

Transmission electron microscopy (TEM) is widely used for the observation of the GBs atomic structure. It is found that the atomic structure of GBs of MoS_2 is closely related to the misorientation angle between the grains forming the GBs, which thus results in different optical and electrical properties along the GBs.(*79*) With a close observation of the GBs in monolayer MoS_2, Young Hee Lee found that most of the GBs are composed of three basic structures: 5-7 cores (**Figure 2.4**a-c), 4-4 cores and 4-8 cores (**Figure 2.4**d).(*80*) In brief, for low angle GBs (< 13°), which are straight, the dislocation core is a 5-7 ring (**Figure 2.4**a). The periodicity of the dislocation core distance is inversely proportional to the misorientation angle (**Figure 2.4**e). For high angle GBs (> 13°) with certain angles (22°, 28° and so on), the basic component is also 5-7 ring (**Figure 2.4**b,c). While those with angles deviated from the certain angles are curvy and without periodic lattice. Mirror twin GBs (60°) are composed with 4-4 cores (**Figure 2.4**d above) when along zig-zag direction and 4-8 cores along arm-chair direction (**Figure 2.4**d below).

Mirror twin GBs are commonly molybdenum rich, which brings n-doping effect to the boundaries, while 5-7 defects at tilt GBs are sulfur rich, which would p-dope boundaries.(*79*) The photoluminescence of MoS_2 is affected by the charge density, so the PL intensity with 100% enhancement at tilt GBs and 50% quench at the mirror twin GBs can be observed (**Figure 2.4**f).(*81*)

Electrical Properties of Grain Boundaries

The electronic properties at the GBs can be studied with scanning tunneling microscopy (STM). MoS_2 experiences bandgap decrease by 0.85 eV at the high angle GB (18°), with the valance band maximum (VBM) shifting 1.05 eV towards fermi level and conduction band minimum (CBM) shifting 0.2 eV away from it (**Figure 2.4**g). At the small angle GB (3°), the

bandgap decreases by only 0.17 eV. The bandgap modulation is mainly induced by the local strain field brought by the distortions at the GBs.(*82*) This result is consistent with Young Hee Lee's observations, where the dislocation cores at high angle (>9°) GB in MoS_2 are with periodical distance less than 2nm, so the electrostatic potential at GB acts as 1D barrier for carriers transporting across them, which causes right shift of the threshold voltage for inter-domain conductance and decreases the mobility, with lower mobility for lower misorientation angle. *(80)* Unlike the tilt GBs, the mirror twin one behaves as a metallic channel, thus has the highest mobility among the GBs defects.(*80*)

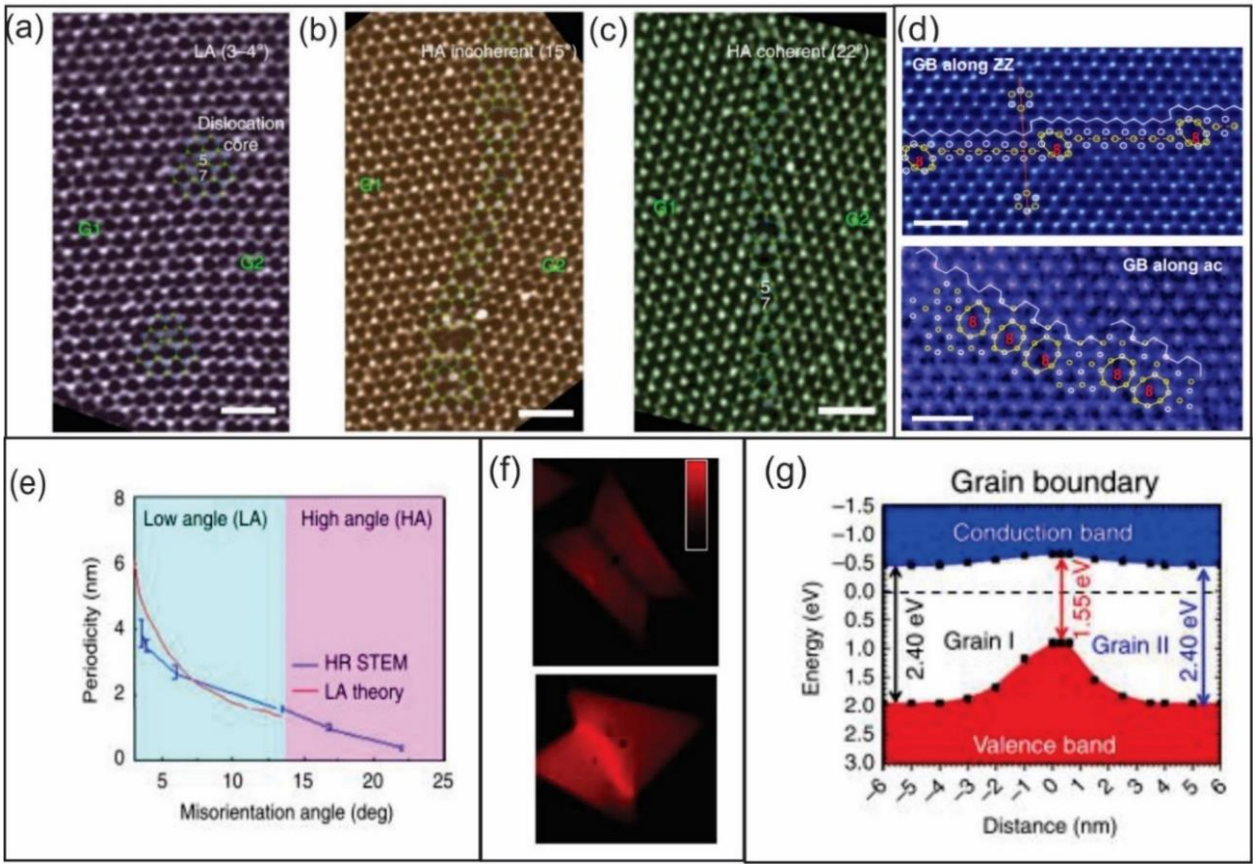

Figure 2.4 TMDs GBs atomic structure, optical and electronic properties. (a-d) High resolution annular dark field-Scanning tunneling electron microscopy (ADF-STEM) images of low angle, high-angle incoherent, high-angle coherent tilt GBs and mirror twin GBs along zigzag, armchair direction. (e) Periodicity of the dislocation cores decreases with the increase of the misorientation angle. (a-e) Reproduced with permission.(*80*) (f) PL intensity quenches for mirror twin GB (above) and enhances for tilt GB (below). Reproduced with permission.(*81*) (g) Energy band diagram of MoS_2 at the GB(18°). Reproduced with permission.(*82*)

2.2.3 2D Van der Waals Heterostructure (vdWHs)

Heterostructures (HS) comprise layered materials held together through van der Waals force. Because 2D materials are free of dangling bonds, the HS have no lattice matching constraint, which brings freedom in the fabrication without worrying about the distortion and defects in the interface.(*83*) With the boost of 2D materials, a substantial variety of HS can be created, which not only possess the properties of the materials composing them but also exhibits some novel properties that the standalone component does not have. This means, by selecting the right 2D materials and stacking them with desired sequence, it is possible to create new properties according to our needs. By now, a variety of experiments have been conducted on vdWHs to study their fundamental properties as well as to use them in different devices.

2.1.3.1 Structure Properties of HS

Unlike conventional HS, in which the interfaces are always rough, one of the prominent properties of vdWHs is the high quality of interface. The lack of dangling bands in the ultrathin layered materials enables the creation of the high-quality hetero-interfaces without the lattice precise constrains.(*84*, *85*) The pioneering work to open the 2D-2D vdWHs field was conducted by Dean *et al*. They stacked graphene on hBN and observed the dramatically improvement in electrical performance due to the smooth and clean interface between the hBN and graphene.(*32*) In some of the crystal pairs, a "self-cleaning" mechanism exists in the interfaces, which results in atomically flat and contaminate free interfaces,(*86*, *87*) as shown by the STEM images in **Figure 2.5**b and c. With the discovery of 2D TMDs materials, more options emerge for the fabrication of vdWHs.

Even though hBN was initially used to reduce the influence of the substrate on the graphene, structural reconstruction of graphene was observed, which is induced from van der Waal interaction with the neighboring hBN crystals.(*88*) hBN and graphene have similar lattice constants, so graphene tends to stretch itself to match the interatomic space of hBN when it is

on hBN, which leads to the formation of moiré pattern and induces strain in graphene.(*88*) When the relative orientation angle is large enough, the moiré pattern and the strain in graphene disappear, as shown in **Figure 2.5**d and e. This structural reconstruction is also observed in the HS formed with TMD materials.(*89*)

2.1.3.2 Electronic properties

The van der Waals interaction between the layered materials is weak, especially for manually stacked HS; therefore, the electronic influences from the adjacent layers is also weak. As a result, the electronic properties of the individual layers are well preserved even in the vdWHs.(*90*) In this case, the overall electronic properties of the vdWHs can be predicated from the properties of the individual components.

However, under some special circumstances, the electronic behaviors of the individual layers are changed when assembled with other layers.(*88*, *89*) We have mentioned above that in graphene/hBN HS, because of the similar lattice constants between them, moiré pattern is formed at specific rotational angles. This moiré pattern not only brings atomic reconstruction, but also alters graphene's electronic spectrum. This effect is also reported to have the ability to open the bandgap of graphene.(*91*) It is well-known that for TMD homobilayer, the interlayer coupling splits the degeneracy at Γ point, changing the direct energy band of monolayer into indirect bandgap.

When layered materials are stacked together, the work function differences result in a transfer of charges.(*90*) In conventional HS formed with bulk materials, such as conventional p-n junction, the charge transfer in the junction brings about a built-in electric field, which causes the formation of a depletion region in the junction, with the length ranging from tens to hundreds of nm dependent on the doping levels of the individual materials. Unlike conventional HS, there is no depletion region in the interface of the constituents, but with atomically sharp interfaces in the vdWHs.(*92*) To be simplified, the HS can be described as an atomically thin

capacitor composed of two parallel plates separated by a vdW gap with a built-in potential originated form the work function difference induced charge transfer between the stacked materials.

In the HS, the charge carriers can not only transfer within the individual layers but also transport out-of-plane across the vdW gap. Contrary to conventional bulk materials, the materials interacting through vdW force do not undergo orbital hybridization with neighboring layers. As a result, the transport barrier formed by the vdW gap minimizes the delocalization and diffusion of the charge carriers, Instead, the out-of-plane charge transfer is mainly through tunneling and hopping, causing the out-of-plane charge mobility to be lower than that of in-plane transport.(*93*)

2.1.3.3 Optical properties

The optical properties of HS consist of TMDs are mostly studied mainly because of their high absorption of visible light and favorable energy band.(*19*, *94*) For the TMD/TMD HS with different energy bandgaps and work functions, staggered type-II band alignment always forms,(*92*, *95*, *96*) which is when the CBM is located in one material and VBM in another to form the smallest energy transition, as shown in **Figure 2.5**g.(*97*) In the type-II energy band, the photo-generated electrons-hole pairs separate immediately into different layers within a shorter time (<50 fs) than that needed for the formation of intralayer excitons.(*98*) The bounded electrons and holes then reside in individual layers, forming interlayer exciton.(*92*, *98*) The HS of graphene and TMDs usually induces p-doping of the TMDs or n-doping of the graphene as the charge flows from TMDs to graphene.(*99*)

The ultrafast charge separation and the formation of the interlayer exciton dramatically suppress the recombination of the intralayer excitons in the TMD layers, thus the quenching of the PL QY of the individual layers is observed in the HS.(*99*) It is also interesting that a new PL peak with lower energy is always observed in the HS, besides those from the original

component layers, which is derived from the recombination of the interlayer exciton (**Figure 2.5**f).(*100*) An external electrical field can modulate the polarization of interlayer exciton, as shown in **Figure 2.5**g, and thus tunes the energy and intensity of the PL in the TMD HS.(*97*) To be specific, the gate voltage dopes two TMD layers in the heterostructure differently, thus reduces or enlarges the relative band-offset between TMD layers, changing the energy separation between the conduction band in one layer and valence band in another.

Because of the low energy of interlayer exciton as well as the space and momentum unfavorable recombination of the interlayer exciton, the life time of the interlayer exciton is measured to be the same or longer than that of intralayer excitons. Pasqual reported an interlayer exciton life time as long as 1.8 ns in monolayer MoS_2/WSe_2.(*97*) Its life time is ten times higher than the intralayer excitons in either MoS_2 or WSe_2, which is on the order of tens of ps. (*65*, *101*)

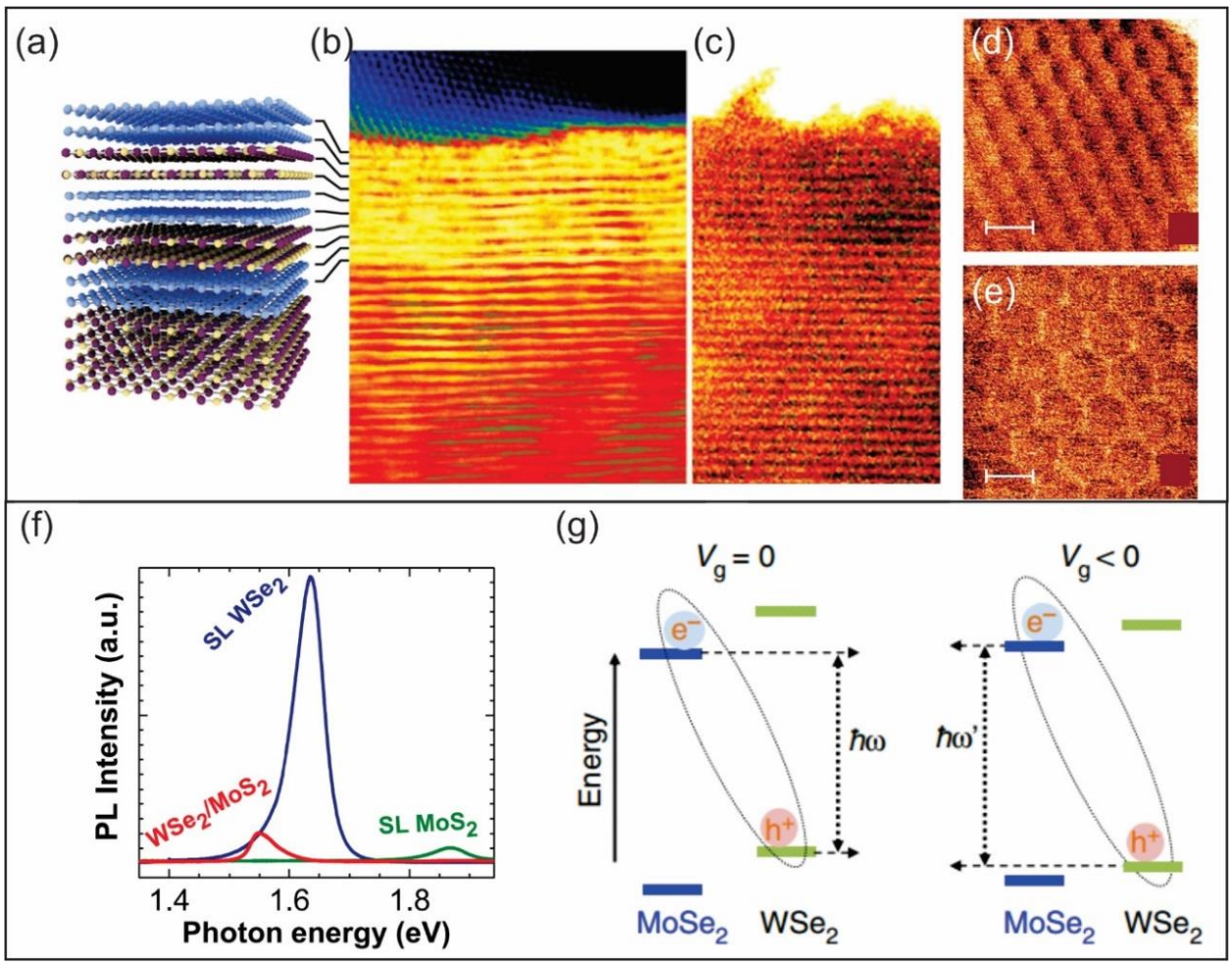

Figure 2.5 van der Waals heterostructure (a) Schematic diagram of van der Waal heterostructure formed with 2D graphene and hBN. Reproduced with permission.(*102*) (b) High-resolution bright-field and (c) high-angle annular dark-field (HAADF) imaging of the heterostructure shown in (a). The spacing for hBN-graphene equals to the interlayer distance in bulk hBN.(b,c) Reproduced with permission.(*87*) (d,e) Strain mapping induced in graphene sitting on hBN with orientaion angle (d) 3° and (e) 0°. (d,e) Reproduced with permission.(*88*) (f) PL spectra of monolayer WSe_2, MoS_2 and their heterostructure. The recombination of the interlayer exciton at the MoS_2 and WSe_2 interface give rise to a peak at low energy. Reproduced with permission.(*100*) (g) The interlayer exciton and band alignment of $MoSe_2/WSe_2$ heterostructure tuned with electrostatic field. Reproduced with permission.(*97*)

2.3 Devices based on TMDs (WS_2, MoS_2)

2.3.1 Field-Effect-Transistor

Several reports on two-dimensional TMDs are focused on the influence factors of the performance of TMDs-based FETs under room temperature. Ways of enhancing mobility and performance of the transistors have been investigated in various studies. It is found that the combination of gate structure, substrate, metal contacts, environment of measurement, defects can all affect the mobility, threshold voltage, subthreshold swing and the on/off ratio of the TMDs FET device.

In this section, we will discuss how dielectric layer, metal contact and absorbents affect the performance of TMDs based FETs. These studies serve as a fundamental knowledge in the fabrication of a high-performance device, which requires both engineering and scientific understanding of FETs based on two-dimensional semiconductors.

The subthreshold swing (the gate voltage needed to change the source-drain current by one decade in the subthreshold region) of a FET device can be expressed as

$$SS = ln10\left(1 + \frac{C_S + C_{it}}{C_{ox}}\right) kT/q \qquad \text{(Eq.2-1)}$$

Where C_S is the capacitance of the TMD channel, C_{it} is the capacitance coming from the interface traps, C_{ox} is the capacitance of the dielectric layer, k is the Boltzmann constant, T is the temperature, and q is the charge of a single electron. The minimum SS of a conventional field-effect transistor is calculated to be 60mV/dec at room temperature.

A reduced subthreshold swing would allow a small off state current and thus improve the on/off ratio of the devices. Therefore, one of the ways to enhance the performance of a FET is to increase the capacitance of dielectric layer, here referred as C_{ox}. The dielectric capacitance can be derived from equation $C_{ox} = \frac{\kappa \varepsilon_0 A}{t}$, where κ is the dielectric constant of the insulating

layer, ε_0 is the dielectric constant of free space, A is the capacitor area and t is its thickness. By employing a thin and high-κ dielectric layer in gates, a small SS can be achieved. Instead of using SiO_2 (k = 3.9) as the back-gate dielectric layer, which results in large subthreshold swing (>1V/dec),(*103*) Kis employed a 30 nm HfO_2, whose dielectric constant is 4-6 times higher than SiO_2, as top dielectric layer to the single layer MoS_2 FET to realize a better gate control.(*45*) A relatively low SS was achieved (74mV/dec). Ionic liquid was used as top gate to achieve an ambipolar characteristic in many devices which would otherwise be unipolar transistors.(*104*) Braga *et al*. fabricated a top gated FET based on WS_2 crystal using ionic liquid 1-buty-1-methyl pyrrolidinium tris-(pentafluoroethyl) trifluorophosphate $[P14]^+[FAP]^-$ as electrolyte dielectric. It enabled tuning of fermi level across bandgap, resulting in SS as low as 66mV/dec in room temperature and ambipolar transport shown in **Figure 2.6**a.(*104*)

The dielectric layer could also influence the charge carrier mobility through the introduction of disorder and dielectric screening of the coulomb scattering of the charge impurities in channels. PMMA was used as substrate for the MoS_2 FET, resulting in an increase of mobility (electrons) from 30 $cm^2\ V^{-1}s^{-1}$ (on SiO_2) to 470 $cm^2\ V^{-1}s^{-1}$ as shown in **Figure 2.6**b.(*105*) The result implies a long-rang disorder at the PMMA-TMD interface, while the SiO_2 TMD interface has a dominant short-range disorder due to chemical bonding or surface roughness.

The Schottky barrier often exists at the metal-semiconductor interface between electrodes and TMD, which causes underestimation of the field-effect mobility of charge carriers, thus it is very important to decrease the contact resistance by selecting the metal with low work function. Theoretically, the Schottky barrier height equals to the difference between metal work function and the electron affinity of TMD channel. However, the metal/TMD interface is also strongly impacted by Fermi level pinning close to the conduction band of TMD.(*106*) The Schottky barrier height is still dependent on the metal contact work function,

with low work function metal having lower barrier height, which correspondingly results in higher carrier injection (**Figure 2.6**c).(*106*) The result implied the importance of the correct use of metal contacts and reducing the fermi level pinning to yield higher mobility of a more accurate value. Graphene was used as electrodes to achieve Ohmic contact to the MoS_2. Linear I_{ds}-V_{ds} behavior was observed at room temperature and a record high extrinsic mobility over 1300 $cm^2\ V^{-1}s^{-1}$ was attained. (**Figure 2.6**d).(*107*)

Water, oxygen and other molecules from the ambient and substrate interface are very easy to be absorbed onto the surface of 2D TMDs, acting as dopants and charge scattering center. The changing of the doping level of single MoS_2 is well demonstrated from the horizontal shift of the transfer curve of the MoS_2 based FET towards a negative direction after annealing in vacuum, as shown in **Figure 2.6**e.(*108*) Monolayer WS_2 based FET also exhibits the similar phenomena.(*48*) The negative shift of the transfer curve indicates that more electron carriers are induced in the TMDs after vacuum annealing. It was reported that the adsorbates on the TMD surfaces are prone to accept electrons from TMDs, decreasing the density of the negative charge carriers. Removing the adsorbates by vacuum annealing increases the n-doping level in TMDs. As we mentioned before, the adsorbates act as charge scattering center. The removing of the adsorbates is also helpful for increasing the charge carrier mobility. By encapsulating TMD by h-BN to avoid the absorption of the molecules, the device performance can be improved.(*109*)

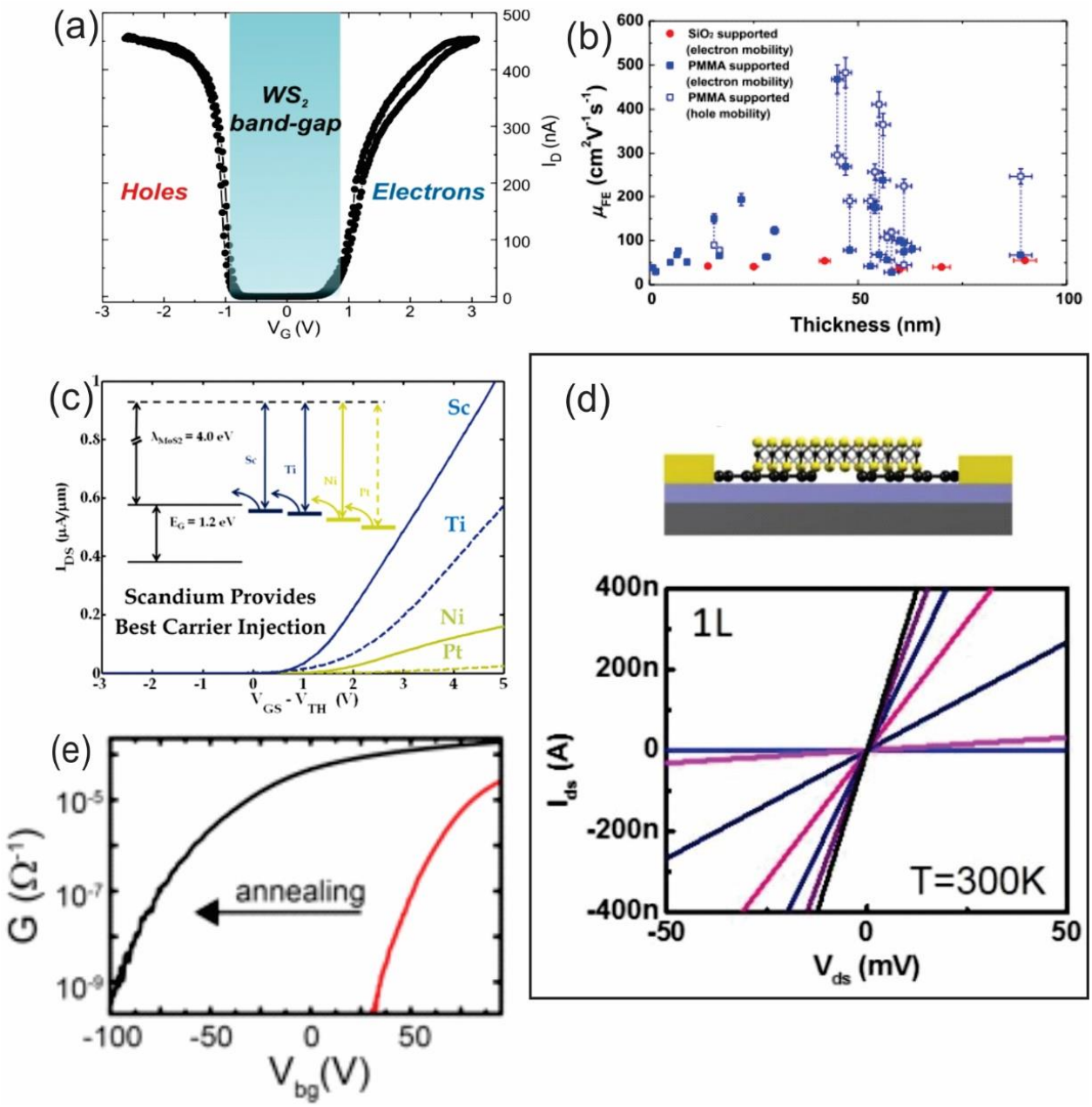

Figure 2.6 Factors influencing 2D-TMD FET device performance. (a) Transfer characteristic of a WS_2 ionic liquid-gated FET measured at V_D = 0.1 V as a function of gate voltage V_G. Reproduced with permission.(*104*) (b) The field-effect mobilities of MoS_2 supported by SiO2 and PMMA as dielectric layer. Reproduced with permission.(*105*) (c) Transfer curves of MoS_2 FET using metal contacts with different work functions. Reproduced with permission.(*106*) (d) Above is the device structure of monolayer MoS_2 with graphene contacts. Blow is the linear I_{ds}-V_{ds} curve of the device. Reproduced with permission.(*107*) (e) The transfer curves of monolayer MoS_2 based FET before (red) and after (black) in situ annealing. Reproduced with permission.(*108*)

2.3.2 Devices based on TMDs Vertical Heterostructure

Vertical heterostructure based on TMDs and other 2D materials have been occupied in many devices, including electronic devices (such as diodes and tunneling field effect transistors), optoelectronic devices (such as photodetector and photovoltaic cells) and other bio-devices.

2.3.2.1 Electronic Devices

Graphene/TMDs Devices

Because the zero bandgap and Klein tunneling of graphene makes it hard to attain low power dissipation in the OFF state, graphene is not considered to be a promising candidate for FET application. However, combining graphene with hBN or other TMDs materials vertically to form a tunneling field-effect transistor (TFET) is able to achieve a high ON/OFF current ratio at room temperature. As the name indicates, the TFET is based on the quantum tunneling. This TFET based on all 2D materials was first realized by Britnell in 2012 (**Figure 2.7**a).(*110*) Atomically thin hBN or MoS_2 was sandwiched between two layers of graphene, acting as vertical transport barriers in the TFET. Switching-ratios as high as 50 and 200 are observed in graphene/hBN/graphene and graphene/MoS_2/graphene devices, respectively. The operation of the device is mainly dependent on the modulation of the density of states in graphene and the effective tunneling barrier height adjacent to the graphene electrodes by the gate voltage, as shown in **Figure 2.7**b and c**.** As the transit time associated with tunneling is very short, this type of TFET is suitable for high frequency operation. Later on, graphene/WS_2/graphene vertical TFET was also realized by T. Georgious.(*111*) The operation principle of their device is very similar to what was proposed by Britnell, but the lower barrier height brought by the WS_2 was fully used to tune the device between tunneling (under the barrier) to thermionic (over

the barrier) transport. The combination of both transport behaviors allows for unprecedented high ON/OFF ratio (10^6) and large ON current at room temperature.

TMD/TMD devices

Diode is one of the important parts in electronic devices. The Shockley diode equation is used to describe the rectifying behavior of diodes, as shown below:

$$\mathrm{I} = I_s(e^{\frac{V_D}{nV_T}} - 1) \qquad \text{(Eq.2-2)}$$

Where I is the current passing through diode, I_s is the reverse saturation current, $V_D$is the applied voltage across the diode, $V_T$is the thermal voltage (V_T= kT/q, k is the Boltzmann constant, T is the temperature, q is the elementary charge), n is the ideality factor. If the diode is ideal, the ideality factor is equal to 1. In real diodes, because of carrier recombination and other junction imperfections, the ideality factor varies between 1 and 2. When ideality factor equals to 1, it represents that the recombination is limited by minority carrier. If it equals to 2, it means the carrier recombination is limited by both carrier types.

By vertically stacking synthetic p-doped monolayer WSe_2 and exfoliated n-doped MoS_2 flake, an atomically thin heterostructure based p-n diode with a sharp interface was formed (**Figure 2.7**d).(*112*) The ultrathin p-n diode was observed to exhibit an obvious rectification behavior, with the current being only able to pass through the device when the positive bias is applied to WSe_2, as shown in **Figure 2.7**e. Based on the fitting model of the diode characteristics, the ideality factor was calculated to be 1.2 at zero gate voltage. The ideality factor closes to 1 signifies the superb diode behavior of the atomically sharp interface. The rectification behavior can also be well modulated by the gate voltage.

In normal cases, artificially stacking differently doped monolayer TMDs (such as MoS_2 and WSe_2) forms a type-II band alignment in the vdW heterojunction. By electronically tuning

the band gap from type-II to type-III, vertical tunneling of electrons from the valence band from one layer to the conduction band of another layer can be activated, which is named as band-to-band tunneling (BTBT). The first realization of such device was based on vertical MoS_2/WSe_2 coupled with a dual-gate (**Figure 2.7**f).(*113*) When the two gates are biased at opposite polarities so that MoS_2 and WSe_2 are strongly n-doped and p-doped, the tunneling transported was observed in the reverse direction (**Figure 2.7**g). The BTBT was later confirmed to be stronger at the edge of the MoS_2/WSe_2 heterostructure in the horizontal direction, compared with that in the out-of-plane direction in the overlapping region.(*93*) The BTBT was also observed in heterostructures comprised with other materials, such as $WSe_2/SnSe_2$, with single-gate structure.(*114*)

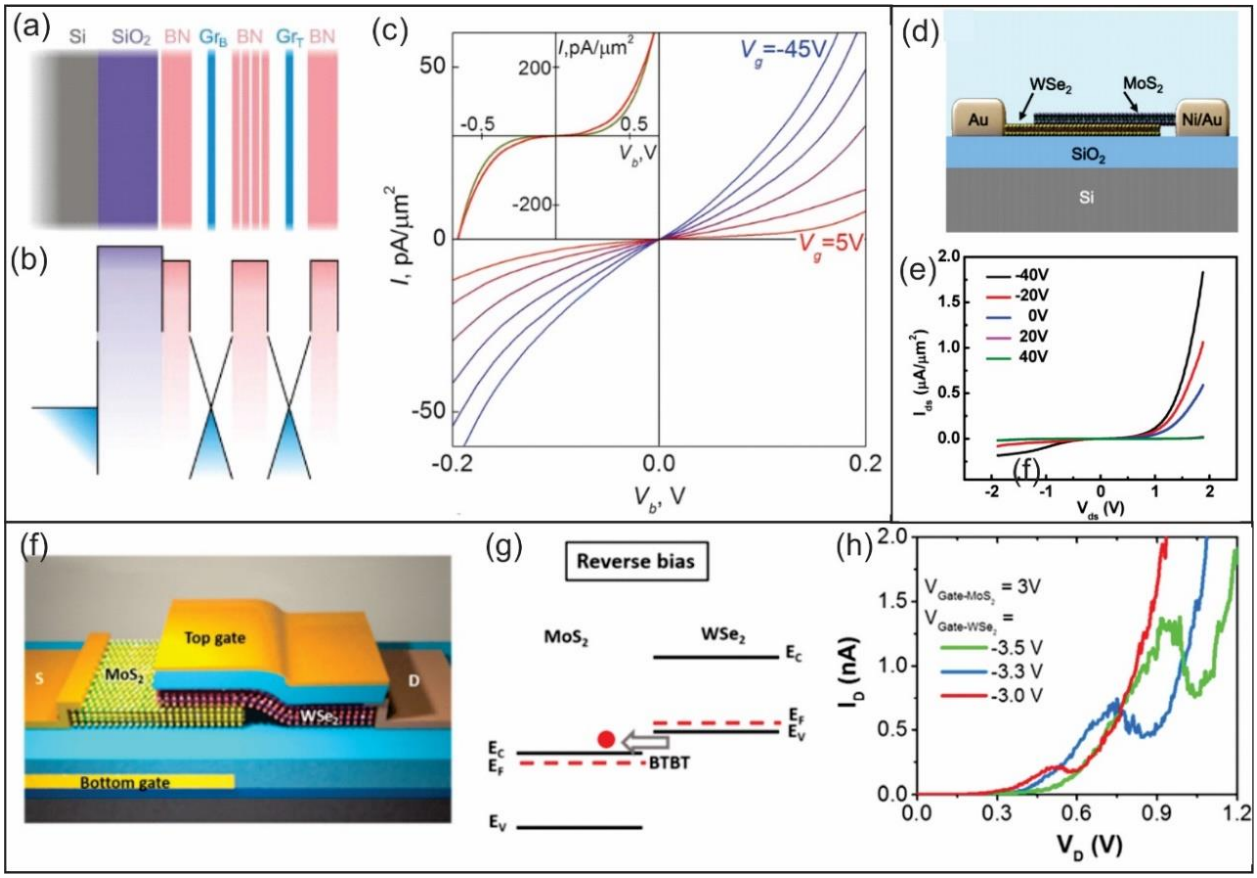

Figure 2.7 Van der Waals heterostructure based electronic devices (a) Schematic structure of graphene/BN/graphene tunneling transistor. (b) Band diagram of the graphene/BN/graphene tunneling transistor with no source-drain bias and gate voltage. (c) Tunneling source-drain current modulated by gate voltage. Inset is the comparision between experimental result and theory. (a-c) Reproduced with permission.(*110*) (d) Schematic diagram of the side-view of the $WSe_2/MoSe_2$ vertical heterostructure diode. (e) Gate-tunable current rectification behavior of $WSe_2/MoSe_2$ p-n diode shown in (d). (d,e) Reproduced with permission.(*112*) (f) Schematic of MoS_2/WSe_2 vertical tunneling transistor, with MoS_2 modulated by bottom gate and WSe_2 modulated by top gate. (g) Energy band diagram of BTBT under reverse bias. (h) Negative differential resistance observed under the forward bias. (f-h) Reproduced with permission.(*113*)

2.3.2.2 Photodetectors devices based on the vertical heterostructures

vdWHs based on 2D materials exhibits a variety of novel optical properties as we have mentioned above and their applications in optoelectronics and photon harvesting technologies are also promising. Fundamental working mechanisms and recent progress of 2D vdWHs including TMDs materials and graphene in a photodetector are reviewed below. Photodetectors

convert absorbed photons into electrical signal, which is the core of technologies in our lives, such as imaging, optical communication, night-vision and so on. It is very important to understand the mechanisms for the photocurrent generation in the vdWHs. The main mechanisms for the generation of photocurrent in vdWHs are photoconductive, photovoltaic, photo-thermionic and tunneling effect. In most cases, the photocurrent observed experimentally is actually the combination of more than one effect.

Some of the important figure of merits to describe the performance of photodetectors are first described as follows:

Photoresponsivity (R, unit: $A \cdot W^{-1}$) is the electrical response to the incident light power, which is expressed as:

$$R = \frac{I_{\text{ph}}}{P_{\text{laser}}} \qquad \text{(Eq.2-3)}$$

I_{ph} is the generated photocurrent, P_{laser} is the power illuminated on the device.

Photoconductive gain is defined as the ratio of the number of charge carriers for the photocurrent and the number of generated electron-holes per second. The formula is as follows:

$$G = \frac{Rhv}{e \cdot \eta_{abs} \cdot \eta_{tra}} \qquad \text{(Eq.2-4)}$$

The electrons and holes contribute to the photocurrent until they recombine. If the mobility of holes is much slower than that of electrons, electrons can circulate multi-times and contribute to the photocurrent, before they recombine. So, the photoconductive gain can also be expressed as the ratio of the photogenerated carrier lifetime and the transit time:

$$G = \frac{\tau_{photocarriers}}{\tau_{transit}} = \frac{\tau_{photocarriers} \cdot \mu . V}{L^2} \qquad \text{(Eq.2-5)}$$

η_{abs} is light absorption efficiency, η_{tra} is the charge transfer efficiency, h is the Planck constant, v is the frequency of the incident light, R is the photoresponsivity, e is the elementary

charge, $\tau_{photocarriers}$ and $\tau_{transit}$ are the lifetime and the transit time of the photogenerated carrier, μ is the charge carrier mobility, V is the source-drain bias, L is the channel length.

External quantum efficiency (EQE, unit: %), an important parameter of photodetectors, represents the number of charge carrier collected for the generation of photocurrent per photon shining on the device:

$$EQE = (\frac{I_{ph}}{e})/(\frac{P_{\text{laser}}}{hv}) \quad \text{(Eq.2-6)}$$

While internal quantum efficiency (IQE, unit: %) is the ratio of the number of charge carriers collected per photon absorbed by the photodetector. Based on the definition, IQE is always larger than EQE, and the EQE/IQE equals to the absorption of the photon by the devices.

Photoconductive effect

Photoconductive effect relies on the resistance change of the photoactive channel layer by absorbing the incident photons. The generated electron-hole pairs are separated by the external electric field and drift towards the opposite direction to the electrodes, resulting in a photocurrent. This photocurrent generally adds to the dark current and thus decreases the whole resistances of the device.

Most of the TMDs-photodetectors operated under photoconductive effect have a metal-TMD-metal configuration. Photogain, as we have mentioned above, is an important figure of merit of photodetectors. One of the advantages of photoconductive-based photodetectors is that they can have a photogain higher than unity, which is resulted from charge traps. One type of the charge carriers is trapped and another one circulates multiple times until recombination. The trapped charges usually give rise to another photoconductive effect-photogating effect. They act as local gates and effectively modulate the local doping level of the channel. Photogating can be identified with a horizontal shift of the threshold voltage or the neutral point

under illumination. The direction of the shift indicates the polarity of the trapped charges. Using graphene as the electrodes to reduce the contact resistance, and using TMDs heterobilayer as the photoconductive channel to form the type-II band alignment to trap one type of charge carrier to achieve photogain as high as 3.4×10^4 has been reported by Jamie *et al.* The device structure and results are shown in **Figure 2.8**.(*115*)

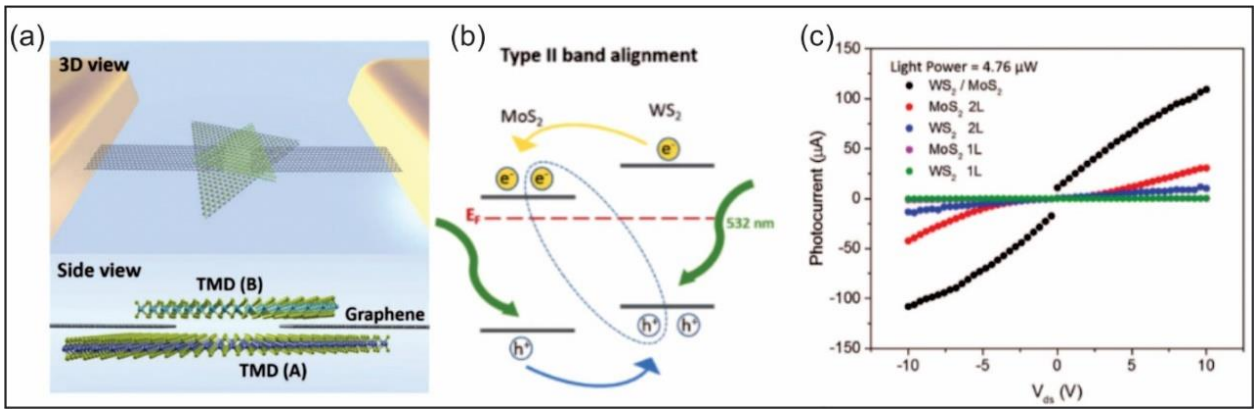

Figure 2.8 Vertical heterostructure based photodetector using photoconductive mechanism (a) Schematic of the top and side view of the Gr-TMD heterobilayer-Gr photodetector. (b) Photogenerated electrons and holes accumulated in different layers. (c) Photocurrent comparision of photodetectors with different photo-active layers. Reproduced with permission.(*115*)

Photovoltaic effect

In the photovoltaic effect, the electrons-hole pairs are separated by an internal electric field. The internal electric field is often generated near the Schottky barrier at the interface of the TMDs and metal electrodes or PN junction. The I_{ds}-V_{ds} curve generated from photovoltaic effect is typically non-linear. When light illuminates on the device, the photogenearted electron-hole pairs are quickly separated by the built-in field. If the circuit is open, the charges accumulate to generate open-circuit voltage (V_{oc}) and short-circuit current for the closed circuit (I_{sc}). Photodiodes based on two atomically thin TMDs with different doping levels are constructed to act as photodetectors working with photovoltaic effect.(*112*) External quantum efficiency (EQE) around 12% for atomically thin WSe_2/MoS_2 was attained, as shown in **Figure**

2.9a and b. The relatively low EQE was found to be strongly influenced by the interlayer recombination dominated by (a) Shockley–Read–Hall (SRH) recombination assisted by inelastic transition of majority carriers into trap states within the bandgap; (b) Langevin recombination by Coulomb interaction. The Langevin recombination is also named bimolecular recombination. In brief, when an electron is within a coulomb radius of an arbitrary hole, they are attracted to each other by Coulomb force. If the Coulomb force is larger than the thermal energy, the attracted electron and hole will recombine. In pristine 2D systems, due to the enhanced Coulomb interaction between electrons and holes, Langevin recombination plays a dominant key role compared with SRH recombination. The recombination rate can be further tuned by gating. In addition, enlarging the band offset for conduction bands (ΔE_C) and valence bands (ΔE_V) at the junction can contribute to the separation of the electron-hole pairs. Generally, the charge transfer processes in the ultrathin p–n junctions are efficient and fast. Sandwiching thick TMDs between graphene electrodes was also a widely studied structure utilizing photovoltaic effect for photodetection application. Britnell *et al*. reported a heterostructure of graphene/WS_2(5-50nm)/graphene. The schematic diagram of the device structure is shown in **Figure 2.9**c.(*116*) EQE as high as 30% was achieved in their devices. Unlike the photodiodes comprised with two ultrathin TMD materials, which has an intrinsic built-in electric field, their heterostructure devices do not show intrinsic electric field. Instead, because of the vertical structure, the electric field can be induced and modulated with external gating (**Figure 2.9**e and f), which further separates the photo-generated electron-hole in WS_2 and brings about current.

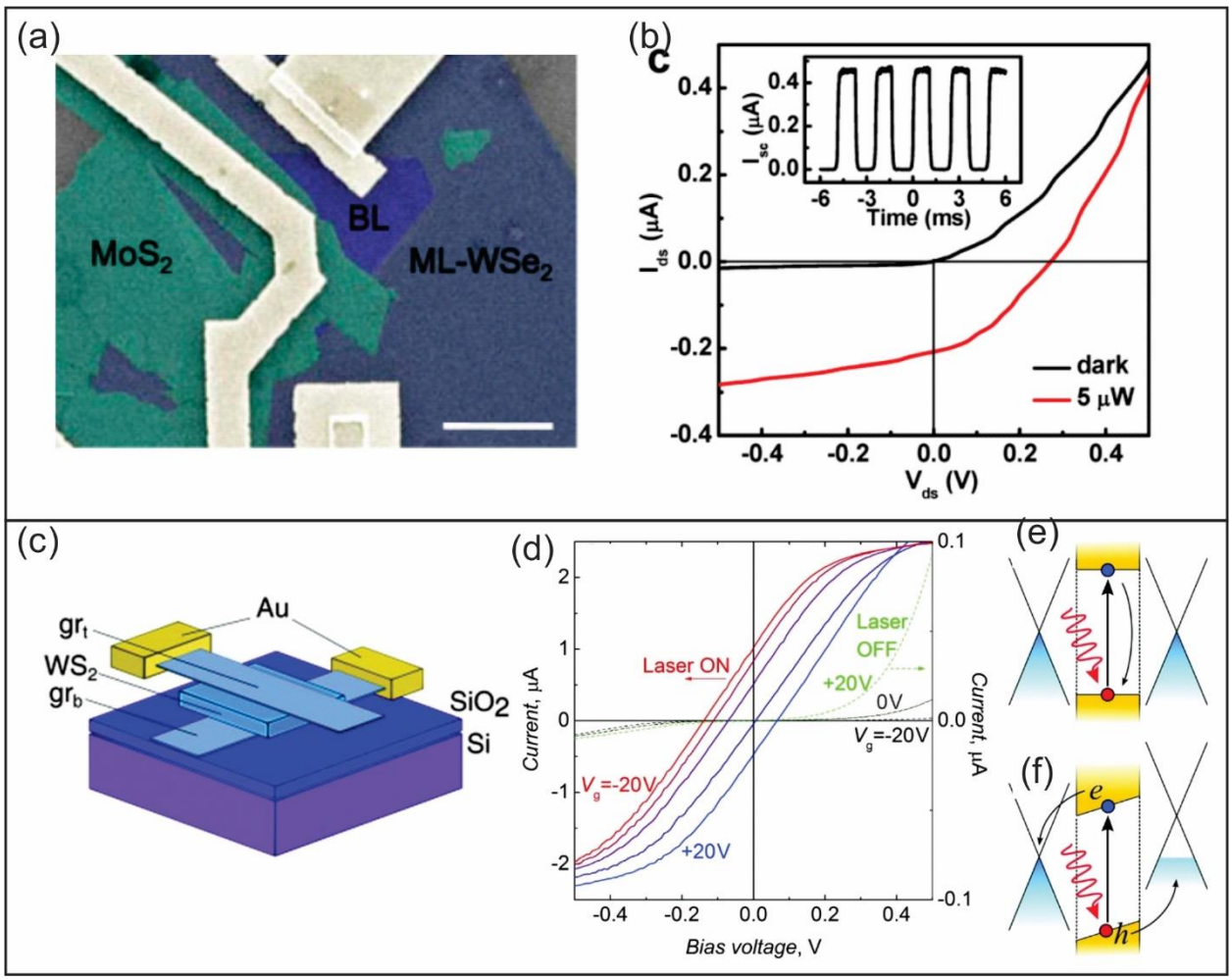

Figure 2.9 Photovoltaic effect in van der Waals heterostructures (a) False color SEM image of WSe_2/MoS_2 vertical heterostrcture BL and ML-WSe_2 are distinguished with different colors. Scale bar is 3μm. (b) IV results of the vertical heterostructure-based device in (a) under dark and illumination (514nm). Inset is the temporal response of the photocurrent under 514nm illumination. (a,b) Reproduced with permission.(*112*) (c) Schematic of the graphene/WS_2/graphene vertical device. (d) Output curves of device in (c) with laser on and off under different gate voltage. (e,f) The graphene/WS_2/graphene energy band diagram and transport of photo-generated electrons and holes in the vertical device (e) without and (f)with a built-in electric field. (c-f) Reproduced with permission.(*116*)

Photo-thermoelectric effect

Graphene has strong electron-electron interaction and weak electron-phonon interaction, which leads to ultrafast heating of the charge carriers in graphene. Under global illumination, two graphene with different doping levels can generate a temperature difference ΔT. This property of graphene has been used for the generation of photovoltage through Seebeck effect

(photo-thermoelectric effect - PTE). The equation for this effect is usually expressed as: $V_{PTE} = (S_1 - S_2)\Delta T$, where $S_{1,2}$ is the Seebeck coefficient of two graphene, while ΔT is the temperature difference in the two graphene regions. Graphene p-n junction controlled by sub-micrometer gates was realized for photocurrent generation through thermoelectric effect by Marcus(*117*) as shown in **Figure 2.10**a. As can been seen from **Figure 2.10**b, the photocurrent was mostly generated near the edges of top gate and the source drain electrodes, where the p-n junction forms. With gate voltage, the photodetection of graphene p-n junction can be switched between on and off. With this kind of device structure, broadband photodetector can be realized, but the temperature difference is always very small. Koppens *et al*.(*118*) fabricated a graphene/WSe_2/graphene heterostructure based photodetector to detect photons with low energy via photo-thermionic effect. The device structure is presented in **Figure 2.10**c. The working principle is illustrated in **Figure 2.10**d. It also makes use of the strong e-e interaction in graphene to generate hot electron bath. Some of the electrons get energy to excite to higher energy level from the heat bath, followed by transferring through the WSe_2 barrier to the graphene in other side. Via modulating the Schottky barrier formed between graphene/WSe_2 with gate voltage, the photocurrent can be further enhanced.

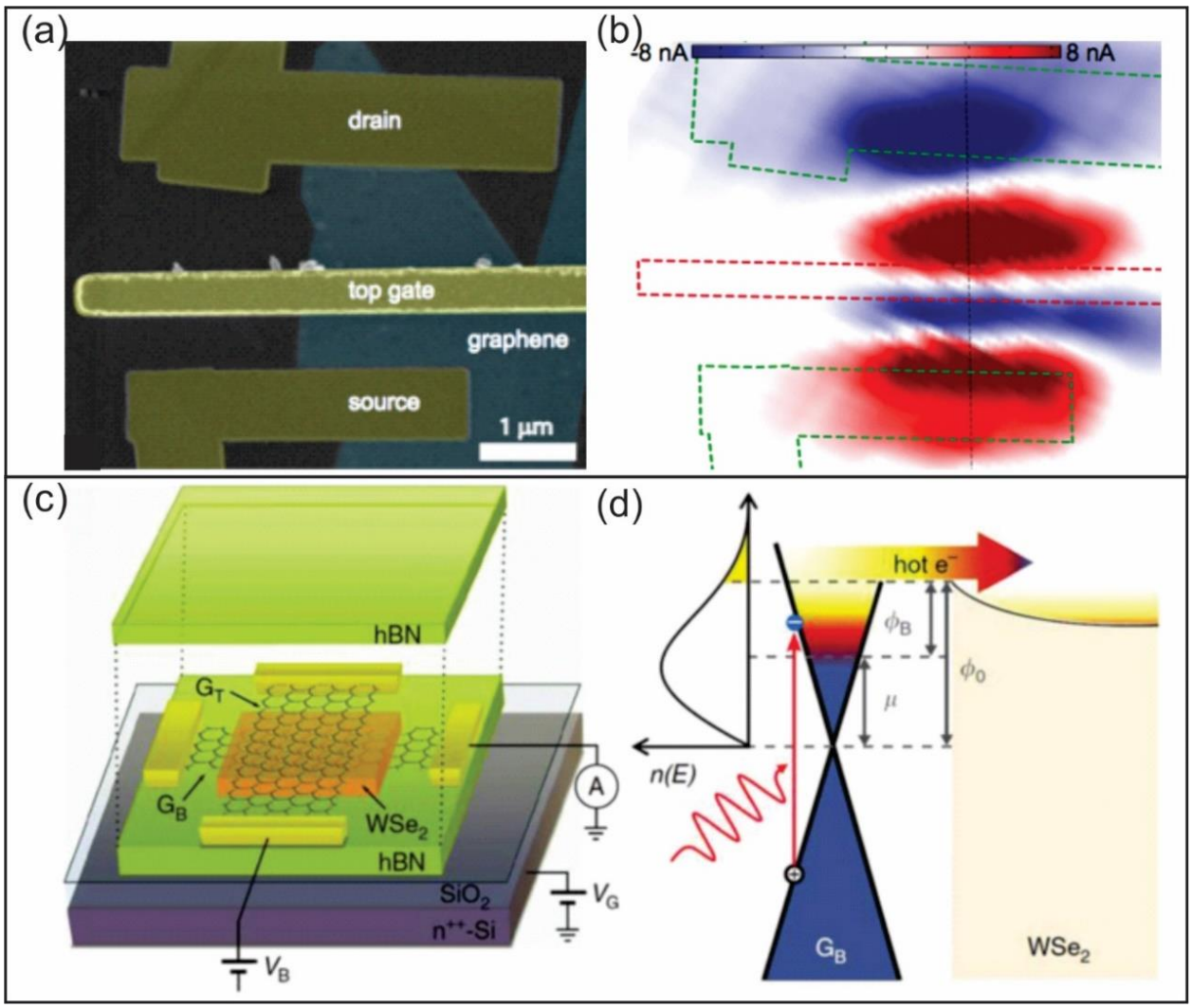

Figure 2.10 Photo-thermoelectric effect photocurrent in van der Waals vertical heterostructure (a) False-color SEM image of graphene p-n junction based photodetector. (b) Photocurrent mapping of the graphene device from photothermoelectric effect. (a,b) Reproduced with permission.(*117*) (c) Schematic of graphene/WSe_2/graphene vertical device and the circuit for the photocurrent measurement. (d) Energy band diagram of photothermionic effect between graphene and WSe_2 interface. (c,d) Reproduced with permission.(*118*)

Tunneling effect

A room temperature Esaki tunneling diode for photodetection application was first realized in black phosphorus (BP)/tin diselenide ($SnSe_2$) vdWHs by creating a broken-gap energy band offset. The optical image of this device is shown in **Figure 2.11**a. However, the generation of the photocurrent in this type of tunneling diode is not directly through tunneling. Instead it is from the accumulation of the electrons and holes in $SnSe_2$ and BP separately due

to the broken-gap energy band offset,(*119*) as shown by the energy band diagram in **Figure 2.11**b. This kind of photocurrent generation mechanism is not common to see. The responsivity reported is not high, around~0.24 mA/W. Another photocurrent generation mechanism is photogenerated electrons (or holes) tunneling through either an insulator barrier or a vdW gap from one layer to another layer. Yu *et al*. reported a highly sensitive heterostructure based on MoS_2/hBN/graphene by introducing hBN as the tunneling barrier (**Figure 2.11**c).(*120*) The dark current (direct tunneling-DT) can be severely reduced by the hBN barrier compared with the photocurrent (Fowler-Nordheim tunneling-FNT), so that to achieve a high photoresponsivity (180 AW^{-1}) (**Figure 2.11**d). For graphene/TMD/graphene vertical heterostructure photodetector, if the TMD is ultrathin, the barrier height formed between TMD and graphene can play a dominate role in generating the photocurrent (**Figure 2.11**e and f). Duan *et al*. made use of the asymmetric tunneling barrier height between top graphene/MoS_2 and bottom graphene/MoS_2 induced by different doping levels of both top and bottom graphene to generate photocurrent in graphene/MoS_2 (1L)/graphene vertical heterostructure (**Figure 2.11**e-g).(*121*)

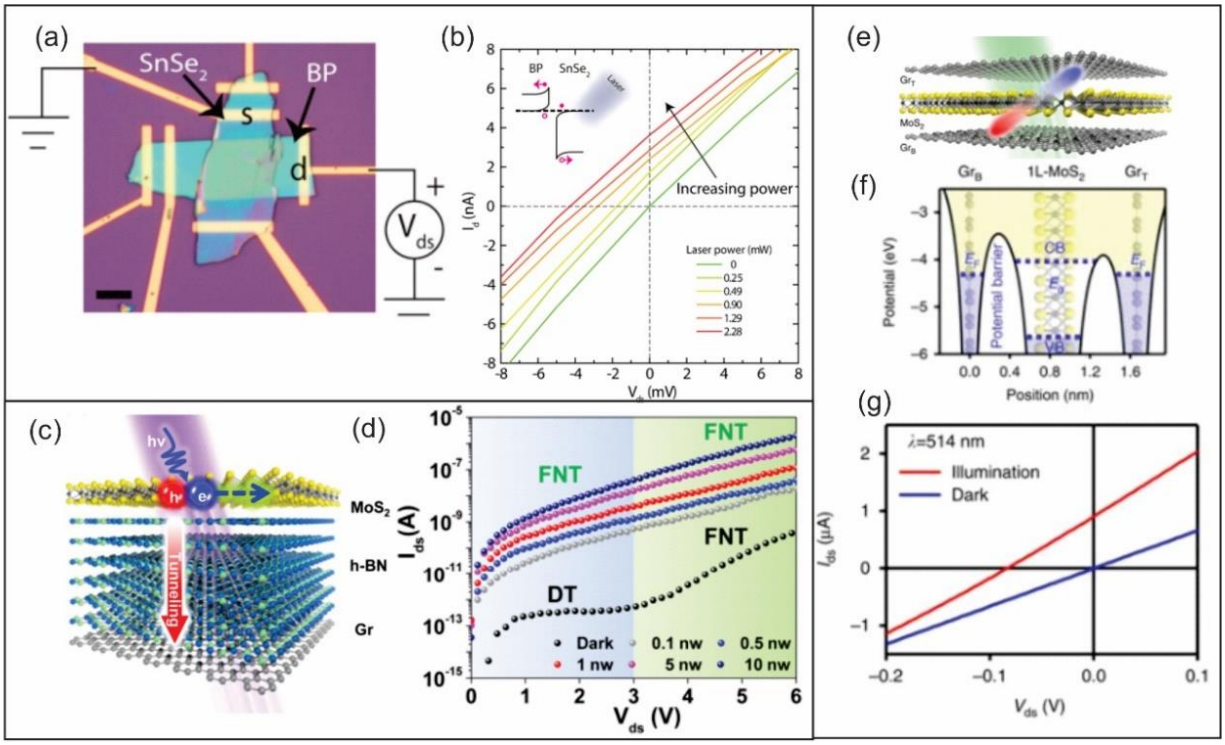

Figure 2.11 Tunneling photocurrent in van der Waals heterostructure (a) Optical image of BP/$SnSe_2$ vertical heterostructure diode. During the measurement, $SnSe_2$ is grounded. (b) The I_{ds}-Vds results of the diode with increasing laser power. Inset is the broken energy band alignment of BP/$SnSe_2$ illustrating the process of photocurrent generation. (a,b) Reproduced with permission.(*119*) (c) MoS_2/multilayer hBN/graphene vertical photodetector. Electrons and holes are generated in MoS_2, with holes tunneling through the thick hBN to graphene and electrons transporting in MoS_2. (d) I_{ds}-V_{ds} results of the vertical photodetector with increasing laser power. (c,d) Reproduced with permission.(*120*) (e) Schematic of vertical graphene/monolayer MoS_2/graphene structure. Holes and electrons are generated in MoS_2 and transfer to bottom and top graphene respectively. (f) Energy band diagram of graphene/monolayer MoS_2/graphene with van der Waals gap between graphene and MoS_2 acting as tunnelling barrier. (g) I_{ds}-V_{ds} characteristics of the device in figure (e) under laser illumination of 514 nm laser (red line) and dark (blue line).(e-g) Reproduced with permission.(*121*)

2.4 Production Methods of 2D Materials based Heterostructures

The 2D material individual layers production methods have been reported in many review papers, (*122*) so in this part, I will only focus on the production methods for 2D materials-based heterostructures. Generally speaking, two categories of approaches are adopted

to fabricate heterostructures: top-down and bottom-up. Top-down method is stacking mechanically exfoliated or CVD synthesized 2D materials artificially. In bottom-up method, a top layer is directly synthesized on another CVD grown or exfoliated 2D material with CVD method.

2.4.1 Chemical Vapour Deposition (CVD)

CVD method has been widely adopted for synthesis of large-area 2D materials. Recently, it has been also used to grow various 2D stacks. The heterojunctions synthesized with CVD method produce a much cleaner interface for fundamental research and thus better device performance.

Several investigations have been carried-out on various TMDs-based heterostructures, mostly grown by CVD method. TMD/TMD vertical heterostructures are the most extensively studied. One-step CVD method was first created for the direct synthesis of TMD-based vertical heterostructures. Gong *et al*. reported a scalable single-step CVD method for the creation of high quality WS_2/MoS_2 vertical and lateral heterostructure.(*123*). A schematic setup for the growth of WS_2/MoS_2 heterostructure is shown in **Figure 2.12**a. Molybdenum trioxide (MoO_3) powder was placed upstream in the tube as the precursor of the MoS_2, while a mixture of W and Te powder were scattered on the SiO_2/Si substrate for the growth of WS_2. S powder was put in front of MoO_3. The differences in the nucleation and growth speed lead to the growth sequence of MoS_2 and WS_2. The vertical and lateral heterostructures can be synthesized in different temperature zones. A two-step CVD method for the TMD/TMD vertical heterostructures production was later demonstrated by the same group. Compared with one-step CVD method, two-step method has the capability of spatial and size control, also minimizes the cross-contamination.(*124*) In their experiment, a well-defined 2H and 3R stacking in the $WSe_2/MoSe_2$ bilayer region and a much sharper in-plane interface was obtained compared with the one-step growth. The detailed process is descried in **Figure 2.12**f. A layer

of $MoSe_2$ was firstly produced by the traditional CVD on SiO_2/Si substrate using MoO_3 and Se powder as the precursors under 750℃. The as-grown $MoSe_2/SiO_2$/Si was then transferred into another CVD setup for the WSe_2 synthesize, using WO_3 and Se powder as the precursors, with a higher growth temperature (900℃). By controlling the growth time in the second CVD step, type I and type II heterostructures can be formed, as illustrated in **Figure2.12**g. The optical images of monolayer $MoSe_2$, type I and type II $WSe_2/MoSe_2$ heterostructures are shown in **Figure 2.12**h-j.

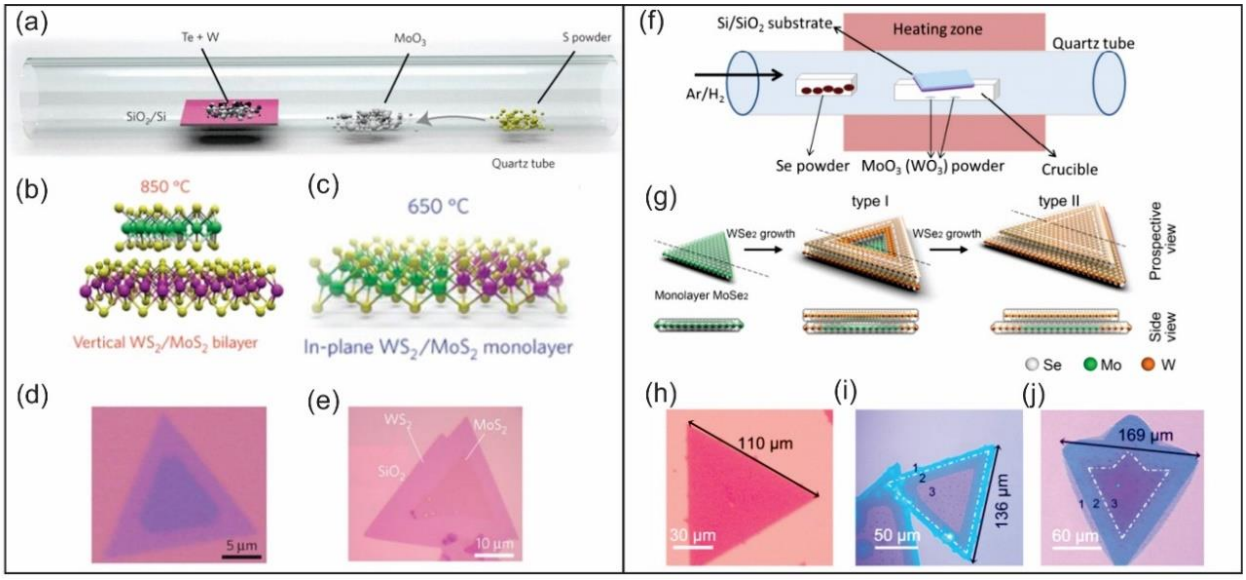

Figure 2.12 CVD method for vertical heterostructure synthesis (a) Schematic of the one step CVD synthesis for vertical heterostructure. (b)(c) Schematic of vertical and in-plane WS_2/MoS_2 structure synthesized under different temperatures. (d)(e) Optical images of the vertical and in-plane structure shown in (b) and (c). (a-e) Reproduced with permission.(*123*) (f) CVD setup of the two-step growth technique. (g) Schematic of $MoSe_2$-templated WSe_2 growth. Type-I is bilayer WSe_2 grown in-plane with $MoSe_2$. Type-II is WSe_2 grown both on top of and in-plane with MoS_2. (h-j) Optical images of monolayer $MoSe_2$, type-I and type-II heterostructure. (f-j) Reproduced with permission.(*124*)

2.4.2 Mechanical Exfoliation-Artificial Stacking Assembling

Unlike CVD based direct synthesis of heterostructures, in which the orientation of the vdWHs between layers is relatively fixed, mechanically stacking different layers to assemble heterostructures provides more freedom to adjust the alignment between layers. In addition, the

high temperature in the second CVD process always unavoidably causes damages to the prior layers.

Mechanically exfoliated or CVD synthesized 2D layered materials can be manually stacked to form vertical heterostructures.(*125*) Generally speaking, with the assist of either the wet or the dry transfer method, a second layer of TMDs was transferred onto the first pre-transferred layers at a specific location to fabricate various 2D TMD-based heterostructures. The schematic illustration of the fabrication process is shown in **Figure 2.13**a. Wet transfer is usually used when the 2D materials are CVD synthesized. CVD synthesized materials are always with high coverage and large domain size, so that a precisely located transfer of the second layer is not very necessary. The wet transfer method will be described in the methodology section. The dry transfer method is used for the transfer of the mechanically exfoliated 2D materials. To be specific, an exfoliated or CVD synthesized bottom layer of TMD is transferred onto the target substrate. Then, a layer of polymer is spin-coated on the top of the second layer of TMD material, followed by the attachment of a transparent stamp, usually poly dimethyl siloxane (PDMS). After that the PDMS with the sample is then attached to a slide. With the help of a microscope stage, the top layer can be placed in a well-defined position with any orientation with respect to the first layer. At last, the polymer is dissolved in chemical solution. Both partially and full vertical architectures of MoS_2/WS_2 heterostructures have been successfully fabricated by Huo *et al*., as shown in **Figure 2.13**b and c.(*126*) Wang *et al*. have also artificially stacked the monolayers of WSe_2 and WS_2 with various twist angles. The optical image is displayed in **Figure 2.13**d.(*127*)

Even though artificial assembling method enables the fabrication of various heterostructures, it may induce contamination between the vdWs interface thus affecting the final device performance. Additionally, the twist angle between layers is difficult to precisely control.

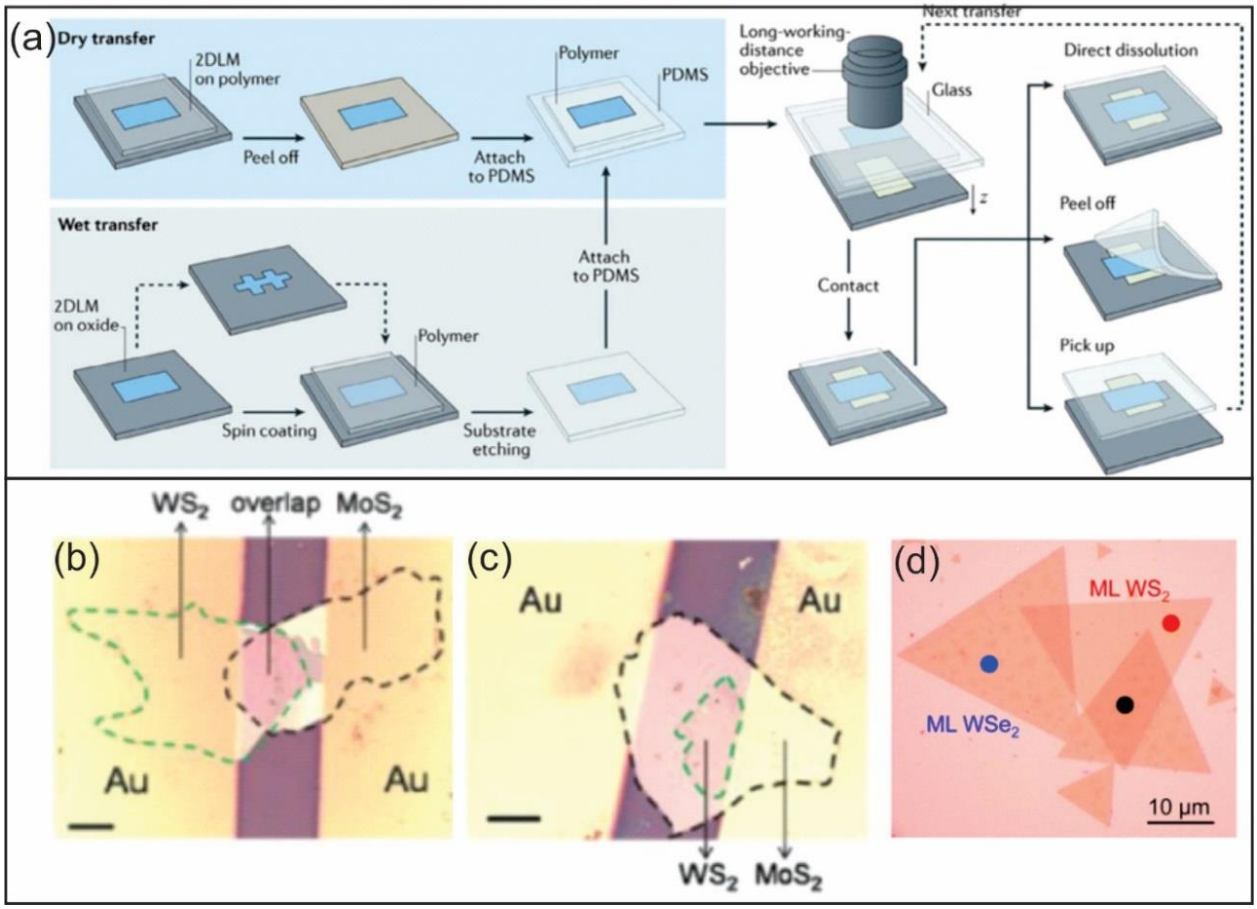

Figure 2.13 Transfer process of 2D materials for van der Waals heterostructures (a) Wet and dry transfer process of 2D materials for making van der Waals heterostructures. Reproduced with permission.(*125*) (b,c) Artificially stacked WS_2/MoS_2 heterostrcture in (b) partially vertical architecture and (c) fully vertical architecture. (b,c) Reproduced with permission.(*126*) (d) Artifically stacked WSe_2/WS_2 heterostructure with different twist angles. Reproduced with permission.(*127*)

Chapter 3 Device Fabrication and Characterization

3.1 Introduction

This chapter is focused on elaborating specific techniques which are exclusively employed to aid the progression of my project. It starts from materials synthesis, then device fabrication and ends with device characterization. The flow chart of the process is shown below:

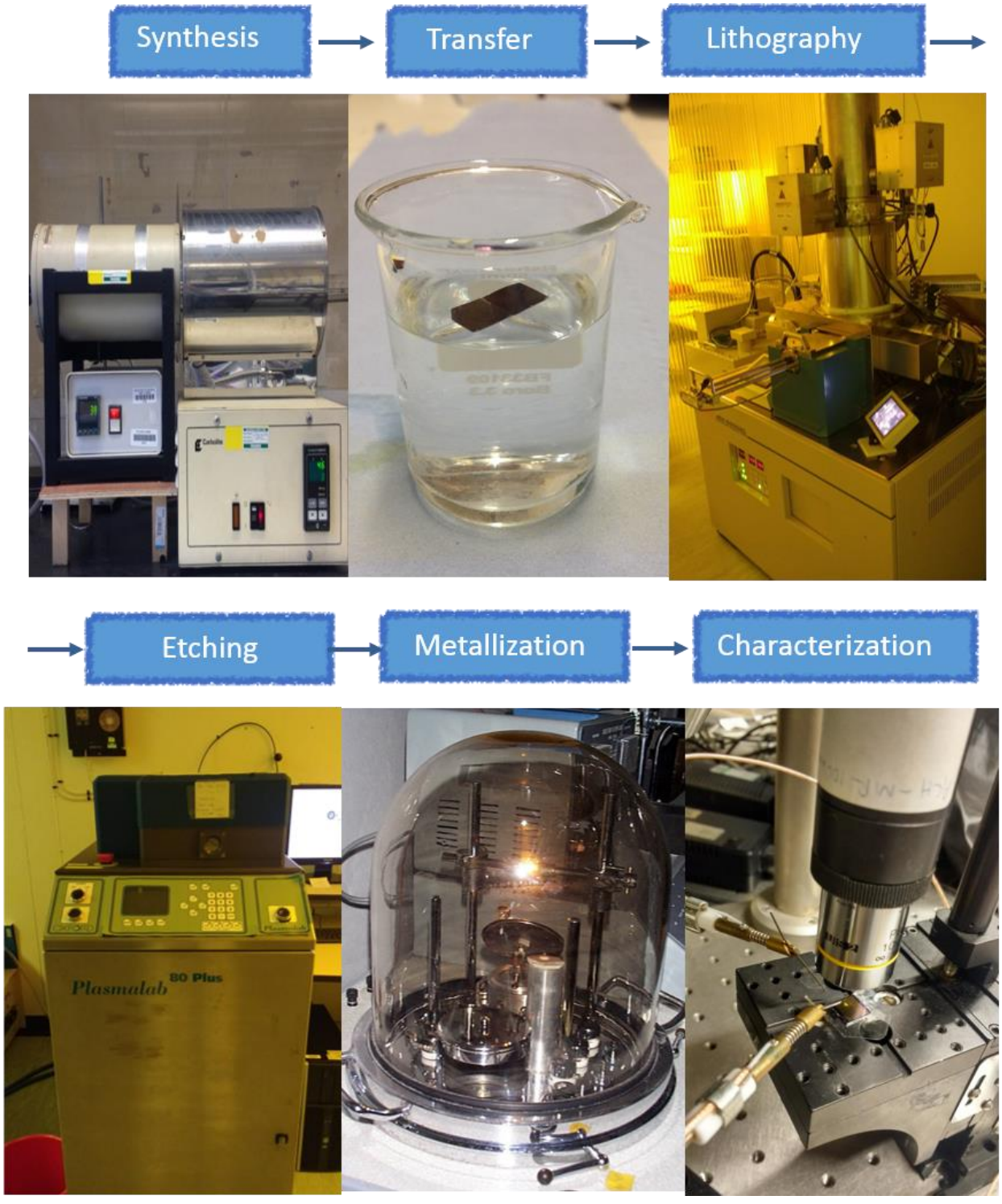

Figure 3.1 Photograph of the main techniques employed in my project.

3.2 2D Materials Synthesis

For all my projects, the CVD synthesized graphene and MoS_2 I used were provided by collaborators from my group. The ability to synthesize various 2D materials with large area

enables us to study devices with different heterostructures and also massive production of device arrays.

3.2.1 CVD Synthesis of Graphene

For the synthesis of graphene, a piece of copper foil was first polished by Brasso for 15 min and sonicated in diluted hydrochloric acid solution (HCl, 1 mol/L) to remove the residues on the copper surface. After this, the copper foil was sonicated in acetone and isopropanol (IPA) for 5 min to remove the organic residues. The copper was then placed in a 4-inch reaction tube. To ensure the uniformity of temperature during the whole growth process, the copper foil was positioned in the center of the furnace. 1% methane in argon (CH_4), 25% hydrogen in argon (H_2) and 100% argon (Ar) were used during the flushing and graphene synthesis process. Before the reaction started, the system was flushed with 1000 sccm Ar, 500 sccm H_2 and 50 sccm CH_4 for 30 min to remove the air inside the tube. After the flushing, the furnace was ramped to 1060 ℃ with the rising speed of 50 ℃/min accompanying with a flow of 600 sccm Ar and 300 sccm H_2. When the temperature reached the set value, the whole system remained the same condition to anneal the copper foil for 1 h. After the annealing process, the synthesis process lasted for 1 h at 1060 ℃ with the flow of 600 sccm Ar, 100 sccm H_2 and 20 sccm CH_4. The reaction was stopped by moving away the furnace from the sample position for the sample to be fast cooled to room temperature.

3.2.2 CVD Synthesis of WS_2

WS_2 was synthesized with a two-furnace system to control the temperature of sulfur powder (S) and tungsten trioxide powder (WO_3) separately. A 2×2 cm SiO_2 (300 nm)/p++Si substrate (University Wafer) was used as the growth substrate. The substrate was first sonicated in acetone for 15 min, then in 2-propanol (IPA) for another 15 min, followed by O_2 plasma for 15 min. After being cleaned, both the substrate and precursors were put into reaction tubes. 300 mg sulfur powder (≥99.5%, Sigma-Aldrich) was put in the outer tube (inner diameter was 22

mm) while the substrate was 41.5 cm from S powder at the downstream of the same tube. Another precursor, 200 mg WO_3 powder (≥ 99.5%, Sigma-Aldrich) in the inner tube (inner diameter was 12 mm), was 9.5 cm away from the center of the substrate. The tube with precursors and substrate inside was then put into the two furnaces, with S in the center of the first furnace while WO_3 in the center of the second one. Before reaction started, system was flushed with 500 sccm Ar for at least 30 min to remove the air inside. Then the first and second furnaces were set to ramp to 180℃ and 1170℃ at their maximum rising speed, respectively. The reaction process lasted for 3 min with Ar flowed at 250 sccm and the two furnaces stabilized at their set temperatures. 3 min later, reaction was stopped by decreasing the flow rate of Ar to 10 sccm, meanwhile, the first furnace was heated at the maximum rising speed to 450℃ to evaporate the rest S and the second one was cooled to room temperature at its maximum cooling speed. When the temperature of second furnace decreased to 950℃, the rest S was blown by Ar at a flow rate of 500 sccm.

3.2.3 CVD Synthesis of MoS_2

MoO_3 powder (≥99.5%, Sigma-Aldrich) and S powder (≥99.5%, Sigma-Aldrich) were employed to grow monolayer MoS_2 on SiO_2 (300 nm)/p++Si substrates (University Wafer). Atmospheric pressure CVD method was adopted to produce large MoS_2 domains, following the procedure reported previously. The temperatures of MoO_3 and S was controlled independently by placing them in separate furnaces. The precursor powders were loaded in two quartz tubes with different diameters (inner diameter to be 22cm and 12 cm, respectively), so that the reaction region could be strictly defined around the substrate surface. Argon (Ar) was introduced as the carrier gas. The MoO_3 and S powders and the SiO_2/Si substrate were heated to 310, 200, and 800 °C, respectively. The synthesis includes three stages: nucleation (25 min with 150 sccm Ar), main growth (30 min with 50 sccm Ar), and atom migration (10 min with 5 sccm Ar), which was finally ceased by a rapid cooling process.

As an example, **Figure 3.2** shows the setup and the process for synthesizing WS_2.

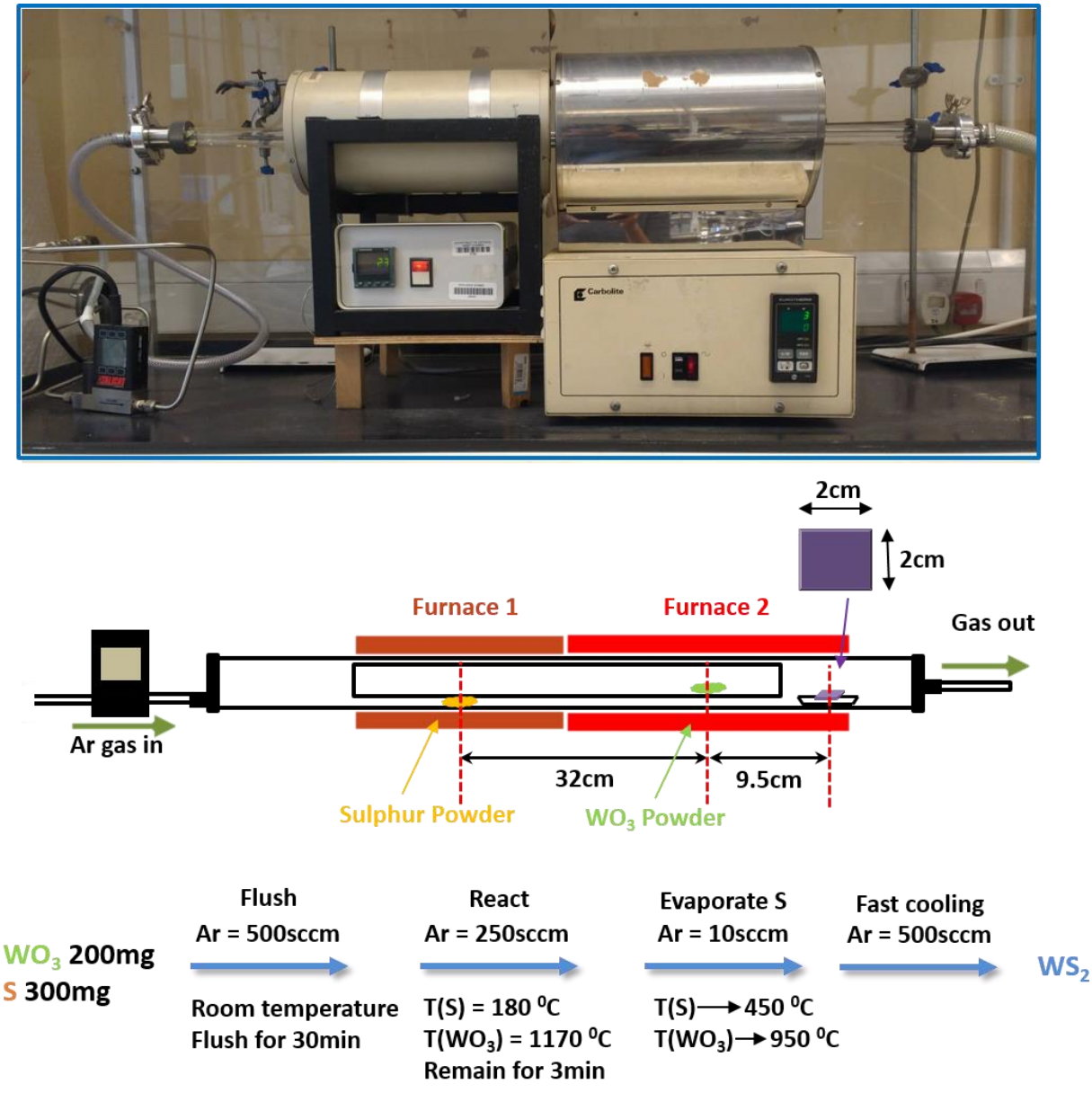

Figure 3.2 Photograph and the schematic of the CVD setup as well as the flowchart showing the main steps for WS_2 synthesis

3.3 Device Fabrication Process

3.3.1 2D Materials Transfer Method

Graphene was synthesized on copper foil. A layer of Poly (methyl methacrylate) (PMMA) was spin-coated on graphene/Cu foil as the transfer medium. The Cu foil was then

etched by the $(NH_4)_2S_2O_8$ solution (0.2 mol/L). The PMMA/graphene film was then transferred onto deionized water for three times (30 min each time) to remove the remaining $(NH_4)_2S_2O_8$. The WS_2 (or MoS_2) was synthesized on SiO_2/Si wafer. The PMMA/WS_2 (MoS_2) film was separated from the substrate by etching the SiO_2 with KOH solution (1 mol/L). After rinsing, the floating PMMA/graphene and PMMA/WS_2 (MoS_2) film were scoped with clean SiO_2/Si substrate and dried overnight at room temperature. Before soaked in acetone to remove PMMA, the samples were baked at 180℃ for overnight and 150℃ for 15 min for better adhesion for PMMA/graphene and PMMA/WS_2, respectively. Below shows the flowchart of the transfer process of TMDs I used in my projects.

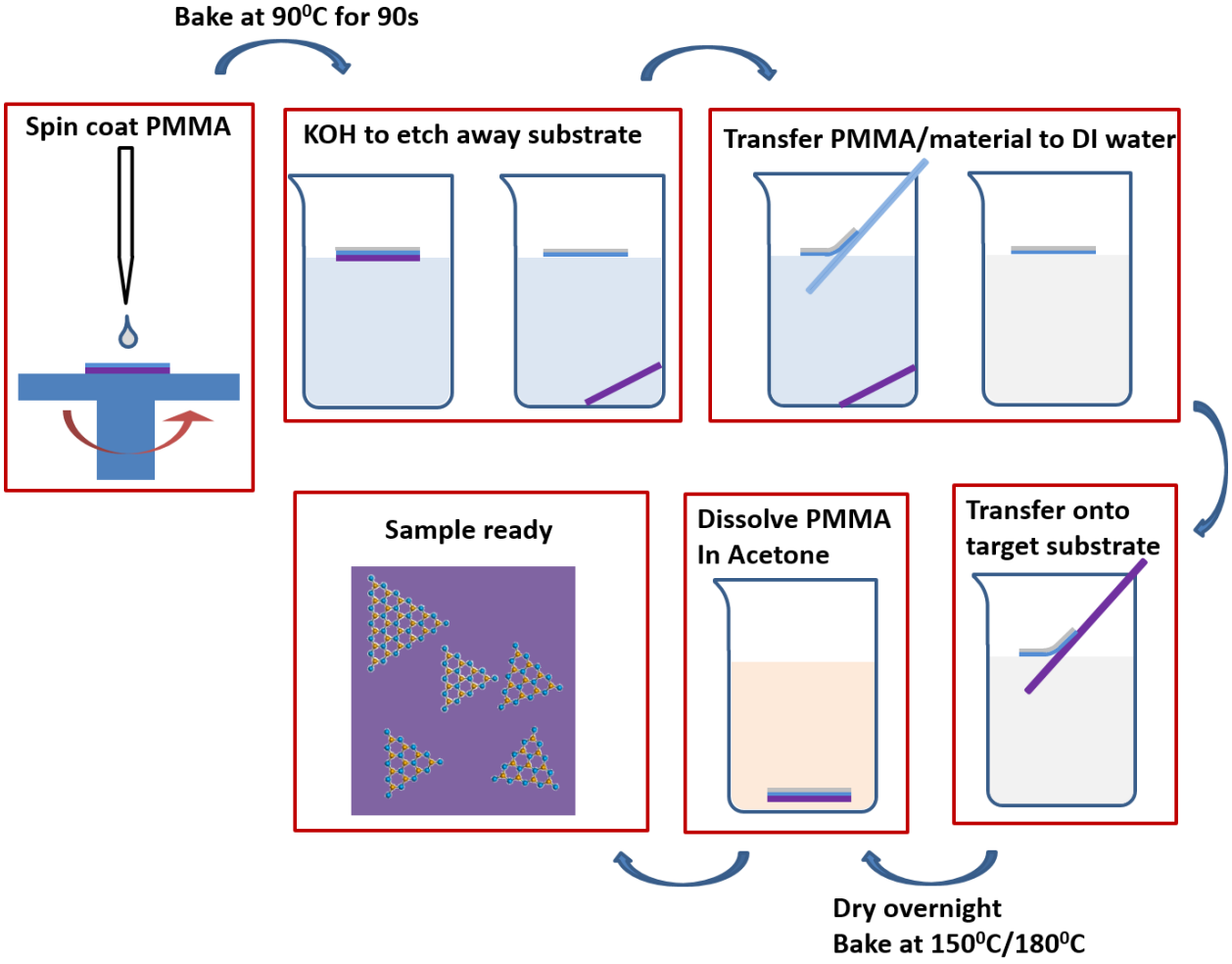

Figure 3.3 Schematic diagram of transferring WS_2 (MoS_2) from a SiO_2/Si substrate onto target substrate.

3.3.2 Electron-Beam-Lithography

Electron-beam-lithography (EBL) is a technique which uses a beam of electrons writing a custom pattern on a sample surface covered with electron-sensitive film. The electron-sensitive films are classified into two different categories: positive photoresist, which is removable by the developer after the electron exposure and negative photoresist, which is removable before the exposure but becomes non-removable after exposure. After developing, the custom pattern appears on the photoresist, which then transfer to the substrate by metal deposition (to form electrodes), etching (to pattern materials into custom shape) or other methods.

Positive photoresist is mostly used in my projects for the patterning of electrodes. Resist with light molecular weight has high dissolution rate, so bilayer positive photoresists are better for lift-off after metal deposition. A layer of PMMA-495K is spin-coated first with the spin speed of 4500 rmp for 45 s, followed by baking on hotplate at 180℃ for 90 s. Another layer of PMMA-950 K is then spin-coated on top with the same recipe. After exposed by electron-beam with the dose of 650 μC/cm^2, samples are developed in developer (MIBK : IPA = 1 : 3) for 45 s. Negative photoresist (maN-2403) is often used for the patterning of graphene ribbons. Because maN-2403 damages graphene, a layer of PMMA-495K is always inserted to isolate graphene from maN-2403. The PMMA-495K is spin-coated with the same recipe mentioned above while the maN-2403 is spin-coated at 3000 rmp for 30 s followed by baking at 90 ℃ for 90 s. The exposure dose for maN-2403 is 180 μC/cm^2. Samples are developed in ma-D525 for 150 s before reactive-ion etching. The equipment used is JEOL JBX-5500FS EBL system, with which features down to 10 nm can be patterned. For the patterning of WS_2 ribbons in *Chapter 4*, the EBL process adopted was the same as for graphene ribbons.

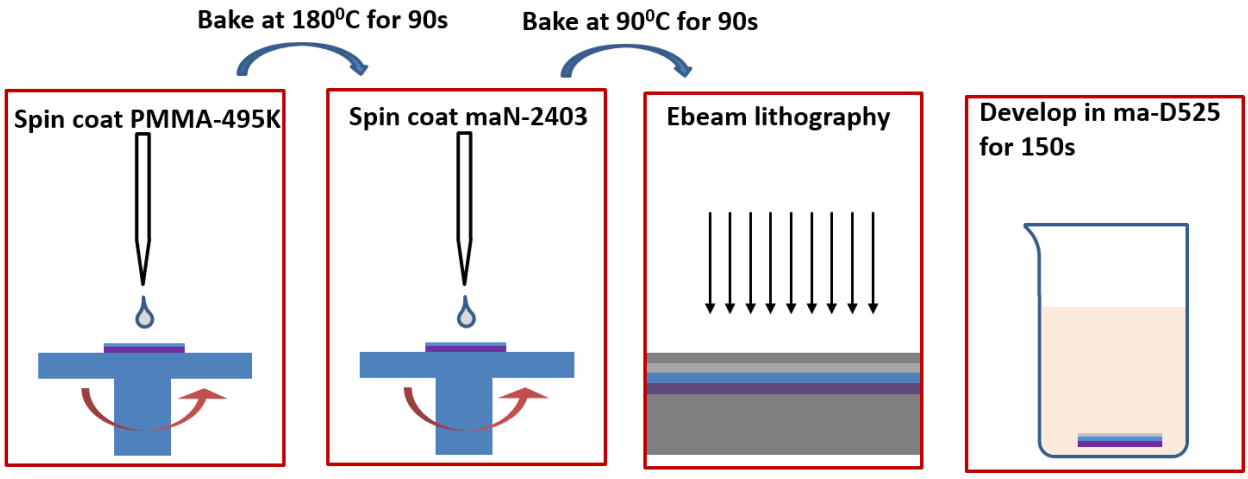

Figure 3.4 Schematic diagram of Ebeam lithography process for etching mateirals.

3.3.3 Reactive-Ion Etching

Reactive-ion-etching (RIE) is a plasma process to etch substrate in low-pressure, commonly used in the micro fabrication procedures. It is a synergistic process between ion bombardment and chemically active etching. RIE enables the etching to be in a strictly vertical direction while minimizes the horizontal etching in order to get a sharp and clean edge of the structure.

RIE is used for the patterning of graphene into ribbons. The etching chamber is first evacuated to low pressure and maintained. O_2, the reactive gas, enters the chamber with the flow rate at 40 sccm. After EBL and development, graphene needs to be etched is covered with PMMA-495K (thickness ~ 500 nm). The sample should be etched to remove graphene which were only covered with PMMA-495K, while graphene covered with PMMA-495K and negative resist (maN-2403) still remains. But the etching time should not be too long, otherwise, graphene ribbons covered with PMMA and maN-2403 will also be etched by O_2 plasma. For WS_2 etching in *Chapter 4*, the etching recipe is the same as the one for graphene.

3.3.4 Metal Deposition

The metal deposition method I used for my work is thermal evaporation. After EBL patterning, the samples are stuck to a sample holder, facing the metal sources. When the pressure of the chamber reaches the specified value, we manually increase the current passing through the metal source, until the metal starts to gradually evaporate and reach the samples. As for the metal electrodes, 10 nm Cr and 80 nm Au are usually deposited. After the deposition, the samples are left in acetone at 50 ℃ for overnight to remove the unwanted metal films on PMMA photoresist.

3.4 Materials Characterization

3.4.1 Optical Microscopy

Optical microscopy is a simple, rapid and nondestructive way to determine the location and number of layers of 2D materials on substrates, over large area. This technique relies on the contrast between the 2D materials and the substrates. Thus it is important to choose the right substrate for optical microscopy characterization. The substrates I use for all my projects are SiO_2 (300nm)/Si which provide strong contrast for 2D materials, such graphene, WS_2 and MoS_2 under optical microscope. The thickness of 2D materials is also reflected on different contrasts to the substrates.

The optical microscope I used for my study in *Chapter 4* is a homemade optical stage, and for studies in *Chapter 5* and *6*, NIKON LV100ND was used, of which the objective lens and light intensity are adjustable to acquire the best image of graphene film, WS_2, MoS_2 domains sitting on SiO_2 (300nm)/Si substrate.

3.4.2 Scanning Electron Microscopy (SEM)

Scanning electron microscopy (SEM) is used to study the surface topography and the composition of samples. A beam of electrons, thermionically emitted from an electron gun, scans in a raster scan pattern on the samples and interacts with the atoms of samples with the interaction depth ranging from less than 100 nm to around 5 μm into sample's surface. Electrons with different energies are collected, such as the secondary electrons (SE), back scattered electrons (BSE) and X-ray. SE are electrons with low energies, generated from the inelastic scattering of the electrons by the specimen atoms within few nanometers depth. BSE are beam electrons emerge from deeper location of specimen (100 nm to 1 mm). The intensity of BSE is dependent on the atomic number, with heavy elements back-scattering electrons more strongly than the light ones. Thus BSE can reflect the chemical compositions of studied materials. For 2D materials, SE is mostly collected to form the image of the samples surface's topography, because of the thin nature of 2D materials.

A Hitachi S-4300 field emission SEM is used to characterize materials I used and the devices based on these materials in this thesis. A beam of electrons with energy of 3keV is used to observe the size of the crystals and the topography of materials on SiO_2 surface down to 40nm.

3.4.3 Raman and Photoluminescence (PL) Characterization

The lattice information of the materials can be studied via the peak positions of Raman spectrum. Usually a monochromatic laser interacts with molecular modes of a material, resulting in an inelastic scattering of the photons. Thus, a shift of the photon energy peak will be detected. From the shift of the energy, the vibrational, rotational and other modes of the material system can be deduced. PL is a process in which a molecule absorbs a photon and excite an electron to a higher energy level, which then recombine with a hole, radiating a photon. According to the PL intensity and peak position, the optical energy band of a material can be

detected. The Horiba LabRAM ARAM imaging confocal Raman spectrometer was used for both Raman and PL characterization of WS_2 and MoS_2 in my studies. Laser with wavelengths of 532nm and 633nm are integrated with this equipment for optical characterization use. For Raman mode, the wave frequency detected is usually from 200cm^{-1} to 600 cm^{-1} for WS_2 and MoS_2, and 1200cm^{-1} to 3000cm^{-1} for graphene with the resolution 1800 slits per mm grating. While for PL detection, the wavelength is from 500nm to 800nm for the monolayer TMDs and the resolution is 600 slits per mm grating. Both Raman and PL mapping were used to investigate the uniformity and the number of layers of the materials in my studies.

3.4.4 Atomic Force Microscopy (AFM) and Kelvin Probe Microscopy (KPM)

AFM is a scanning microscopy with resolution down to nanometer. The key component is a sensitive cantilever with a sharp probe at the top to scan the specimen surface. The force between the sample and the tip causes the defection of the cantilever, which can be detected by a beam of laser reflected off the back of the cantilever. As the distance between the tip and the sample surface changes, the force between them changes accordingly. This causes the cantilever to change in different degrees to maintain a constant force and the deflection of the cantilever is detected by the reflected laser beam. In 2D materials researches, AFM is considered to be a powerful technique to examine the surface roughness and the thickness of samples. AFM can be operated under three different working modes, depending on the sample conditions: contact, non-contact and tapping modes.

In the contact working mode, the tip is always in contact with the sample surface, maintaining a repulsive force in the range between 10^{-10} to 10^{-6} N. This working mode is not suitable for specimen with soft surface. Non-contact mode is the tip scanning on the sample surface with a distance at 5-10 nm. This mode does not bring damage to sample, thus is very suitable for soft surfaces. Tapping mode, which is also called dynamic contact mode, is the most popular mode for measurement under ambient condition. The cantilever oscillates above

the sample surface near its resonance frequency and taps on the surface periodically. The oscillation amplitude decreases when the tip gets closer the sample surface. Thus by detecting the change of the amplitude, the surface roughness can be acquired.

Asylum Research MFP-3D AFM was used for the WS_2 GBs study on SiO_2/Si substrate under the tapping-mode. (The AFM in *Chapter 4* was performed by Ghazi Syed Sarwat)

KPM measures the contact potential difference (CPD) between the probe tip and the sample. A two-pass technique is used for the potential measurement. In the first pass, the topography is measured in the tapping mode. In the second pass, a voltage is applied to the tip $V_{tip.}$ At the same time, the topography is retraced at a fixed height to the surface for the potential detection. The surface potential of the sample can be calculated from the equation: $CPD = (\phi_{tip} - \phi_{sample})/e$, where ϕ_{tip} and ϕ_{sample} are the potential of the probe tip and the sample surface, respectively. (The KPM in *Chapter 4* was performed by Ghazi Syed Sarwat)

3.5 Device Electrical Measurement

Electrical and opto-electrical measurements in chapters 4, 5 and 6 are conducted on a home-built probe station. The stage can be adjusted in X,Y and Z directions with a digital controller. Two tungsten probes (Signatone SE-T) were used to connect the source and drain electrodes of the devices to the source meter. The gate voltage was applied through the p doped silicon substrate from the back side with the silver paste. Two Keithley 2400 source meters were used for biasing and gating the photodetectors. The current resolution of the Keithley can reach 1nA, which is enough for most of our electrical and opto-electrical measurements. A 532nm laser beam was generated from a diode-pumped-solid-state laser (Thorlabs, DJ532-40) and reflected by a dichroic mirror to be focused by objective lens with either 50x or 10x magnification and further illuminated on the sample. The laser intensity can be controlled with

a current controller at it working temperature at 24.85℃. The intensity was measured with a power meter every time after experiment.

Chapter 4 Grain Boundaries Mediated Charge Transport in Monolayer WS_2

4.1 Introduction

The top-down approaches for 2D materials synthesis can produce residue free surface, but the lack of uniformity in thickness and size limitation hinder the viability of this method. Meanwhile, chemical vapour deposition method is widely adopted for scalable 2D materials synthesis. With this method, GBs are inevitably induced between randomly distributed domains. The structures and electronic properties of GBs of TMD materials have been studied with TEM and DFT calculation.(*128*) From these studies, it is predicted that GBs can be utilized to tune the electrical properties of TMD materials. However, the studies of the effect caused by GBs on the carrier transport of TMD materials-based field-effect transistors are rare.

Here, we grow high quality and uniform monolayer WS_2 with average size up to 100 μm and examine the carrier transport properties of field-effect transistors based on CVD synthesized monolayer WS_2, with GBs both parallel and perpendicular to the conductive channel, under vacuum condition and at room temperature. We observe that the GBs can act as a more n-doped conductive channel compared with pristine WS_2. This is understood to cause a negative shift in the threshold voltage.

4.2 Results and Discussions

4.2.1 Optical Characterization of WS_2 with GBs

The WS_2 domains and films we studied were synthesized by two furnaces CVD method.(*129*) With this method, uniform WS_2 domains with large scale and high density can be grown on SiO_2 (300nm)/Si substrate. By optimizing the optical contrast, some GBs formed between monolayer WS_2 domains are visible under optical microscope while some are invisible. As shown **Figure 4.1**a, truncated WS_2 domains with average size up to 100 μm are scattered on the substrate with uniform thickness. **Figure 4.1**b is the SEM image of triangle WS_2 monolayer domains. Two of the GBs with darker color are very easy to locate, which are marked with red arrows. The different shapes of WS_2 in **Figure 4.1**a and b are due to the different growth parameters in different locations on the SiO_2/Si substrate.(*130*) By analyzing the direction of the visible GBs relative to the WS_2 domain orientation, we found that these GBs prone to start along the bisector of the angle between two WS_2 domains regardless the domain relative orientation, as illustrated in **Figure 4.1**b. The mirror property of visible GBs is similar to the invisible ones reported.(*131*) With the elongating the visible-GBs from the edge to the inner side, the GBs bend to different directions to fit the orientation and center separation distance of the WS_2 domains, as shown in **Figure 4.1**c-e. Without specific mention, the GBs we talk about below are visible GBs.

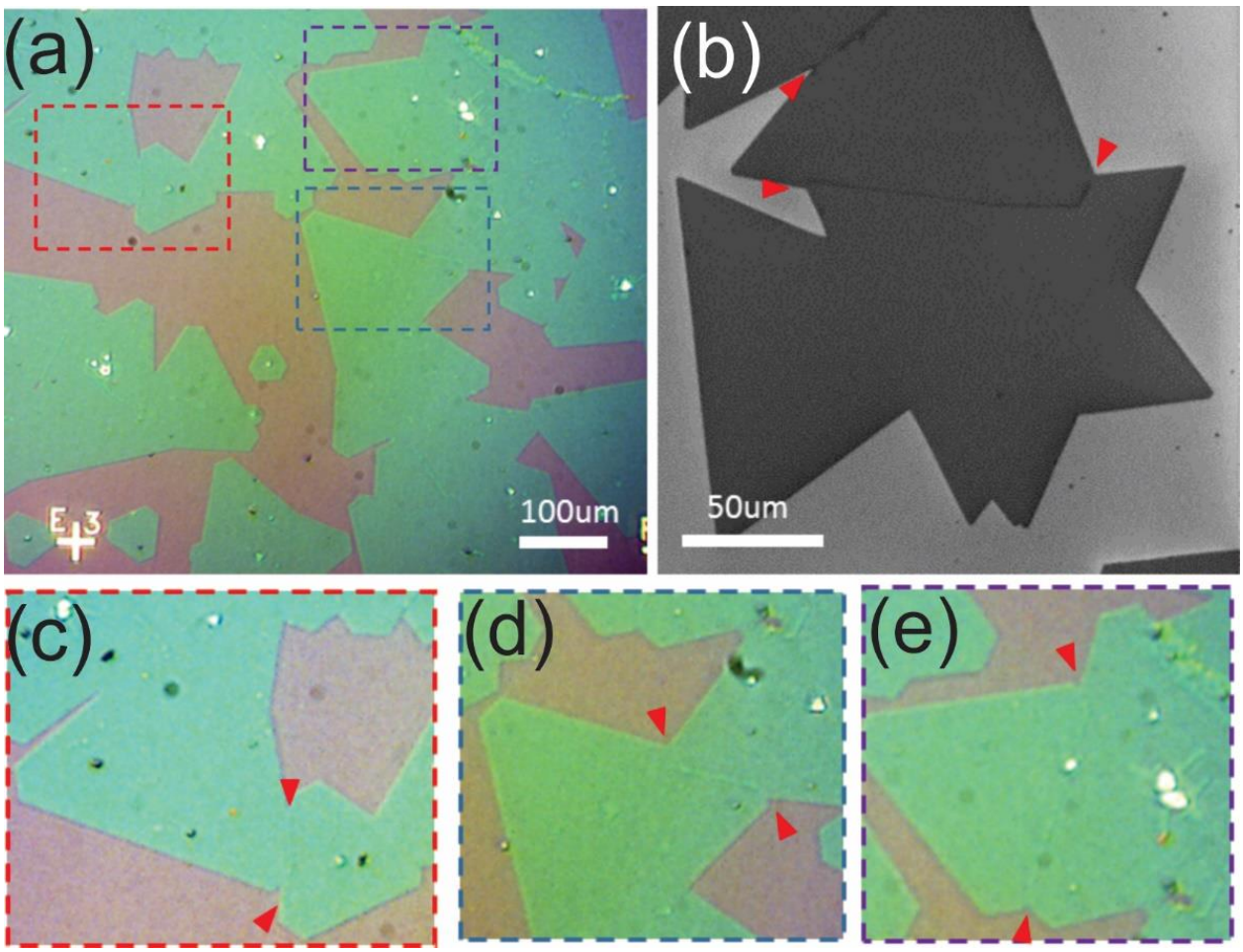

Figure 4.1. Visible GBs observed in the CVD synthesized monolayer WS_2 (a) Optical image of monolayer WS_2 domains on SiO_2/Si substrate. (b) SEM image of monolayer WS_2 domains merging to form visible GBs. The dark lines pointed with red arrows are visible GBs. (c-e) Optical images of WS_2 GBs with different configurations of conjunctive domains with different angles. The red arrows pointed to the GBs.

The optical properties of a visible GB formed by two WS_2 domains with 19.5° angle is studied by photoluminescence and Raman spectroscope. **Figure 4.2**a is the Raman spectrum of the pristine WS_2. **Figure 4.2**b is the optical image showing that two WS_2 domains merge together to form a GB. Based on the GB, multiple field effect transistors were designed to study the influence of the GB on the electrical properties of WS_2 monolayer. Based on the relative orientation of the conducting channel to that of the GB, the devices have three typical configurations: across the GB (perpendicular,$GB_{\perp}$), along the GB (parallel, $GB_{//}$) and without GB (pristine). CVD synthesized WS_2 was first transferred onto SiO_2 (300nm)/Si substrate with

the assistance of PMMA on top. Electron-beam lithography and oxygen plasma were used to pattern and etch the WS_2 into ribbons along GBs with 10μm width. Cr(20nm)/Au(80nm) was subsequently deposited onto the patterned WS_2 ribbon as electrodes with channel length as 10μm using thermal evaporation method. **Figure 4.2**c is the SEM image of our as fabricated devices with the three structures. In the SEM image, a blooming white line denoted by the red arrows is the GB. To examine the optical property of the GB in our device, photoluminescence mapping of the WS_2 was conducted on the device, which is shown in **Figure 4.2**d. There is a strong PL quenching along the GB as indicated in the PL mapping image and the integrated intensity quenched to 1/3 of that from the monolayer WS_2 a few micrometers away from the GB, shown in the **Figure 4.2**e. Using Lorentzian fitting, the PL spectra at GB and pristine WS_2 can be fitted well with two distinct peaks, corresponding to exciton (X) and negative trion (X^-), respectively, as shown in **Figure 4.2**f. For the pristine WS_2, exciton and trion peaks are located at around 2.00eV and 1.975eV, respectively. The high trion peak intensity indicates the n-doping of the CVD WS_2 domain sitting on SiO_2. The increase in the intensity ratio of X^-/X from 4.5 to 8 at GB suggests a slightly higher n-doping at the GB region, which is likely from the sulfur deficiency. S deficiency induces n-doping in WS_2 by introducing unpaired electrons into the lattice (*132, 167*). Strain at GBs can also induce additional doping (*133*), but it is always accompanied with a shift in the binding energy of the trion and exciton (due to change in the bandgap). In our experiments, both the trion and exciton peaks at the GBs are similar to those peaks in the bulk of the material, which indicates that the n-doping effect is most likely induced by the sulfur vacancies.

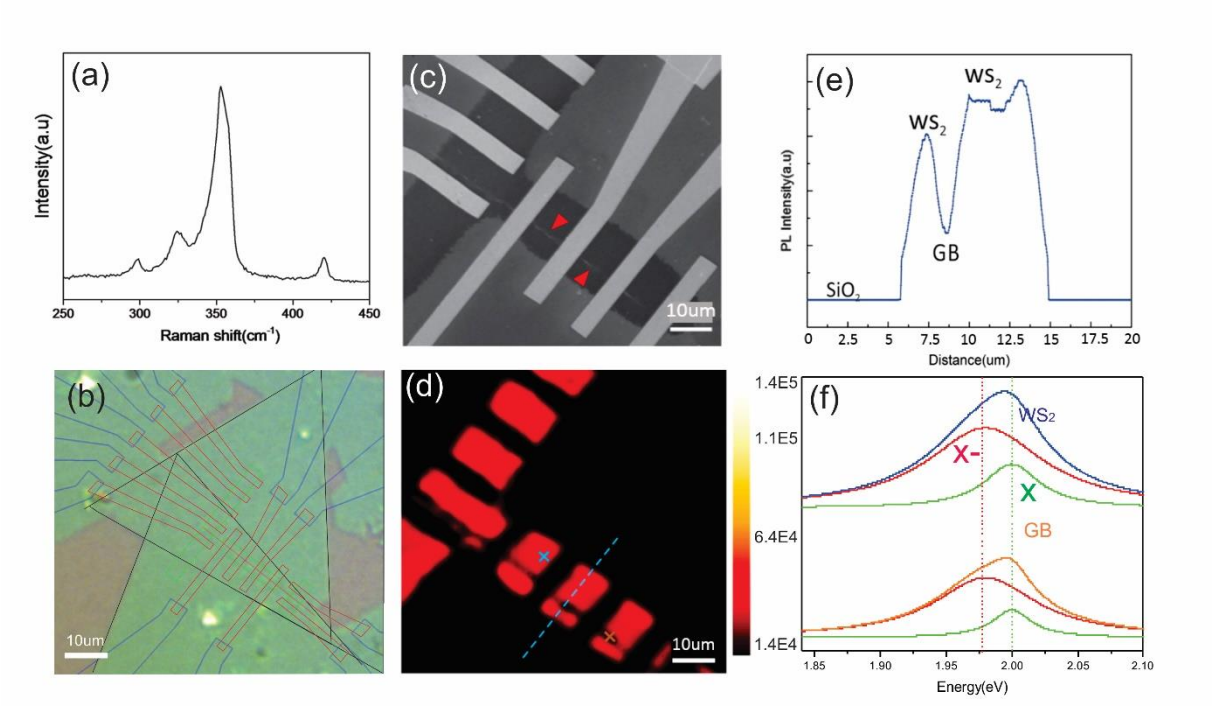

Figure 4.2. (a) Raman characterization of monolayer WS_2 away from GB. (b) The optical image showing two monolayer WS_2 domains merging together to form GB. The black triangles represent the outline of two WS_2 domains. The red and blue outlines are the designed electrodes for device fabrication around the GB. (c) SEM image of the WS_2 devices based on the design shown in (b). (d) PL mapping spectrum of the WS_2 GB by integrating the photo emission intensities from energy of 1.85eV to 2.10eV. (e) PL integrated intensity line profile corresponding to the line marked in (d) showing obvious PL quenching along the GB. (f) Lorentzian fitting of the PL spectra of both monolayer WS_2 and GB.

4.2.2 Electrical Characterization of WS_2 with GBs

I_{sd}-V_{sd} measurements are carried on the three sets of devices. Electrical properties of WS_2 are very sensitive to H_2, O_2 and H_2O adsorbed on the surface,(*134*, *135*) so before the electrical measurements, the devices were kept in a vacuum chamber for around 4 hours with a low pressure of 3×10^{-8} bar to remove all the molecules absorbed on the WS_2 surface. Joule heating annealing was also conducted to improve the metal contacts. All the electrical measurements were performed under vacuum condition (3×10^{-8} bar), at room temperature and in the dark environment. **Figure 4.3**a-c show the plots of the I_{ds} from multiple devices along a specific GB with V_{ds} within 0~1V under various V_g. The results in figure 4.3a and c show

that the devices with GBs in the channel are still conductive. The I_{sd}-V_{sd} plots show a nonlinear behavior indicating Schottky contacts formed at the interface of metal and WS_2. The I_{sd}-V_{sd} can be well modulated by the V_g. When increase V_g from -4V to 16V, I_{sd} of all three sets increases monotonously. The gate dependent measurements reveal that the devices with GBs in the channel can still be tuned effectively by the back-gate voltage regardless of the relative orientation of the GBs to the channel direction. The current of the WS_2+$GB_{//}$ devices (the conductive channel is parallel to the GB) has been doubled compared with devices with pristine WS_2 at high V_{ds}. This improvement indicates that GB is more conductive than pristine WS_2 and could be likely attributed to two effects: (1) reduced Schottky barrier height formed between metal contact and GB(*136*) and (2) n-doping effect at the GB, which has been observed from the PL spectrum.

In **Figure 4.3**d and e, we compared the transfer characteristics (I_{ds}-V_g) of the three sets of devices. The I_{ds}-V_g plots show the n-type behavior for all of the three devices with different conducting channels. It is worth noting that the existence and the orientation of the GBs exhibit influence on the value of the threshold voltages (V_{th}) under vacuum condition. The V_{th} here is extrapolated in the linear region of the transfer characteristic curve.(*137*) For the devices based on pristine WS_2, the average V_{th} is measured to be 11V. The insertion of a GB parallel to the channel obviously reduced the V_{th} by 7V, to around 4V, while for devices with GB perpendicular (WS_2+$GB_{\perp}$) to the conducting direction, the average V_{th} is measured to be 17V, as shown in **Figure 4.3**f. The negative shift of V_{th} for WS_2+$GB_{//}$ device indicates that the GB acts as a conductive channel parallel to the WS_2 in the parallel structured device.

The decreased threshold voltage in the WS_2+$GB_{//}$ devices indicate greater n-doping effect along the GB which reasons why such devices are turned ON before pristine WS_2 FET on application of V_g. The V_g induces shift in the Fermi level of the conductive channel relative to the energy bands. For the GB, which are more n-doped, the energy difference between the

Fermi level and the conduction band edge is smaller compared with that in the pristine WS_2 region. That is why the magnitude of the gate voltage needed to switch on the conduction along the GB is smaller. Using the formula: $n = \varepsilon_0 \varepsilon_r \Delta V_T / te$, we can estimate the charge carrier density induced by the GB. Where $\varepsilon_0, \varepsilon_r$ are the dielectric constants of free space ($8.85 \times 10^{-12} F/m$) and SiO_2(3.9) respectively; ΔV_T is the average difference of the threshold voltage between the pristine WS_2 device and the WS_2+$GB_{//}$ devices; t is the thickness of SiO_2 dielectric layer (300nm); e is the electron charge ($1.6 \times 10^{-19} C$). The charge carrier density induced by the GB is calculated to be 5×10^{11} cm^{-2} on average. As to the reasons for the increase of the threshold voltage of the WS_2+$GB_{\perp}$ devices, I am still not quite sure about them.

The logarithmic scale of I_{ds}-V_g curves are shown in the **Figure 4.3**e. It can be seen that all sets of devices show comparable on/off ratio, around 10^3, with off-current as low as 0.1nA. The subthreshold swing (SS), an important parameter to describe the switch on speed of a field-effect transistor, is defined as the V_g needed to increase the source-drain current for one decade in the subthreshold region The subthreshold voltages are calculated to be 1.8V/dec and 1.7V/dec for pristine WS_2 based devices and WS_2+$GB_{\perp}$ devices, respectively. While for the WS_2+$GB_{//}$ devices, the value increased to as twice as that for WS_2 based devices (3.99V/dec). The subthreshold transport is dominated by the carrier diffusion in the channel. The increase of the subthreshold swing can be understood as a result of the increase of the charge scatter centers from both GB and the interface when devices conduct along GBs.

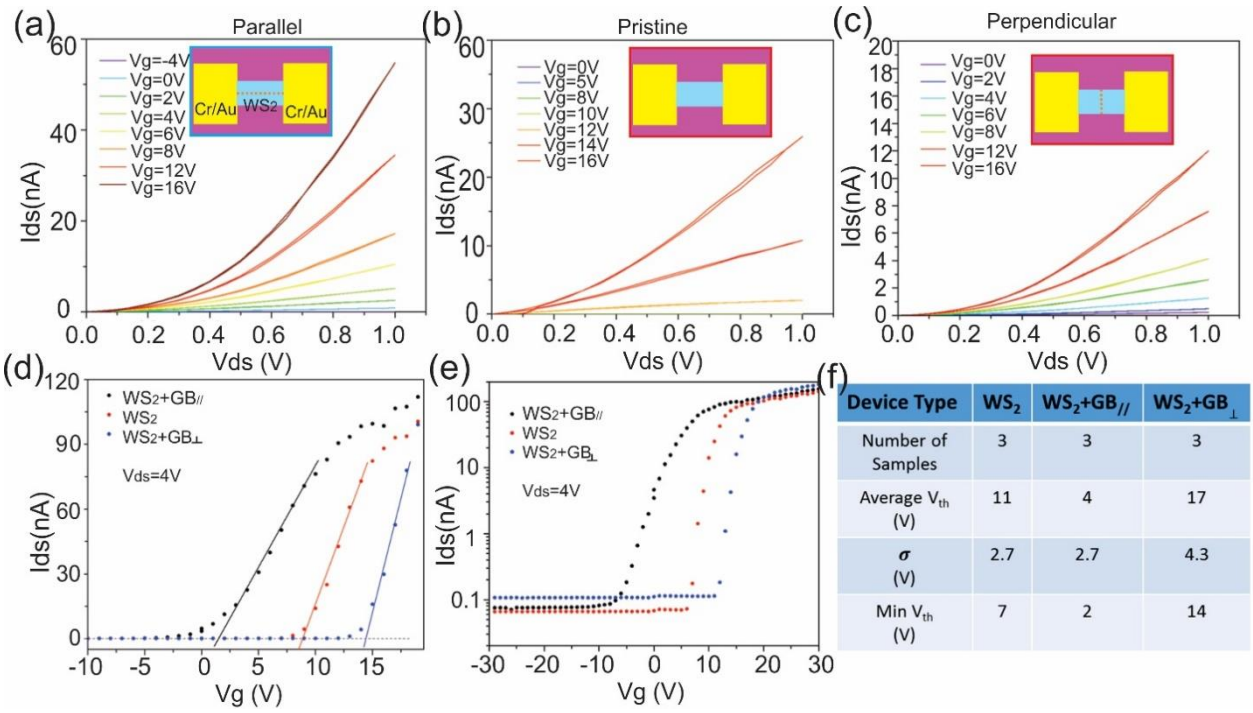

Device Type	WS_2	WS_2+$GB_{//}$	WS_2+$GB_{\perp}$
Number of Samples	3	3	3
Average V_{th} (V)	11	4	17
σ (V)	2.7	2.7	4.3
Min V_{th} (V)	7	2	14

Figure 4.3. Electrical characterization of devices with conductive channels parallel to GBs, with pristine WS_2 and perpendicular to the GBs in dark and vacuum condition. (a-c) Plots of the I_{ds}-V_{ds} curves of devices of three different structures under various gate voltages during the forward sweep. (d)Transfer curves of devices of three structures with bias voltage at 4V. (e) Semilogarithmic plots of the curves in (d). (f) Comparison of the threshold voltage (V_{th}) of devices with three different structures. 3 devices of each structure are measured. The average, variance and minimum V_{th} are presented in the table.

4.2.3 AFM and KPM Characterization of the WS_2 with GBs

The n-doping effect at the GBs is further confirmed by measuring the surface potential at the GB with the Kelvin probe microscope (KPM). In the KPM measurement, a cantilever is used as a reference electrode. The contact potential difference (CPD) between the tip and materials is measured to acquire the work function of the materials. **Figure 4.4**a is the atomic force microscopy (AFM) mapping of monolayer WS_2 with a GB. It is very clear to see the S-shape of the GB. Clusters with height at around 10nm accumulate at the GB, which is likely due to the energetically preference. Further experiments are needed to figure out the composition of the clusters. The KPM mapping of WS_2 with GB is shown in **Figure 4.4**b. The inset of **Figure 4.4**b shows the CPD of the tip and WS_2 along the dashed line across the GB.

The relationship between CPD and the potential energy of WS_2 can be expressed as: $CPD_{WS2} = (\phi_{tip} - \phi_{WS2})/e$, where ϕ_{tip} is the work function of the tip, ϕ_{WS2} is the work function of WS_2, e is the elementary charge. The CPD along the GB is much smaller than that of pristine WS_2, as shown in **Figure 4.4**b. In **Figure 4.4**c, the energy band diagram of monolayer WS_2, GB relative to the KMP tip energy are presented. It is found that the work function at the GB is smaller than that of pristine WS_2, which translates into a higher fermi level at GB before band bending. **Figure 4.4**d shows that at the equilibrium state, GB is more n-doped that the pristine WS_2.

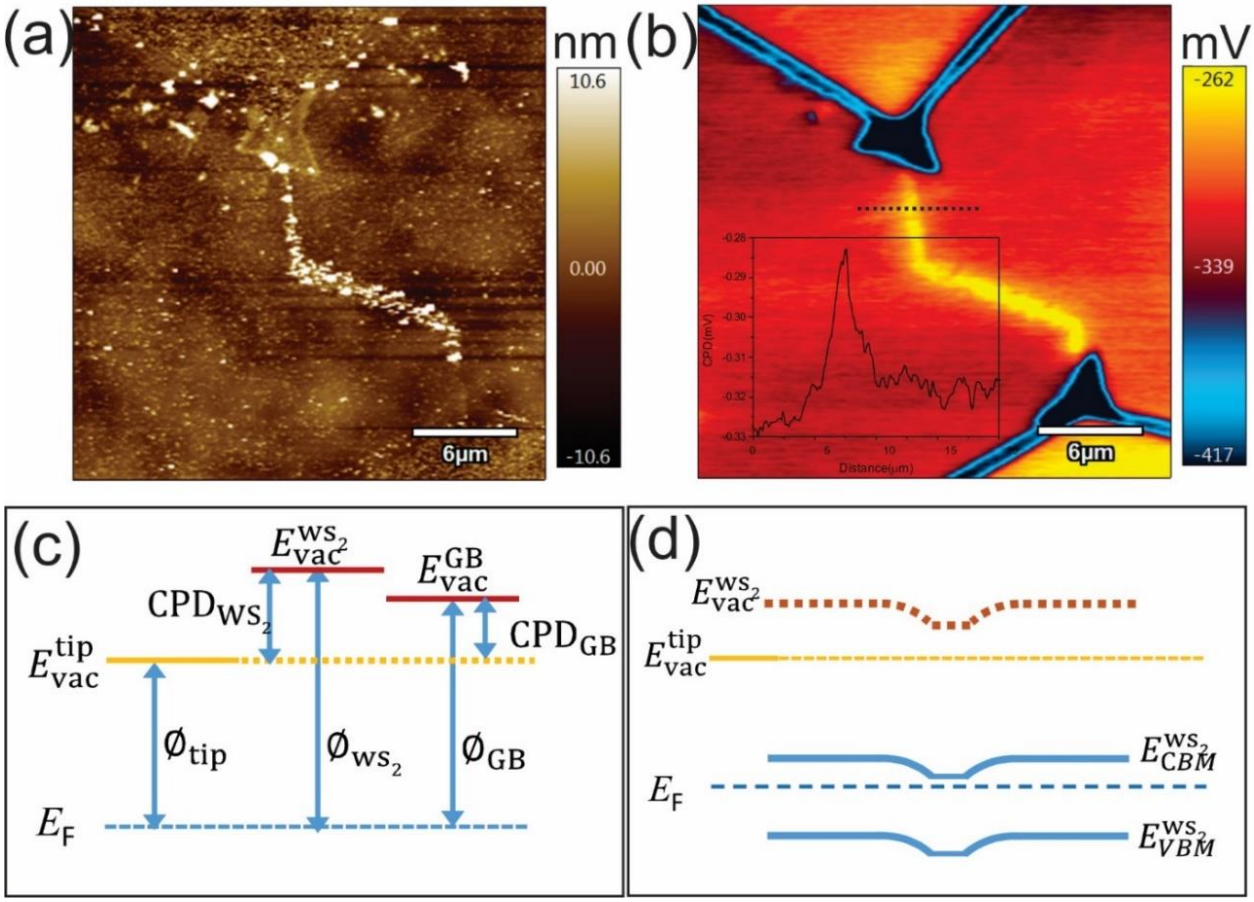

Figure 4.4. AFM and KPM characterization and energy band diagram. (a) AFM and (b) KPM mapping of WS_2 with a GB. Inset of (b) is the line profile of KPM result along the dashed line across the GB. (c) Schematic of the energy band diagrams of pristine WS_2 and at GB, relative to the KPM tip under equilibrium condition. The yellow solid and dashed lines represent the vacuum level of KPM tip. The red solid lines represent the vacuum level of pristine WS_2 and at

GB. The blue dashed line is the fermi level. (d) The energy band diagram with conduction and valance band to show the band bending around the GB.

4.3 Conclusion

In summary, we realized the fabrication of field-effect transistors based on CVD synthesized pristine monolayer WS_2, parallel to GB and perpendicular to GB. The transport properties of the three types of field-effect transistors were studied under vacuum condition and at room temperature. The GB can act as a more n-doped conductive channel compared with pristine WS_2, shifting the threshold voltage of the devices to the negative direction, which was further confirmed with the PL and KPM characterization. Our finding reveals the importance of controlling the formation of GBs during the CVD synthesis for the device application.

4.4 Contribution Statement

Syed Ghazi Sarwat did the AFM and KPM measurements in this project. Dr. Ye Fan and Haijie Tan provided training in device fabrication and established the software interface for electrical characterization. Dr. Youming Rong provided me with some WS_2 and offered some discussions.

Chapter 5 Utilizing Interlayer Excitons in Bilayer WS_2 for Increased Photovoltaic Response in Ultrathin Graphene Vertical Cross-Bar Photodetecting Tunneling Transistors

5.1 Introduction

As we have mentioned above, vdWHs based on WS_2 can serve as photodetectors and photovoltaic devices, because WS_2 offers high absorption within the visible range and also owns thickness tunable bandgap.

Up until now, most all-2D vertical stacked heterostructure devices explored for photodetector applications have been based on mechanical exfoliated 2D crystals, which severely limits production yield and device fabrication scalability. The small batch number of devices made with mechanically exfoliated 2D materials makes it difficult to obtain statistically robust results, given variances in device to device behaviors. Moreover, it is challenging to control the number of layers of TMD crystals isolated by mechanical exfoliation with most regions having mixtures of both mono- and bi-layers. The rise of high quality CVD grown 2D TMDs and graphene offers a possible route to explore the wafer scale fabrication of all-2D opto-electronic devices and the assessment of their performance, which is essential for the industrial realization of 2D technology. Here, Gr/WS_2/Gr based ultrathin photodetectors

fabricated entirely using CVD grown materials are demonstrated. In particular I utilize vertically stacked cross-bar graphene electrodes to enable large numbers of devices to be fabricated with minimal alignment steps. I systematically study the properties of such devices with monolayer and bilayer WS_2 sandwiched between graphene electrodes as photodetectors and reveal strong photovoltaic response in bilayer WS_2, which is observed to be one order of magnitude higher than in monolayer WS_2 device.

5.2 Results and Discussion

5.2.1 Fabrication of Gr/WS_2/Gr Vertical Device

The fabrication process for the Gr/WS_2/Gr vertical heterostructure devices is schematically illustrated in **Figure 5.1**a. In brief, the monolayer graphene film was first synthesized by the chemical vapour deposition method and then transferred onto a silicon wafer covered with 300 nm SiO_2. The graphene film was then patterned with EBL and etched into strips of 20 μm width by oxygen plasma to form the bottom graphene electrode (Step 1, **Figure 5.1**a). A layer of CVD grown WS_2 domains was then transferred onto the graphene strips as the photo-absorbing semiconductor material (Step 2, **Figure 5.1**a). The high domain density ensures that a large number of devices are created. This approach is not aimed at producing uniform 2D arrays of devices, but instead enough devices to obtain a statistically robust analysis. Another layer of pre-patterned monolayer graphene strips was subsequently transferred on top of the substrate/Gr/WS_2 as the top electrode with a perpendicular alignment to the bottom graphene strips (Step 3, **Figure 5.1**a). Finally, bond pads (Cr/Au (10 nm/80 nm)) were patterned using EBL and thermally evaporated on the graphene electrodes (Step 4, **Figure 5.1**a). In the center of **Figure 5.1**a is the 3D schematic illustration showing the typical device geometry with graphene top and bottom cross bar electrodes and WS_2 sandwiched in between. Here, we only studied the vertical devices with top and bottom graphene completely separated by WS_2

domains. As shown in the SEM image (see **Figure 5.1**b) our CVD synthesized WS_2 are mainly isolated domains evenly distributed across the 1 cm×1 cm substrate. The WS_2 crystals consist of both monolayer and bilayer domains, which enables the study of layer dependence on the device performance. The fabrication of vertical graphene cross bar electrode pairs was highly reproducible, with ~95% yield. The high density of WS_2 domains resulted in ~50% of graphene cross bar electrode pairs to be separated by WS_2 to form Gr/WS_2/Gr devices, with the majority of WS_2 crystals being monolayer (90%) and a few bilayer (10%). **Figure 5.1**c shows the SEM image of a typical Gr/WS_2/Gr device. The devices were then isolated from other devices by mechanical etching of the surrounding graphene strips using a nanotip probe to stop any leakage currents.

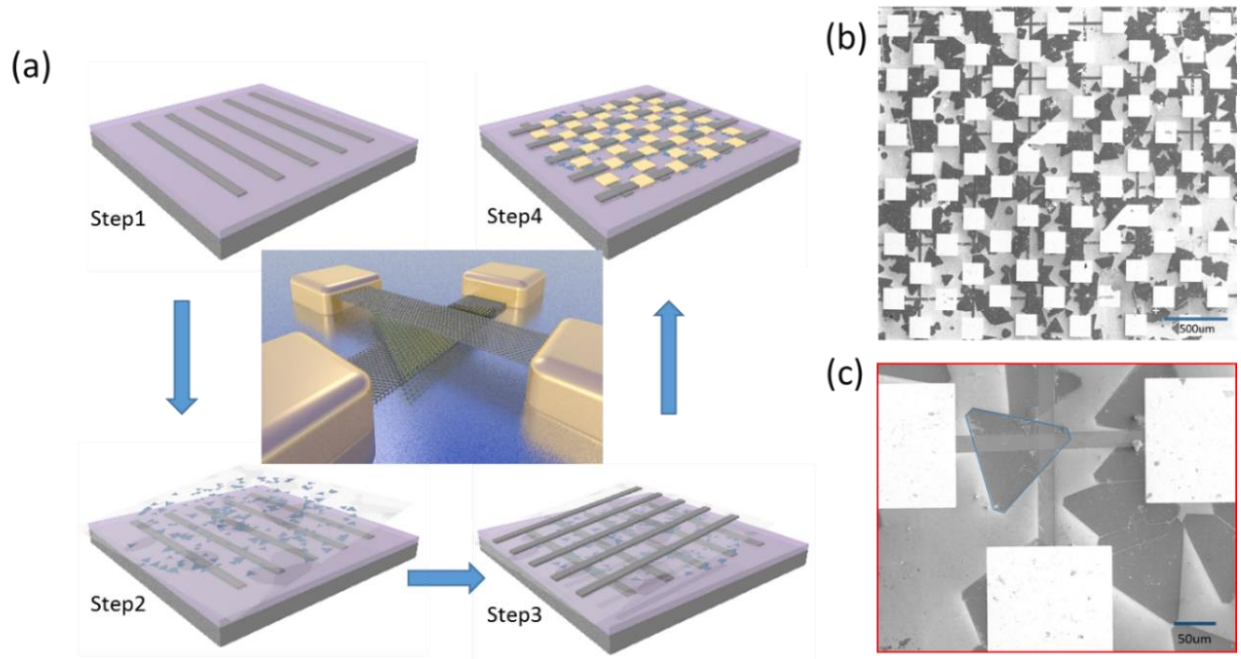

Figure 5.1. (a) Schematic illustration showing the fabrication steps (Step 1-Step 4) for creating the vertically stacked Gr/WS_2/Gr devices. Step 1: Graphene nanoribbon fabrication by electron beam lithography. Step 2: Transfer of WS_2 domains onto bottom graphene nanoribbons and removal of polymer. Step 3: Transfer of top graphene nanoribbon electrodes. Step 4: Deposition of Au bond pads to graphene nanoribbons at bottom and top. Each device is isolated from all others before measurement by cutting the connecting graphene electrodes using a sharp metal tip. (b) SEM image of the fabricated device array. (c) SEM image of one of the vertical devices in (b).

5.2.2 Raman and PL Characterization

Figure 5.2a is an optical microscope image of a typical device that comprises a monolayer WS_2 domain sandwiched between graphene electrodes (top graphene: Gr_T, and bottom graphene Gr_B), and a bilayer WS_2 beside the device. Although the CVD method adopted for the synthesis primarily yields monolayer WS_2 domains, several bilayer and multilayer domains also grow. By adjusting the RGB color channels of the imaging CCD, the monolayer and bilayer WS_2 domains are distinguished, based on the contrast between the optical images. Both the monolayer and bilayer WS_2 are further probed using Raman spectroscopy. **Figure 5.2**b is the Raman spectrum of graphene electrodes with excitation wavelength of 532 nm. It shows a 2D/G intensity ratio of around 1.5, indicating our CVD synthesized graphene is mostly monolayer.(*138*) The darker traces in the graphene ribbons in the optical image are bilayer graphene. The Raman spectra of monolayer and bilayer WS_2 are shown in **Figure 5.2**c. Fitting Lorentzian curves reveals the presence of multiple peaks in the Raman spectra of WS_2, $2LA$ (second-order longitudinal acoustic), $E^1_{2g}(\Gamma)$ (in-plane vibration mode) and $A_{1g}(\Gamma)$ (out-of-plane mode) (**Figure 5.2**c). The two main peaks $E^1_{2g}(\Gamma)$ and $A_{1g}(\Gamma)$ of monolayer WS_2 are positioned at 355.2 cm^{-1} and 417.5 cm^{-1}, respectively, similar to literature.(*139*) Also, the second-order $2LA$ band is more intense than the first-order $E^1_{2g}(\Gamma)$ and $A_{1g}(\Gamma)$ bands, due to the double-resonance process.(*75*, *140*) While for the bilayer WS_2, the $E^1_{2g}(\Gamma)$ peak was softened, positioning at 355.66 cm^{-1} and $A_{1g}(\Gamma)$ upshift to 419.49 cm^{-1}. Also, the peak intensity ratio of $2LA(M)/A_{1g}(\Gamma)$ decreases from 7.6 to 5.9 as layer number increases from monolayer to bilayer. Because the Raman spectra of WS_2 can be influenced by several factors, such as strain, doping, number of layers, one cannot use the absolute Raman peak positions and intensities with certainty to determine the number of layers. Instead, a good practice, which we use here is combining the contrast in the optical images with the relative Raman peak positions and intensities to differentiate monolayers from bilayers.

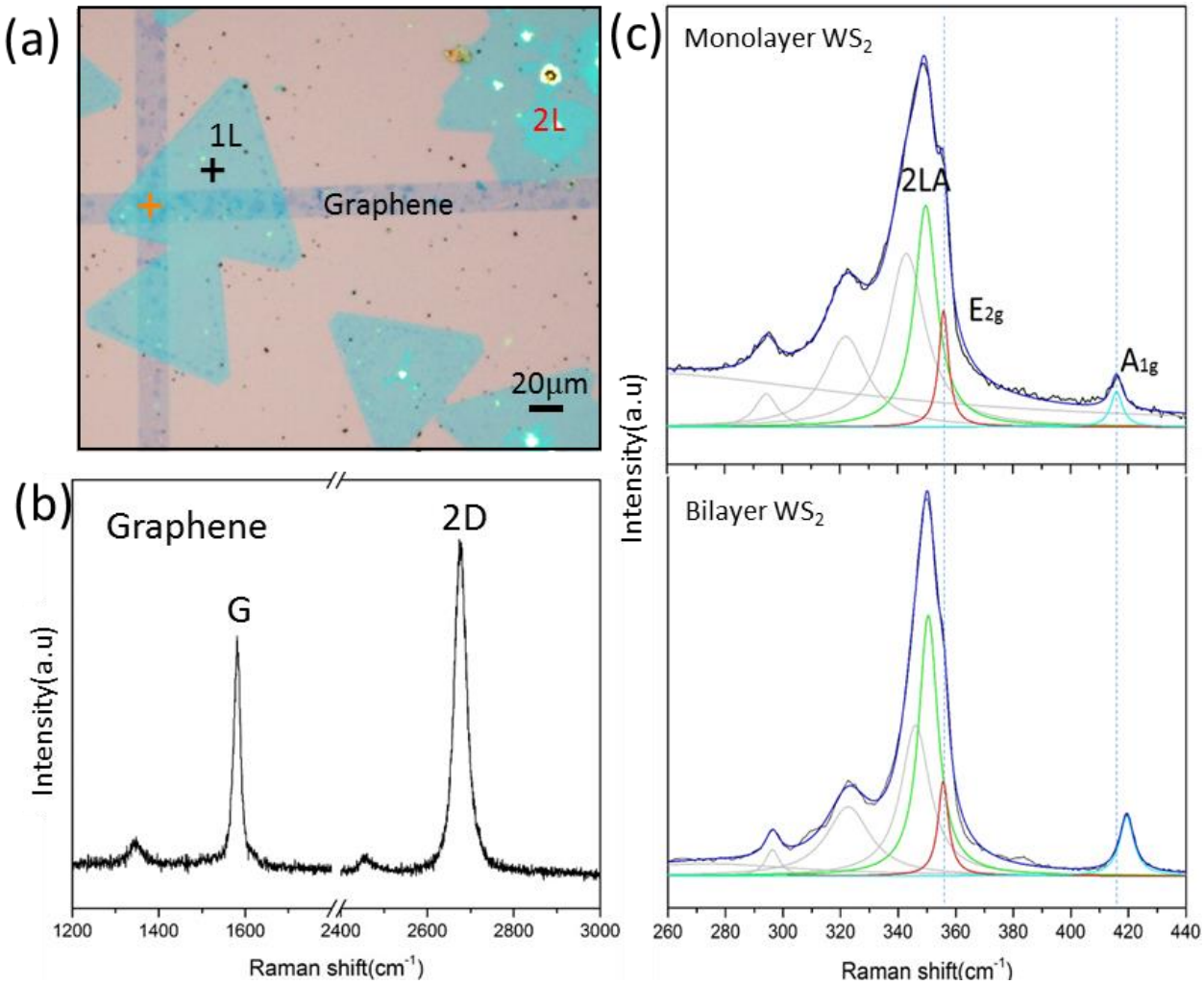

Figure 5.2. Optical characterization of Gr/WS_2(1L)/Gr heterostructure. (a) Optical microscope image of a Gr/WS_2(1L)/Gr device. Monolayer WS_2, bilayer WS_2 and graphene are shown in the image. (b) Raman spectrum of graphene (c) Raman spectra of monolayer and bilayer WS_2 excited with 532 nm wavelength laser. The two main peaks which reflect the properties of WS_2 are fitted using Lorentzian function.

PL spectra of monolayer and bilayer WS_2 on SiO_2/Si substrate are conducted to further determine the number of layers of WS_2, as shown in **Figure 5.3**a. Bilayer WS_2 shows a significant PL quenching compared with monolayer WS_2. **Figure 5.3**b is the PL intensity comparison of monolayer WS_2 in two different regions, with the black curve representing the WS_2 on the SiO_2 surface, and the orange one from the WS_2 sandwiched between two graphene electrodes. The PL intensity from WS_2 is heavily quenched when in contact with graphene. The deconstruction of the PL spectra of WS_2 into negative trion (X^-) and exciton (X) peaks using

Lorentz fitting are shown in **Figure 5.3**c and d. For the WS_2 on the SiO_2 surface, the integrated PL intensity ratio of X^-/X is 1.7 (**Figure 5.3**c). Stacking the WS_2 with graphene, the X^-/X ratio decreases to 0.6, indicating the depletion of electrons in WS_2 (**Figure 5.3**d). This is due to electron transferring from WS_2 to graphene (top and bottom layers) within the Gr/WS_2/Gr stacks.(*99*) The quenching of the PL in the stacked region is an indication of strong interactions between graphene and WS_2 layers.(*99*, *141*)

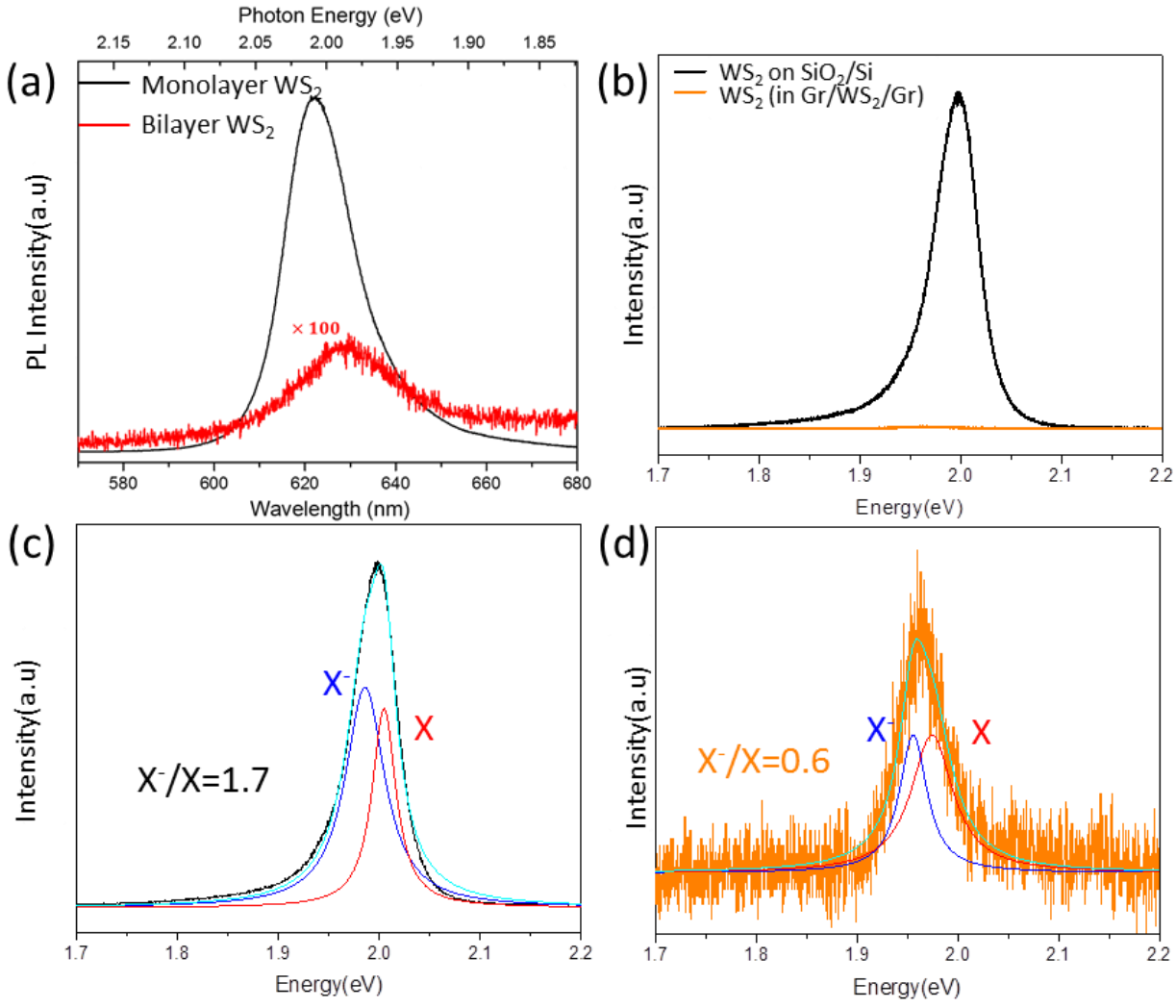

Figure 5.3. (a) The PL signals of monolayer and bilayer WS_2 domains on SiO_2. The bilayer WS_2 PL signal was magnified by 100 times. (b) PL spectra from monolayer WS_2 domain on SiO_2 and sandwiched between graphene top and bottom electrodes. (c) and (d) are PL spectra of WS_2 on SiO_2/Si and sandwiched between graphene electrodes when exposed with 532 nm laser. Lorentz fitting of the two PL peaks is conducted. The blue and red peaks are the trion and exciton peaks, the green curves are the fitted PL peaks for excitons (X) and trions (X^-).

5.2.3. Doping Levels of Gr_B and Gr_T in the Gr/WS_2/Gr Junction

To analyze the doping levels of Gr_B and Gr_T by WS_2 in the Gr/WS_2/Gr devices, we performed gate sweep measurements on the graphene ribbons in the heterostructure devices under dark conditions. When graphene and WS_2 come in contact with each other, the Fermi level differences drives the electrons in WS_2 to diffusive to graphene. The holes left behind in WS_2 source positive gating effect, thereby n-doping graphene. So the metal-Gr_B(or Gr_T)-metal lateral field-effect transistor shown in **Figure 5.4**a (**5.4**b)can be modeled as two graphene resistors with different doping levels (different Dirac points) in series. (*99*, *142*) This model was adopted here to deduce the neutrality points (Dirac points) of both the top and bottom graphene. Because the transfer curve of the graphene transistor is the combination of two resistors: graphene on SiO_2 and graphene in contact with WS_2, its shape is determined by the relative area between the covered and uncovered regions. Eq. 5-1 was used for the fitting of our measurements in **Figure 5.4**.

$$R = R_c + \frac{A_1}{\sqrt{1+\frac{(V_g - V_{CNP})^2}{B_1^2}}} + \frac{A_2}{\sqrt{1+\frac{(V_g - V_{CNP})^2}{B_2^2}}} \qquad \text{(Eq.5-1)}$$

In this equation, R_c is the contact resistance, V_{CNP} is the charge neutrality point, V_g is the gate voltage, $A = \frac{\mathrm{L}}{\mathrm{w}\cdot\mathrm{e}\cdot n_0\cdot\mu}$, $B = \frac{\mathrm{e}\cdot n_0\cdot\mathrm{t}}{\varepsilon}$. Where n_0 is the residue charge carrier density, μ is the charge mobility, e is the elementary charge unit, L and w are the length and width of graphene ribbons, ε and t are the dielectric constant and thickness of SiO_2 in our devices. The neutrality points of both Gr_B and Gr_T contacted with WS_2 are fitted to be around 0 V and 22 V. We assume that Gr_T is more p-doped than Gr_B in the Gr/WS_2/Gr junction is because the strong hole doping effect of oxygen and moisture from air.(*143*)

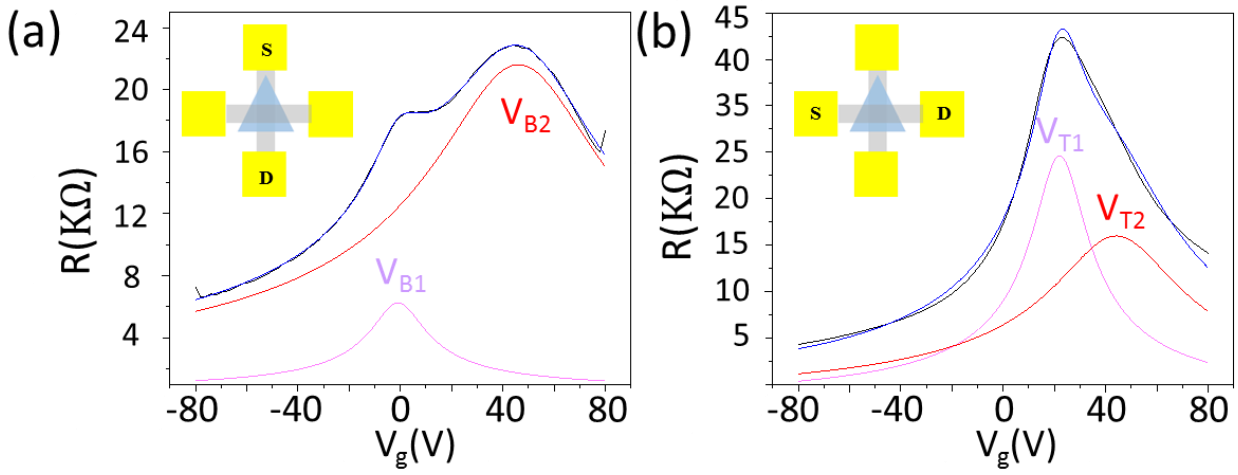

Figure 5.4. Gate sweep of (a) Gr_B and (b) Gr_T in one of our Gr/WS_2/Gr devices (black) and the fitting curves (dark blue) of the gate sweep results. The pink peaks (V_{B1},V_{T1}) and red peaks (V_{B2},V_{T2}) are the positions the charge neutrality points of graphene contacted with WS_2 and on SiO_2/Si. (The subscripts B and T represent bottom and top) Insets are the schematic diagram of the source-drain connection in the measurement process.

5.2.4 Electrical and Opto-electrical Measurement of Gr/WS_2(1L)/Gr Vertical Heterostructure

First, we measured the dark current from Gr/WS_2(1L)/Gr devices at room temperature. **Figure 5.5**a shows the current-voltage (I_{ds}-V_{ds}) data for a typical device with the applied bias voltage within the range of 0-1 V at different back gate voltages. The Gr/WS_2(1L)/Gr devices show linear I_{ds}-V_{ds} curves, which is typical for tunneling currents through monolayer WS_2.(*144*) The dependence of the photocurrent on the laser power is then studied at room temperature and in ambient condition. The bottom graphene is always grounded, and the source-drain bias is applied to the top graphene electrode in our study. **Figure 5.5**b shows the transfer curves of the Gr/WS_2(1L)/Gr photodetector upon exposure to 532 nm (2.3 eV) light with increasing power, with a source-drain bias voltage fixed at 0.5 V. The transfer curves show V-shape, very similar to that of pristine graphene on a SiO_2 substrate, suggesting that the carrier transport of our vertical devices is mainly dominated by the semi-metallic density of states of graphene in dark condition.(*145*) Without illumination, the device shows a charge neutral point (V_{CNP}) located

around 32 V. This neutral point is a convolution of Dirac points of four different graphene ribbons, namely top graphene on WS_2 (V_{T1}), top graphene on substrate (V_{T2}), bottom graphene between substrate and WS_2 (V_{B1}), bottom graphene on substrate (V_{B2}). We have shown in **Figure 5.4** that the Dirac points of top and bottom graphene sitting on substrate located at around 40V, while those in contact with WS_2 show Dirac points at smaller gate voltages. The device shows strong response to the incident light, with the increasing power gradually shifting the transfer curve towards the negative direction. The neutral point splits into two under increasing illumination power, with one (V_{CNP1}) shifting significantly towards the negative direction while the other (V_{CNP2}) shifting only a little when the light power increases. Prior work on WS_2 vertically stacked on graphene nanoribbon transistors showed similar Dirac points splitting when illuminated due to local changes in doping levels of graphene from charge transfer.(*99*) In our case, the transfer of photo-excited electrons in WS_2 to graphene is also the likely cause of the shift in Dirac position of graphene in contact with WS_2. Higher intensity optical exposure of the Gr/WS_2/Gr junction facilitates more electrons to transfer from WS_2 to graphene. Concomitantly, more holes are left in WS_2, which in turn more strongly gate the graphene. The photocurrent, shown in **Figure 5.5**c, was obtained by subtracting the dark current from the current when the vertical device is illuminated with light (Also see in **Figure A1**(a). The light green region is the photocurrent transition area, where the photocurrent reverses the sign. To be specific, when the V_g is at 20 V, the photocurrent is negative with small incident laser power and reverses the sign when the laser power reaches a higher value. This is reasonable as more photo-excited electrons transfer to graphene with higher incident laser power, which combine with the holes in graphene and the remaining electrons will contribute to the photocurrent. To evaluate the performance of our device, photoresponsivity and photo-gain are analyzed, which are important figures of merit to evaluate the performance of a photodetector. **Figure 5.5**d shows the photoresponsivities of this photodetector with respect to the illuminated laser power at two back gate voltages (V_g = 80 V, -80 V) when biased with 0.5V.

The photoresponsivity of the device decreases linearly with increasing the excitation laser power, which is attributed to be the photo absorption saturation in monolayer WS_2 sandwiched between graphene electrodes. Photogain is an important parameter for photodetectors. It can be expressed with the formula: $G = \frac{Rhv}{e \cdot \eta_{abs} \cdot \eta_{tra}}$, where R is the photoresponsivity, h is the plank constant, v is the frequency of the incident light, e is the elementary charge, η_{abs} is light absorption efficiency, η_{tra} is the charge transfer efficiency. If we optimistically assume that all the photogenerated charge carriers on the device are collected by the electrodes and contribute to the photocurrent, η_{tra} equals to 100%. The external photo-gains in our devices was calculated to be 10.8 and 8.4 for gate voltage at -80 V and 80 V. Considering the absorbance (η_{abs})of 532 nm light for monolayer WS_2 is around 8%,(*146*) the internal photo-gain we calculated can be as high as 136 and 106 for our device with gate voltage at -80 V and 80 V, with laser power of 0.1μW, as shown in **Figure 5.5**e.

We attribute the photocurrent in Gr/WS_2(1L)/Gr vertical devices mainly to be the separation and collection of photo-excited electrons and holes in WS_2. Photo-thermoelectric effects (PTEs) due to different thermoelectric power in graphene-based photodetectors has been explored,(*147*, *148*) but this effect is negligible in our devices due to the low excitation powers, which will be discussed in details when we study the Gr/WS_2(2L)/Gr vertical devices in the following part. Because of the van der Waals (vdW) gap between graphene and WS_2, tunneling potential barriers are formed in Gr_B/WS_2 and WS_2/Gr_T interfaces, we assume the barrier widths between Gr_B/WS_2 and WS_2/Gr_T are the same, but with different heights. By creating asymmetric tunneling barrier heights between Gr_B/WS_2 and WS_2/Gr_T by variable doping and local dielectric environments, the photo-excited electrons in WS_2 have different collecting rates by Gr_B and Gr_T. The difference in electron collecting rates results in an overall photocurrent. Tunneling barrier height can be modulated by external applied bias and the doping levels of G_B and G_T induced by the surrounding environment, as shown in **Figure 5.5**f. The photocurrent

results of Gr_B/WS_2 and WS_2/Gr_T confirm that the electrostatic potential barrier in the Gr_B/WS_2 interface is higher than that in the WS_2/Gr_T interface when there is no bias and gate voltage applied. The internal asymmetric potential barriers between Gr_B and Gr_T/WS_2 interfaces is similar to the results reported for Gr/MoS_2 interfaces. The energy of the excited electrons in WS_2 was calculated to be 3.7 eV below the vacuum energy, calculated with a simple mathematical formula in Eq. 5-2:

$$E_e = \Phi_{WS_2} + E_g - E_{laser} \qquad \text{(Eq.5-2)}$$

Where Φ_{WS_2} and E_g are the work function and the bandgap of monolayer WS_2. E_{laser} is the energy of the incident laser (wavelength is 532 nm). The energy of the excited electrons is located between the region confined by the top and bottom barriers. In this case, the photo-generated electrons can tunnel from WS_2 through the barrier into both Gr_B and Gr_T with different probabilities, with higher tunneling probability through the lower barrier at WS_2/Gr_T interface. The difference in the tunneling probabilities of the photo-excited electrons into Gr_T and Gr_B modulate the magnitude of photocurrent.

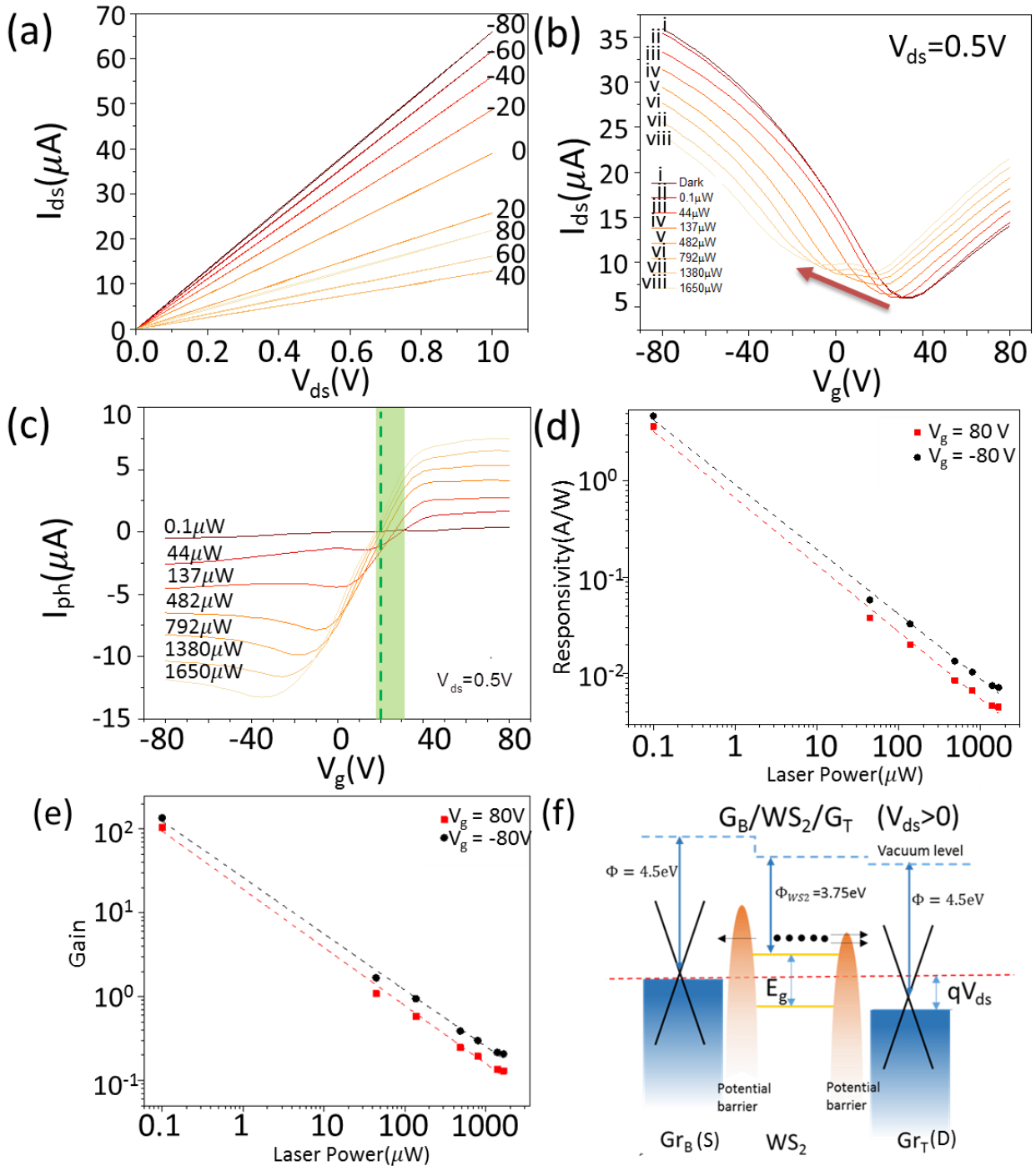

Figure 5.5. Photoresponse of the Gr/WS_2(1L)/Gr devices. (a) Plots the I_{ds}–V_{ds} curves of Gr/WS_2(1L)/Gr device with various gate voltages during the forward sweep in dark condition. (b) Transfer curves for the Gr/WS_2(1L)/Gr photodetectors under the exposure of light (532 nm wavelength) with increasing powers. (c) Photocurrent as a function of the back-gate voltage based on the transfer curves in (b). The light green region marks the photocurrent transition area. (d) Photoresponsivity and (e) photo-gain of the Gr/WS_2(1L)/Gr photodetector with increasing incident laser power with source-drain bias at 0.5V. (f) Band diagrams of the vertical Gr/WS_2/Gr structure with positive bias voltage (Gr_B is connected to source and Gr_T is connected to

drain). qV_{ds} is the fermi level difference of two graphene induced by bias voltage. The solid black dots represent the photo-excited electrons in WS_2. The orange shape is the electrostatic potential barrier formed in the vdW gap between graphene and WS_2. The black arrows represent the electrons generated in WS_2 tunnel through the potential barriers to the Gr_B and Gr_T.

5.2.5 Electrical and Opto-electrical Measurement of Gr/WS_2(2L)/Gr Vertical Heterostructure

When examining the photoresponse behavior for devices with bilayer WS_2 we found a significant difference between Gr/WS_2(2L)/Gr vertical heterostructure devices and Gr/WS_2(1L)/Gr devices. The I_{ds}-V_{ds} curves of both Gr/WS_2(1L)/Gr and Gr/WS_2(2L)/Gr devices pass through the origin at various gate voltages in the dark condition. As shown in **Figure 5.6**a, when illuminated with light, the bilayer WS_2 based device shows much higher short-circuit current (I_{sc}) and open-circuit voltage (V_{oc}) (For the Gr/WS_2(2L)/Gr device, $I_{sc} = 9 \times 10^{-7}$A, V_{oc} = 22 mV) compared with that of Gr/WS_2(1L)/Gr ($I_{sc} = 1.5 \times 10^{-8}$A, V_{oc} = 0.2 mV (The comparison of short-circuit current density is shown in **Figure A1**(b)). For the Gr/WS_2(2L)/Gr devices, when the V_g decreases, there is a gradual upshift of the I_{ds}-V_{ds} curve (see **Figure 5.6**b, illuminated with a fixed laser power). **Figure 5.6**c illustrates the dependence of the I_{sc} and $|V_{oc}|$ on the V_g. It shows that V_g can modulate both the I_{sc} and $|V_{oc}|$ effectively. When V_g = 0 V, the I_{sc} and $|V_{oc}|$ are at around 1×10^{-6} A and 22 mV. When V_g decreases, both the I_{sc} and $|V_{oc}|$ increase to 1.3×10^{-6} A and 26 mV at -10V. When V_g increases, both I_{sc} and $|V_{oc}|$ decrease, reaching 4×10^{-7} A and 14 mV at 60V. And the decreasing slope becomes smaller at higher V_g. It should be noted that the modulation of the photocurrent by the external gate voltage does not generate additional dark current. The power of the incident light also has the ability to tune the I_{sc} and $|V_{oc}|$ of our Gr/WS_2(2L)/Gr devices, as shown in **Figure 5.6**d. Both I_{sc} and $|V_{oc}|$ scale exponentially with incident light power and show no indication of saturation over the measured range of optical powers. From the direction of the V_{oc}, it is easy to exclude the dominance of the PTE effect in our vertical heterostructure. When V_g increases from -10 V to 60 V, the doping

levels of the Gr_B and Gr_T turn from p+/p to n+/n, as shown in **Figure 5.6**e. If PTE is the dominant mechanism of photocurrent generation, the sign of the V_{oc} should reverse when V_g passed a certain value between -10 V and 60 V, which has been confirmed by Gabor et.(*147*) To be specific, because of the substrate can dissipate heat well, the Gr_T has higher temperature than the Gr_B, which leads to the charge carriers transporting from Gr_T to Gr_B. So, when the charge carrier changes from electrons to holes, the direction of photocurrent should reverse. This means when the V_g changes from 60 V to -10 V, the direction of V_{oc} should reverse. But in our experiment, we observed that V_{oc} keeps moving in the negative direction as V_g is swept from 60 V to -10 V, which indicates that PTE is not the dominate mechanism of the photocurrent in our experiment.

As mentioned above, Gr_T is more p-doped than the Gr_B in the vertical junction, leading to a potential difference between the two graphene electrodes in our vertical Gr/WS_2/Gr devices. When light is absorbed by the WS_2 monolayer, e-h pairs are generated, with around 60% of the free electrons and holes rapidly bound into excitons, on time scales shorter than 1 ps.(*149*, *150*) So the photocurrent in our devices is mainly dependent on the exciton dissociation. The exciton binding energy of monolayer WS_2 is as high as 0.71 eV at room temperature over a magnitude order than conventional semiconductors.(*65*, *151*) The large binding energy of excitons in monolayer WS_2 suppresses the separation of e-h pairs and thus the number of free charge carriers contributing to the photocurrent are small without applied bias voltage. The e-h pairs in monolayer WS_2 also rapidly recombine across the direct band gap.(*65*, *152*) So the I_{sc} we observed in the monolayer WS_2 vertical devices is rather small.

The reason for the high I_{sc} and $|V_{oc}|$ in the bilayer WS_2 vertical devices is first due to the increased absorbance of light in bilayer WS_2 compared with its monolayer counterpart. So the generated I_{sc} in bilayer vertical devices should be at most two times that generated in monolayer WS_2 devices if we only considered the absorbing differences in bilayer WS_2. The average I_{sc}

we measured in bilayer WS_2 vertical devices is 10 times of that in monolayer WS_2 devices, so there must be other factors which contribute to the increased I_{sc} in bilayer WS_2 vertical devices. We attribute the high I_{sc} to an increased efficiency of exciton dissociation in bilayer WS_2 compared to monolayers, which is ascribed to two reasons. (i) Lower exciton binding energy in bilayer WS_2, which is half of that in monolayer WS_2.(*153*) This enables higher probability of exciton dissociation and thus higher I_{sc} and $|V_{oc}|$. (ii) Longer exciton life time in bilayer WS_2. The lifetime of intra-layer excitons is longer than that of excitons in monolayer WS_2, because bilayer WS_2 has an indirect band gap. The momentum conservation requires extra phonons for the recombination of exciton in bilayer WS_2. Fast dissociation time was observed in few layer MoS_2 (700 fs), which is much shorter than that for excitons in monolayer MoS_2 (60 ps).(*154*)

The V_g dependence of the I_{sc} and $|V_{oc}|$ in the Gr/WS_2 (2L)/Gr vertical devices is explained using the energy band shift in **Figure 5.6**e. By applying negative (positive) V_g on our devices, both Gr_B and bottom WS_2 layer are more influenced by the gate voltage due to closer proximity, inducing stronger p-doping effect (n-doping) than the top WS_2 and Gr_T. This could cause an energy band offset between the bottom and top WS_2 layers in bilayer WS_2, similar to the effect of an external electric field induced energy band offset in bilayer MoS_2 proposed by Chu et.al.(*155*) The value of band offset represents the electric field strength applied on the bilayer WS_2. The two layers in bilayer WS_2 are strongly coupled as they are grown directly by a CVD process rather than being assembled manually by a layer-by-layer transfer.(*156*) Similar to the heterostructure, the staggered band of bilayer WS_2 enables a quick dissociation of photo-generated intra-layer excitons to free carriers (electrons and holes).(*92*) The interlayer excitons formed between two layers of WS_2 also have a low binding energy, with a similar value of binding energy to that of intra-layer excitons when the applied electric field is at a low value.(*157*) The lifetime of the interlayer exciton in the $MoSe_2/WSe_2$ heterostructure is as long as 1.8 ns, because of the low exciton energy and its spatially indirect nature, even when the

lifetime of the intra-layer exciton in monolayer $MoSe_2$ and WSe_2 is short.(*97*) So in our bilayer WS_2 devices, the out-of-plane interlayer exciton is also assumed to have a long lifetime on the order of ns, which is much longer than the lifetime of excitons in monolayer WS_2. The low PL signal of WS_2 bilayers between two graphene sheets prevents direct measurements of the signals. When applying negative gate voltage, the CBM and VBM of bottom layer WS_2 shift higher than that of bottom WS_2. The tunneling barrier difference between Gr_B/WS_2 and Gr_T/WS_2 is also enlarged. This band-offset facilitates the electrons and holes transfer to the top and bottom WS_2 respectively, leading to more electrons tunneling to the top graphene and less to the bottom graphene. So, the net photocurrent increases with negative gate voltage. The explanation is the same as applying positive gate voltage.

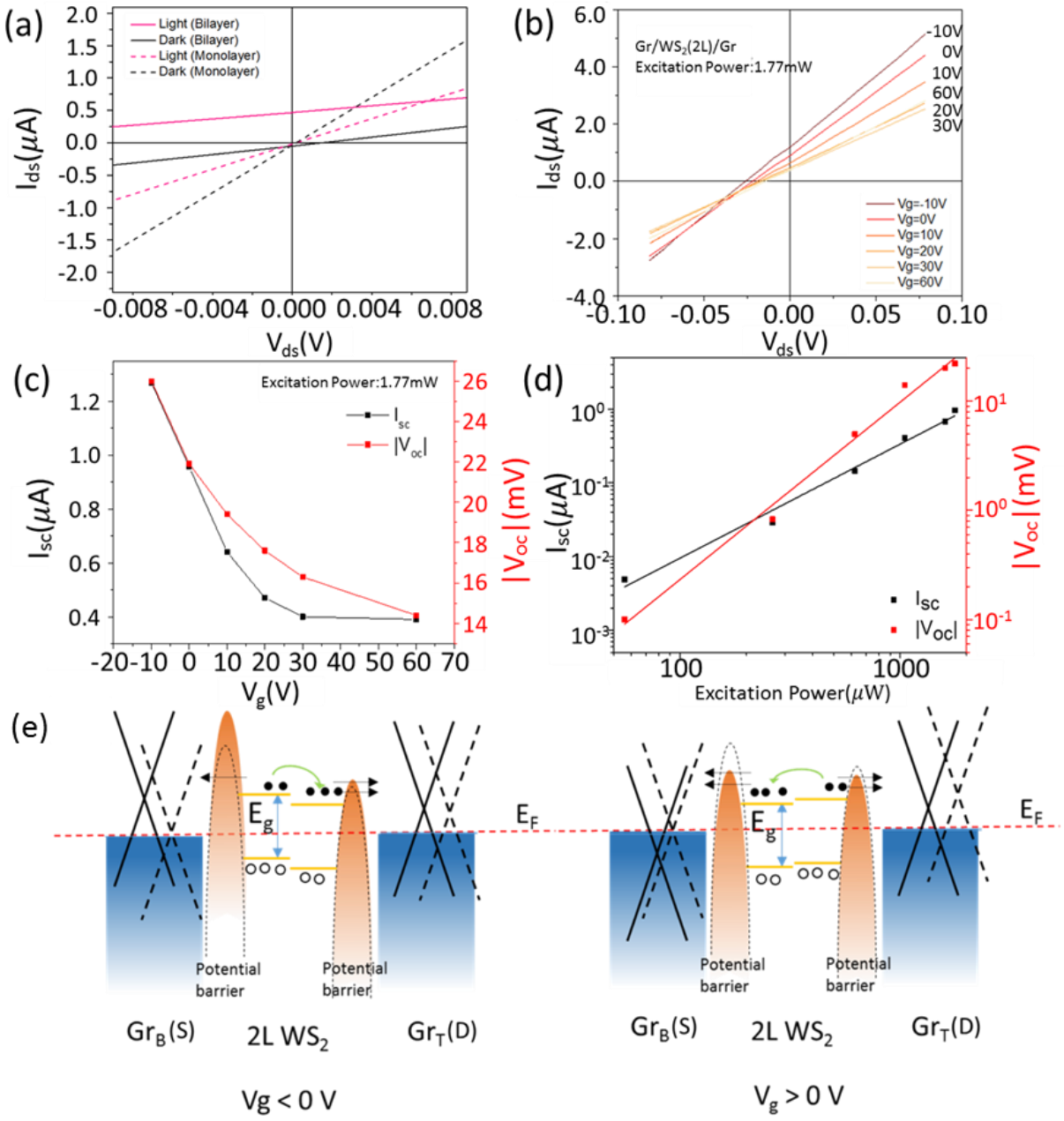

Figure 5.6. Photovoltaic effect of Gr/WS_2(2L)/Gr vertical devices. (a) Output characteristics of Gr/WS_2(1L)/Gr and Gr/WS_2(2L)/Gr vertical devices in dark and under 532 nm illumination. (b) Output characteristics of Gr/WS_2(2L)/Gr vertical device with various back gate voltages under the excitation power at 1.77 mW for 532 nm. (c) The dependence of short-circuit-current (I_{sc}) and open-circuit voltage (V_{oc}) on the V_g with the excitation power fixed at 1.77 mW for 532 nm. (d) The power-law dependence of I_{sc} and $|V_{oc}|$ on the excitation power with the V_g = 0 V, the red dots represent $|V_{oc}|$ and black dots represent I_{sc}. The black and red lines are the fitting curves. (e)The band diagrams of Gr_B/WS_2 (2L)/Gr_T with negative (left) and positive (right) V_g and zero bias voltage. The dotted straight line and parabola represent graphene's energy band the potential barrier with zero gate voltage and bias voltage, while the solid line and parabola are graphene's energy band and potential barrier with non-zero gate voltage and zero bias voltage. The

red dotted line is the fermi level of the whole device. With non-zero V_g, the bottom WS_2 feels stronger electric field compared with the top WS_2, causing an energy band offset in bilayer WS_2.

5.3 Conclusion

In summary, we have realized the large-scale fabrication of ultrathin Gr/WS_2/Gr cross bar photo-detecting transistor device. All the materials used in the devices are synthesized by CVD methods with large domain sizes and relatively homogeneous layer number within each domain, enabling comparisons of monolayer and bilayer crystals. The Gr/WS_2(1L)/Gr devices show high photo-gain reaching around 136 when illuminated with 532 nm light (V_g = -80 V). With the Gr_T more p-doped than the Gr_B, the Gr/WS_2(2L)/Gr devices exhibit significant photovoltaic effect but very weak photovoltaic effect for Gr/WS_2(1L)/Gr devices. We attribute the difference to the reduced binding energy and long life time of excitons in bilayer WS_2 which contribute more free charge carriers for the photovoltaic effect. With changing the back-gate voltage, the photovoltaic effect can be tunable in the Gr/WS_2(2L)/Gr devices. Our finding reveals the importance of controlling the number of layers of sandwiched photoactive material in the vertical devices.

5.4 Contribution Statement

Dr. Ye Fan and Haijie Tan provided training in device fabrication and established the software interface for electrical characterization. Dr. Haijie Tan also discussed with me about the results. Dr. Yuewen Sheng provided CVD-grown graphene for this study. Wenshuo Xu provided me some WS_2 samples.

Chapter 6 Symmetry Control of Reversible Photovoltaic Current Flow in Ultrathin All 2D Vertically Stacked Graphene/WS_2/MoS_2/Graphene Devices

6.1 Introduction

Atomically thin vertical heterostructures are promising candidates for opto-electronics application, especially for flexible and wearable technologies. However, as we mentioned in last chapter, up until now, most of the heterostructures are based on mechanically exfoliated two dimensional materials, which severely limit the mass-production of vertical heterostructure based devices. Before, we fabricated arrays of ultrathin vertically stacked opto-electronic tunneling devices using all chemical vapour deposition grown 2D materials. Monolayer graphene was utilized as top and bottom electrodes, and transition metal dichalcogenides (TMDs) of monolayer and bilayer WS_2 were used as active semiconductors to study the photovoltaic effect. Stimulated by the idea that type-II energy alignment can facilitate the separation of electron-hole pairs, we substituted bilayer WS_2 with MoS_2:WS_2 vertical stacks. And large photovoltaic effects in more than 40 devices are achieved. The large number of devices allows for statistical verification of performance and comparative behavior, which is not easily achievable with mechanical exfoliated materials. The photo-voltage in the

graphene/TMD-heterobilayer/graphene (Gr/TMD-HB (MoS_2:WS_2)/Gr) increases up to ten times that generated in the monolayer TMD devices under the same optical illumination power, due to efficient charge transfer between WS_2 and MoS_2 and extraction to graphene electrodes. By applying external gate voltages (V_g), the band alignment can be tuned, which in turn controls the photovoltaic effect in the vertical heterostructures. The tunneling assisted interlayer charge recombination also plays a significant role in modulating the photovoltaic effect in the Gr/TMD-HB/Gr. Controlled reversible photo-current flow by switching the ordering of the MoS_2:WS_2 heterostructure stack relative to the substrate were demonstrated. These results provide important insights into the application of TMDs and graphene in ultrathin opto-electronics using scalable chemical vapour deposition grown materials.

6.2 Results and Discussion

6.2.1 Fabrication of Gr/TMD Heterobilayer/Gr Vertical Device

The schematic diagram of the side view of the Gr_B/TMD-HB/Gr_T vertical device is shown in the center of **Figure 6.1**a (Step v). The vertical devices are constructed with WS_2/MoS_2 hetero-bilayer vertically sandwiched between two graphene electrodes. The fabrication process of such a vertical photodetector is shown in **Figure 6.1**a (Step i-v). A CVD synthesized monolayer graphene film was first transferred onto a silicon chip with 300 nm SiO_2 using a poly (methyl methacrylate) (PMMA) thin-film support and patterned into ribbons of 10 μm width by electron-beam lithography (EBL) and reactive ion etching (RIE) to form the bottom graphene electrodes (Step i, **Figure 6.1**a). A layer of CVD synthesized WS_2 domains are transferred onto bottom graphene electrodes followed by transferring of another layer of CVD grown MoS_2 domains. Due to the advantage of CVD method, the WS_2 and MoS_2 domains are distributed randomly on the substrate with high density, which enables a high possibility to produce WS_2/MoS_2 hetero-bilayer (Step ii and iii, **Figure 6.1**a). Another layer of pre-patterned

monolayer graphene ribbons was subsequently transferred onto the substrate/$Gr_B/WS_2/MoS_2$ as the top electrodes with a perpendicular alignment to the bottom graphene ribbons (Step iv, **Figure 6.1**a). At last, the bond pads (Cr/Au (10 nm/80 nm)) were made on the graphene electrodes with EBL and thermal evaporation (Step v, **Figure 6.1**a). By optimizing the CVD synthesis process, both monolayer and bilayer WS_2 domains can be obtained on the same chip, which ensures us being able to construct Gr/TMD-HB/Gr vertical devices with different TMD materials sandwiched, including $Gr_B/WS_2(1L)/Gr_T$, $Gr_B/MoS_2(1L)/Gr_T$, $Gr_B/WS_2(2L)/Gr_T$, $Gr_B/WS_2(1L)/MoS_2(1L)/Gr_T$ and $Gr_B/WS_2(2L)/MoS_2(1L)/Gr_T$. By reversing the stacking order of WS_2 and MoS_2, we also acquire $Gr_B/MoS_2(1L)/WS_2(1L)/Gr_T$ vertical devices. The bottom right image in **Figure 6.1**a is the top view of the $Gr_B/WS_2(1L)/MoS_2(1L)/Gr_T$. With the method we described above, the vertical devices array can be acquired for our study. Figure 6.1b is the SEM image of the device array, where we can see that WS_2 and MoS_2 domains were scattered on the 1cm×1cm chip with high density. A zoom in SEM image of a typical $WS_2(1L)/MoS_2(1L)$ hetero-bilayer sandwiched between graphene electrodes is shown in **Figure 6.1**c In the device, the MoS_2 domain and graphene ribbons are highlighted with blue and orange dashed lines, while the WS_2 domains are very big, covering most area of the device, with the edge being marked with yellow lines. The top graphene and bottom graphene overlapping area is completely sandwiched by WS_2 and MoS_2.

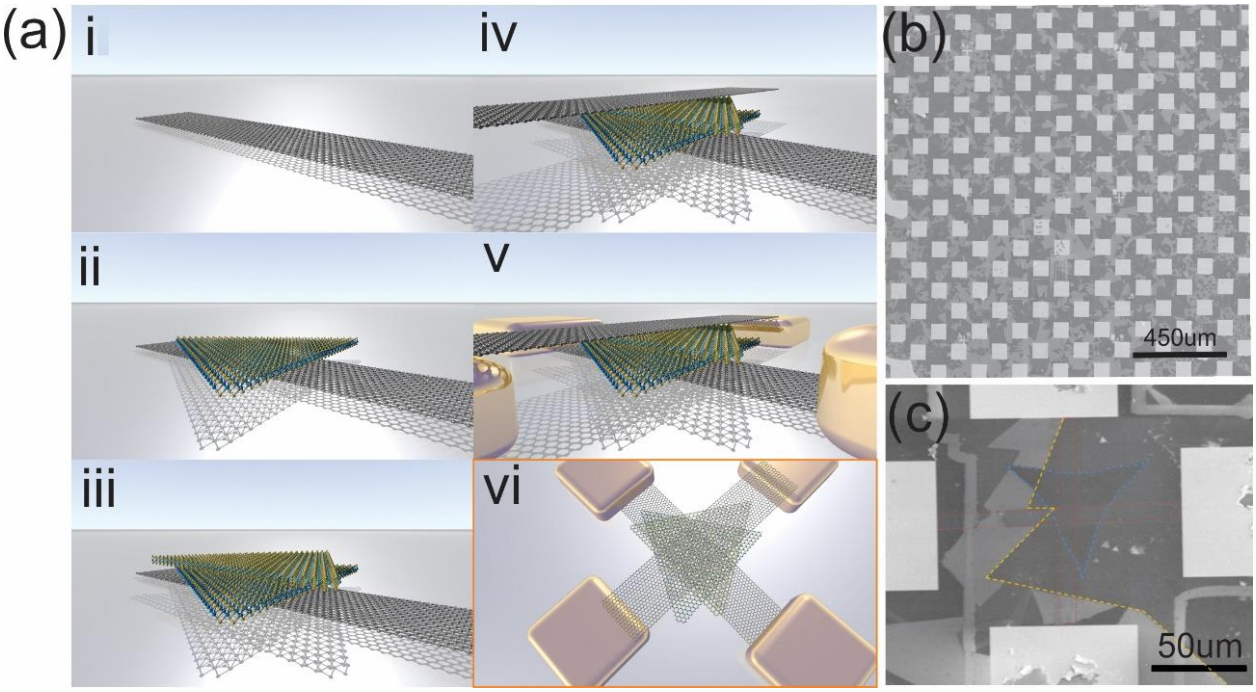

Figure 6.1. Fabrication process schematic and images of devices (a) Fabrication process for creating the Gr/TMD-HB/Gr vertical device array. Step i: Pattern graphene ribbon as electrodes using electron-beam lithography. Step ii: Transfer WS_2 domains onto bottom graphene electrodes. Step iii: Transfer MoS_2 domains onto Gr/WS_2. Step iv: Transfer top graphene ribbon as top graphene electrodes. Step v: Deposit Cr/Au (10 nm/80 nm) onto graphene electrodes as bond pads. vi is the top view of $Gr_B/WS_2(1L)/MoS_2(1L)/Gr_T$ heterostructure photodetector. (b) Scanning electron microscope (SEM) image $Gr_B/WS_2(1L)/MoS_2(1L)/Gr_T$ heterostructure photodetectors array. The scale bar is (c) The zoom in image of a $Gr_B/WS_2(1L)/MoS_2(1L)/Gr_T$ vertical device from the array in (b).

6.2.2 Raman and PL Characterization

Figure 6.2a-d demonstrate the SEM and optical images of monolayer WS_2, MoS_2 and WS_2/MoS_2 stacks. WS_2 and MoS_2 domains can be well distinguished from the shape, with WS_2 having straight edges, while MoS_2 domains showing concave edges. Raman and photoluminescence were conducted to examine the quality and number of layers of WS_2, MoS_2 and WS_2/MoS_2, as shown in **Figure 6.2**e and f. PL intensity at WS_2/MoS_2 area quenches compared with monolayer WS_2, indicating the charge transfer between WS_2 and MoS_2 at the junction (**Figure 6.2**e). Compared with monolayer WS_2, monolayer MoS_2 has very low PL quantum yield, which can be seen from **Figure 6.2**e. In the WS_2/MoS_2 area, the typical Raman

modes A_{1g} and E_{2g} of both WS_2 and MoS_2 monolayer appear at the same frequencies as their isolated monolayers, with a slightly right shift of the mode A_{1g} from WS_2 in the WS_2/MoS_2 compared with standalone WS_2, which is likely because A_{1g} is more sensitive to the influence from neighboring layer (**Figure 6.2**f).

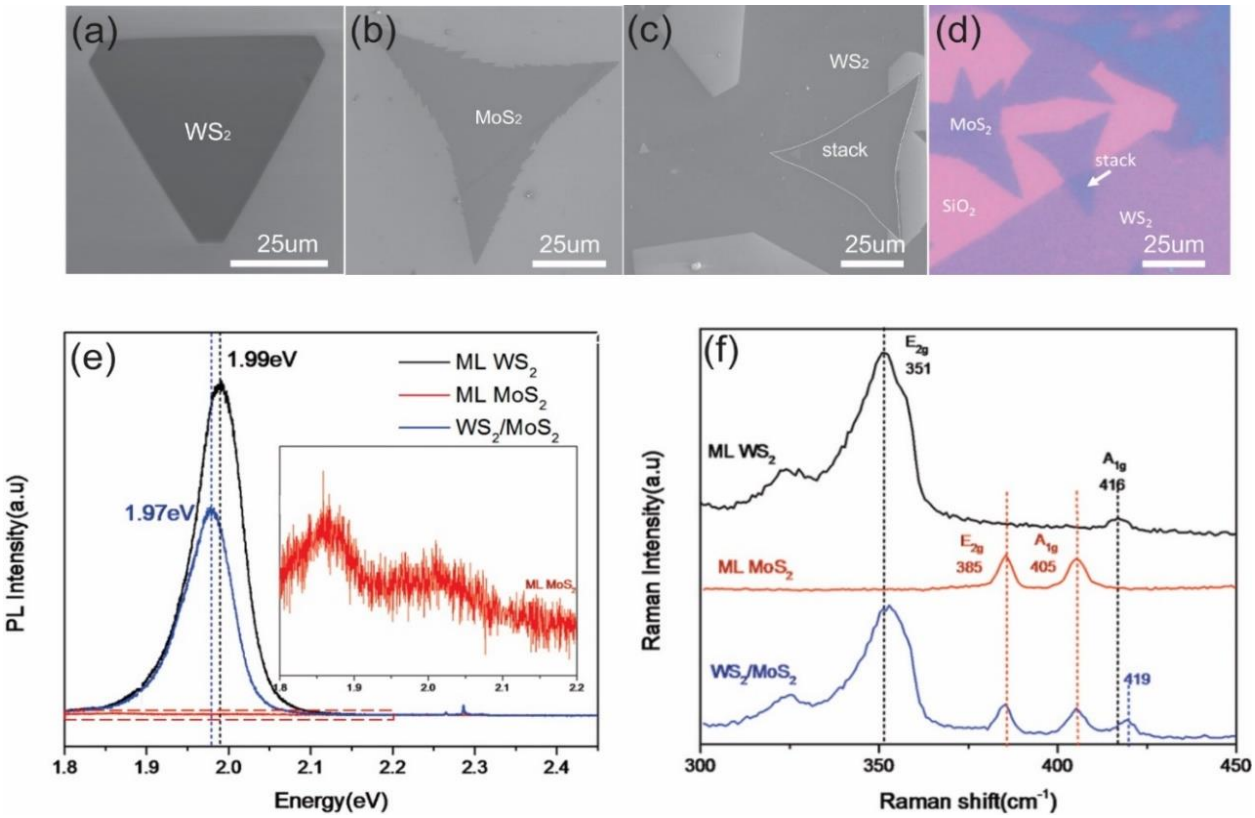

Figure 6.2. Optical characterization of WS_2,MoS2 and their stacks. (a-c) SEM images of monolayer WS_2, MoS_2 and WS_2/MoS_2 stack. (d) Optical image of the WS_2/MoS_2 stacks. (e) PL spectra of monoalyer WS_2,MoS_2 and their stack. The PL intensity at the junction area decreases compared monoalyer WS_2. (f) Raman spectra of monolayer WS_2, MoS_2 and WS_2/MoS_2 stack.

6.2.3 Opto-electrical Measurement

Before the opto-electrical measurements of the heterostructure devices, the electrical properties of monolayer WS_2 and MoS_2 field-effect transistor based on SiO_2 (300nm)/Si substrate were studied, as shown in **Figure 6.3**a and b. Both of the transistors are conductive when applied with positive gate voltage. The transfer curves indicate both WS_2 and MoS_2 show n-type conductive property. The output characteristics of the six types of vertical photodetectors

illuminated with light (wavelength = 532nm, light power = 270uW) and without light are shown in **Figure 6.4**, with the schematic illustration of the vertical stacking shown in **Figure 6.4**a-c, g-i. In the optical images in **Figure B1**(a-f), the Gr_T and Gr_B are marked with white color, while the WS_2 and MoS_2 domains are marked with bluish and reddish colors, respectively. For optical excitation, we use a laser spot size of ~2μm, which is much smaller than the graphene ribbon width enabling comparisons across devices with slightly variable ribbon widths.

Similar to our previous reports in homobilayer vertical structures,(*158*) before any electrical measurements were conducted on a device, a nano-tip probe was used to mechanically etch the graphene electrodes connected to other devices to isolate the device under measurement. During the whole measurement process, the Gr_B electrodes are always connected to source, while the voltage bias is applied through Gr_T electrodes. In the output characteristics measurement, the devices are gated with -60V back-gate voltage. All the types of devices we measured show output characters passing through origin in dark condition (black curve in **Figure 6.4**d-f, j-l). When the junctions are illuminated with light, different types of devices show different responses. For $Gr_B/WS_2(1L)/Gr_T$ and $Gr_B/MoS_2(1L)/Gr_T$ devices (**Figure 6.4**j, k), the I_{ds}-V_{ds} curves still pass through origin (the shift of I_{ds}-V_{ds} is too small to be detected by our equipment) under illumination. Other vertical heterostructure based devices exhibit a detectable upshift or downshift of the I_{ds}-V_{ds} curves with different magnitudes of optical illumination. The shift of the I_{ds}-V_{ds} under illumination suggests the existence of photovoltaic effect, which can be quantified with short-circuit current (I_{sc}) and open-circuit voltage (V_{oc}). In $Gr/WS_2(2L)/Gr$ devices, the I_{sc} and $|V_{oc}|$ reach around 12nA and 1.7 mV, which is consistent with the previous report under similar light intensity illumination.(*158*)

Manually stacking $WS_2(1L)$ and $MoS_2(1L)$, which show no obvious photovoltaic effect, and sandwiching them between graphene electrodes to form $Gr_B/WS_2(1L)/MoS_2(1L)/Gr_T$, the I_{sc} and $|V_{oc}|$ even slightly higher than those of bilayer WS_2 device can be detected, with I_{sc} and

$|V_{oc}|$ reaching 14nA and 2.7mV. When the stacking sequence of WS_2 and MoS_2 reverses, similar magnitude of I_{sc} and V_{oc} also observed, but with negative I_{sc}. Our results above show an easy way to enhance the photovoltaic effect in atomically thin vertical devices simply by stacking two TMDs together. Under the illumination light with wavelength of 532 nm (E = 2.3 eV), the absorbance of bilayer WS_2 is almost double magnitude of monolayer WS_2 (8.2%), while for the WS_2/MoS_2 hetero-bilayer, the absorbance was reported to be lower than the sum of the absorbance of the individuals layers (MoS_2: 9.3%, WS_2/MoS_2: 10.8%).(*146*) With lower absorbance, the $Gr_B/WS_2(1L)/MoS_2(1L)/Gr_T$ devices are expected to show weaker photovoltaic effect, but the experimental results reveal that the $Gr_B/WS_2(1L)/MoS_2(1L)/Gr_T$ devices have marginally higher photovoltaic effect compared with $Gr_B/WS_2(2L)/Gr_T$ when illuminated with green light (E = 2.3 eV). The enhancement of the photovoltaic effect is assumed to be due to the type-II energy band formed in WS_2/MoS_2 which can facilitate the exciton dissociation and charge separation.(*159*) The photovoltaic effect generated from type-II energy band can be further confirmed by the negative I_{sc} in the $Gr_B/MoS_2(1L)/WS_2(1L)/Gr_T$, shown in **Figure 6.4**f.

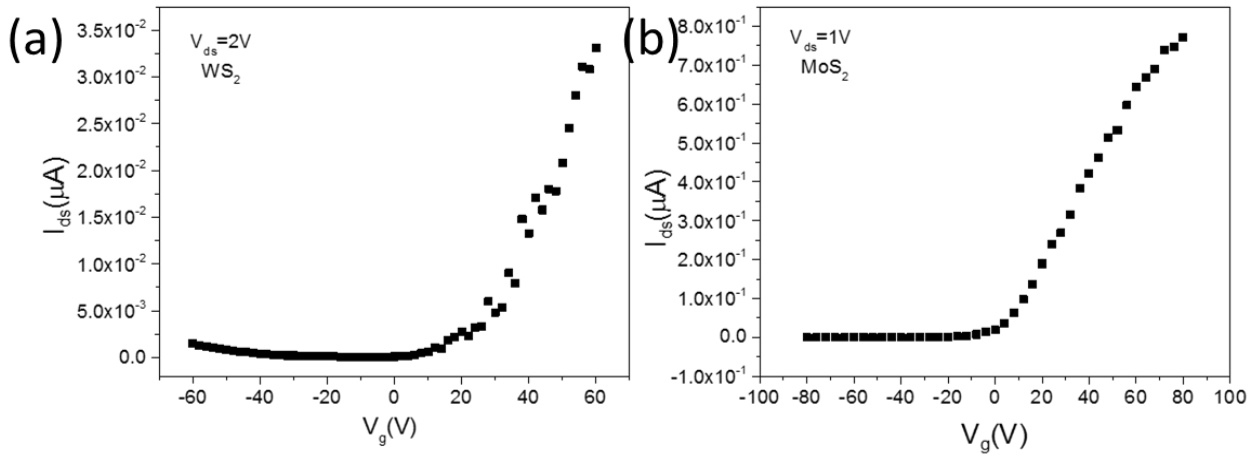

Figure 6.3. Transfer characterisctics of Monolayer WS_2 and MoS_2 based FET. (a) The transfer curve of monolayer WS_2 FET shows n-type characteristic of WS_2. (b) The transfer curve of monolayer MoS_2 FET shows n-type characteristic of MoS_2.

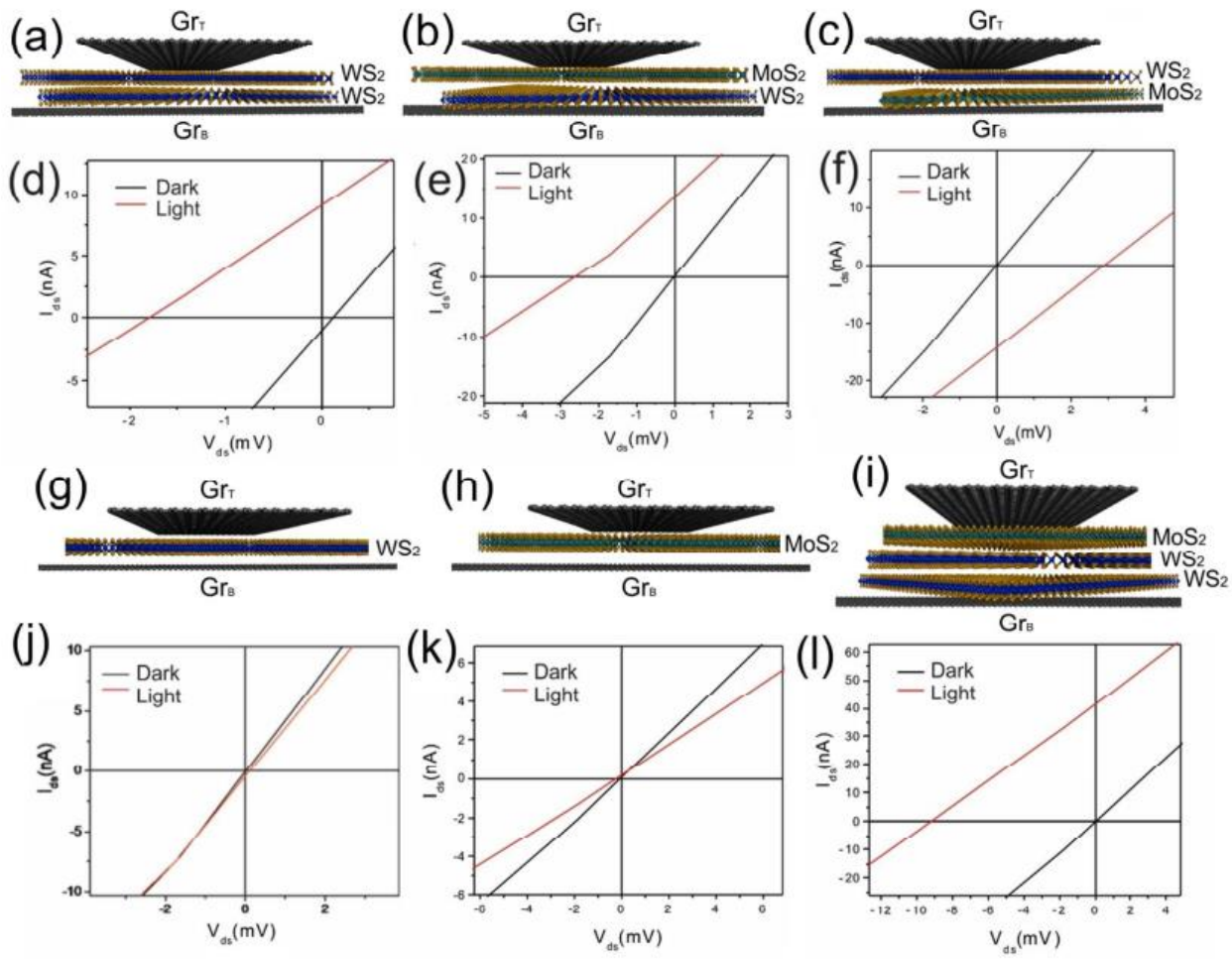

Figure 6.4. Photovoltaic effect of Gr/TMD/Gr vertical devices with different thicknesses of sandwiched TMD layers. (a-c, g-i) Schematic illustrations of the vertical stacked ordering of devices and (d-f, j-l) their source-drain current as a function of applied source-drain bias for (a,d) $Gr_B/WS_2(2L)/Gr_T$, (b,e) $Gr_B/WS_2(1L)/MoS_2(1L)/Gr_T$, (c,f) $Gr_B/MoS_2(1L)/WS_2(1L)/Gr_T$, (g,j) $Gr_B/WS_2(1L)/Gr_T$, (h,k) $Gr_B/MoS_2(1L)/Gr_T$ and (i,l) $Gr_B/WS_2(2L)/MoS_2(1L)/Gr_T$, with (red) and without (black) illumination at 532nm.

To further understand the photocurrent mechanisms in the vertical heterostructure devices, we studied the dependence of the output characteristics of the Gr/TMD-HB/Gr on the back-gate voltage under illumination (power: 270μW, wavelength: 532nm). As shown in **Figure 6.5**a and b, the gate voltage provides strong modulation on the photovoltaic effect of the both $Gr_B/WS_2(1L)/MoS_2(1L)/Gr_T$ and $Gr_B/MoS_2(1L)/WS_2(1L)/Gr_T$ devices. With the decrease of the V_g from 60V to -60V, the photovoltaic effect in both structures becomes stronger. In **Figure 6.5**c and d, we show the absolute value of I_{sc} (black) and V_{oc} (red) as a

function of V_g with a fixed illumination power. For the $Gr_B/WS_2(1L)/MoS_2(1L)/Gr_T$ device, the I_{sc} and $-V_{oc}$ decrease monotonously from 12nA and 2.4mV to 3nA and 0.7mV when the V_g varied from -60V to 60V. For $Gr_B/MoS_2(1L)/WS_2(1L)/Gr_T$, highest photovoltaic effect appears at V_g = -60V and gradually decreases with increasing V_g. The huge changes in both I_{sc} and V_{oc} are significantly different to the TMD(A)/TMD(B) hetero-bilayer devices previously reported, where the V_{oc} almost keeps constant when the V_g changes.(*160*, *161*) This behavior in our vertical heterostructure based devices is attributed to the small tunneling resistance in the Gr/TMD-HB/Gr vertical structure induced by the thin TMD layers.

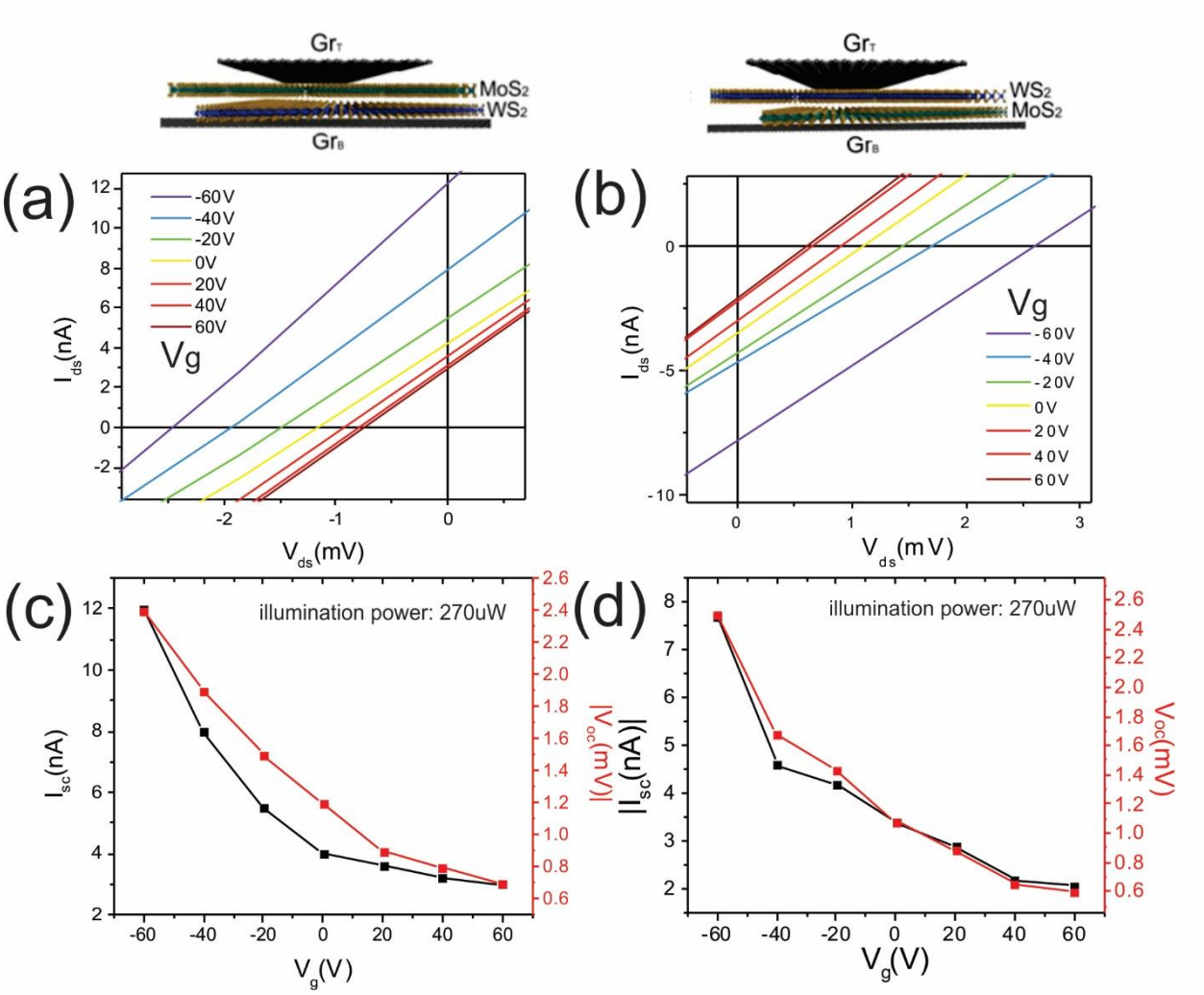

Figure 6.5. Dependence of photovoltaic effect on back-gate voltage. Output characteristics of (a) $Gr_B/WS_2(1L)/MoS_2(1L)/Gr_T$ and (b) $Gr_B/MoS_2(1L)/WS_2(1L)/ Gr_T$ vertical device with various back-gate voltages under the excitation power at 270 μW for 532 nm (c-d) The dependence of short-circuit current (I_{sc}) and open-circuit voltage (V_{oc}) of (c) $Gr_B/WS_2(1L)/MoS_2(1L)/Gr_T$ and (d) $Gr_B/MoS_2(1L)/WS_2(1L)/ Gr_T$ vertical device on the gate voltage.

The generation of the photovoltaic effect in the Gr_B/TMD-HB/Gr_T device can be explained in terms of the photo-generated charge separation at the type-II energy band and further collected by the graphene electrodes (~1 ps),(*162*) as schematically illustrated in **Figure 6.6**. We have revealed that the photovoltaic effect generated in the Gr/WS_2(2L)/Gr heterostructured devices was attributed to the asymmetric tunneling barrier height between Gr_B/WS_2 and WS_2/Gr_T.(*158*) However, we assume that the asymmetric tunneling barrier height plays a minor role in determining the photovoltaic effect in our $Gr_B/WS_2/MoS_2/Gr_T$ structures.

This can be confirmed by the reversed direction of the V_{oc} and I_{sc} detected in the $Gr_B/MoS_2/WS_2/Gr_T$ devices. **Figure 6.6**c depicts the schematic structure of the $Gr_B/WS_2(1L)/MoS_2(1L)/Gr_T$ device and the circuit for the photoelectrical measurement. The diagram of the energy band of the heterostructure and the gate voltage modulation of the band structure are also shown in **Figure 6.6**a and b. The energy offset between WS_2 and MoS_2 monolayer CBMs (VBMs) is reported to be 0.27meV (0.35meV) when there is no external bias applied.(*98*, *163*) The bandgaps of monolayer WS_2 and MoS_2 are 2.31eV and 2.39eV,(*98*) respectively, so when the WS_2/MoS_2 hetero-bilayer is illuminated with light (2.33eV), both WS_2 and MoS_2 are excited, with the electron-hole pairs being generated in both layers. The holes (electrons) in $MoS_2(WS_2)$ then transport to $WS_2(MoS_2)$ driven by the band offsets.(*98*) So when the WS_2/MoS_2 hetero-bilayer is contacted with Gr_T and Gr_B, the excessive electrons in MoS_2 will tunnel through the van der Waals gap to the Gr_T (~1ps)(*162*) with a higher rate than recombining with holes to form intra-layer excitons, contributing to the photovoltaic effect in the whole system. The reason for back gate voltage modulation to the photovoltaic effect is two-fold: (1) The back gate voltage poses a vertical electrical field to the heterostructure which has been theoretically proved to have linear modulation to the band offset between WS_2 and MoS_2.(*164*) (2) The increased carrier concentration in both WS_2 and MoS_2 reduces the lifetime and enhance the recombination rate of the photo-generated carriers under positive gate voltage.(*92*) To be specific, as we show in **Figure 6.6**b, when a negative gate voltage is applied to the device, the WS_2 and MoS_2 are both p-doped, but with bottom layer (WS_2) experiencing more p-doped than the top layer (MoS_2), which results in higher band offset, driven more photo-generated carriers to spatially separated layers.

However, with the decreasing of the gate voltage, the relative band-offset in MoS_2/WS_2 reduces, which suppresses the electrons transfer from WS_2 to MoS_2. Photocurrent measurements results show that the decreasing of the gate voltage enhances the photovoltaic

effect in the Gr_B/ MoS_2/WS_2/Gr_T devices, which indicates that the second factor we mentioned above compensates for the suppression of the charge transfer between WS_2 and MoS_2, which is less photo-generated charge loss due to smaller recombination rate under positive gate voltage. As it has been reported that tunneling mediated interlayer recombination: Shockley-Read Hall (SRH) and Langevin recombination, plays an important role in determining the photocurrent in TMD heterostructures.(*92*) The interlayer recombination is proportional to $n_M p_W^s$ or $n_M p_W/(n_M + p_W)$, depending on whether SRH or Langevin is the dominant, where n_M is the electron density in MoS_2, p_W is the hole density in WS_2. Under illumination and with positive gate voltage, more electrons are generated in both WS_2 (n_W) and MoS_2 (n_M) layers, which results in higher recombination. Photocurrent is determined by the difference between the gate-independent photo-generated charge rate and recombination rate, so I_{sc} is reduced with higher gate voltage.

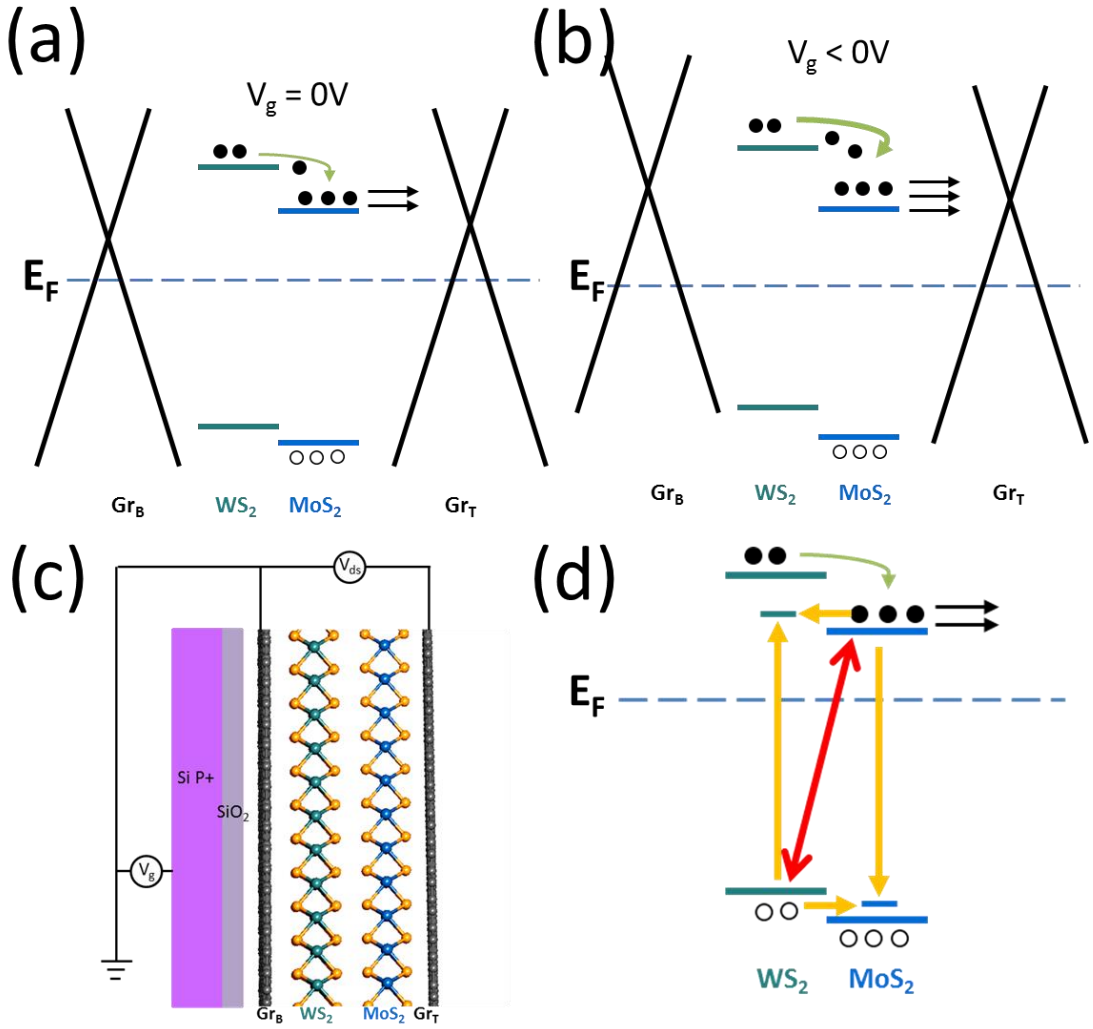

Figure 6.6. Schematic diagram of the photovoltaic mechanism. (a) and (b) The band diagrams of $Gr_B/WS_2/MoS_2/Gr_T$ without (left) and with negative (right) V_g and zero bias voltage. The green curvy arrow indicates the transfer of photo-generated electrons from WS_2 to MoS_2. The black line arrows represent the transfer of electrons from MoS_2 to graphene. The circles and the black solid dots are holes and electrons, respectively. (c) Schematic diagram of the $Gr_B/WS_2(1L)/MoS_2(1L)/Gr_T$ device and the electrical measurement circuit. (d) The interlayer charge recombination process between WS_2 and MoS_2. Yellow and red arrow lines indicate the SHR and Langevin recombination processes, respectively.

The dependence of photovoltaic effect of Gr/TMD-HB/Gr with different TMDs stacking sequences on the illumination power is further studied. The dependences of the I_{ds}-V_{ds} characteristics on the illumination power (P_{opt}) of the two type devices with V_g = -60V are shown in **Figure 6.7**a and b. For the $Gr_B/WS_2(1L)/MoS_2(1L)/Gr_T$, When the illumination power increased from 0μW to 174μW, the I_{ds}-V_{ds} curve experienced a gradually upshift from passing

origin to the I_{sc} reaching around 12nA (V_{oc}~-2.5mV), which indicates that the incident light power can effectively tune the I_{sc} and $|V_{oc}|$. What is interesting is that the resistance of the devices also increased gradually when increase the P_{opt}. This may due to the photogating effect which leads to negative photo-conductance (NPC, NPC means that the conductivity of a semiconductor reduces under light illumination) and is particularly common in hybrid structure.(*165*) In our heterostructure, the photo-generated holes in the TMD-HB are trapped in the band tail states of the TMD materials (WS_2 or MoS_2) due to the structural defects in the layer or induced by disorder.(*161*) The trapped holes then act as a local positive gate voltage to modulate the graphene electrodes conductance.(*99*) So when the P_{opt} increased, more electrons are transferred to graphene electrodes and more holes are trapped, leading to stronger positive gating effect on the graphene. Because the vertical devices we measured in Figure 6.7a was under -60V gate voltage, the positive gating effect from the trapped holes weakens the applied negative gating effect, resulting in decreased conductivity. This photo-gating effect can also be deduced from the shift of the Dirac point of graphene electrode under illumination. The combination of photo-gating and photovoltaic effect during the illumination process brings the crossover of the I_{ds}-$V_{ds(illumination)}$ and I_{ds}-$V_{ds(dark)}$ curves. Studying of the V_{cross} (the V_{ds} when the I_{ds}-$V_{ds(illumination)}$ cross with the I_{ds}-$V_{ds(dark)}$) can help us get better understanding of photocurrent generation mechanisms of our vertical heterostructure devices. At V_{cross}, no photocurrent is generated when device is illuminated with light, which means the photocurrent generated by photogating effect offsets the photocurrent generated by photovoltaic effect. There might be a photoconductive effect, but photoconductive effect always contributes to enhance the total current, which means the resistance under illumination will decrease.(*166*) Here for our devices, the photo-resistance increases, so it is assumed that the dominant effect is brought by the photo-gating effect.

Figure 6.7c and d depicts the power dependence of the $|I_{sc}|$ (black dots) and photoresponsivity (red dots) for $Gr_B/WS_2(1L)/MoS_2(1L)/Gr_T$ and $Gr_B/MoS_2(1L)/WS_2(1L)/Gr_T$ where the fitting curves of the I_{sc} and photoresponsivity are also shown (black and red lines). Photoresponsivity is defined as $R = I_{sc}/P_{opt}$. In both structures, $|I_{sc}|$ shows a power law dependence on P_{opt}. The fitting equation for I_{sc}-P_{opt} curve is $I_{sc} = P_{opt}^{\alpha}$. α is calculated to be 0.6 and 0.4 for in the $Gr_B/WS_2(1L)/MoS_2(1L)/Gr_T$ and $Gr_B/MoS_2(1L)/WS_2(1L)/Gr_T$ devices. The non-unity values further prove that the interlayer recombination through SRH and Langevin exists in the photocurrent generation process. The responsivity is then defined as $R = \frac{I_{sc}}{P_{opt}} = P_{opt}^{1-\alpha}$, so it decreases monotonously with the increase of the illumination power.

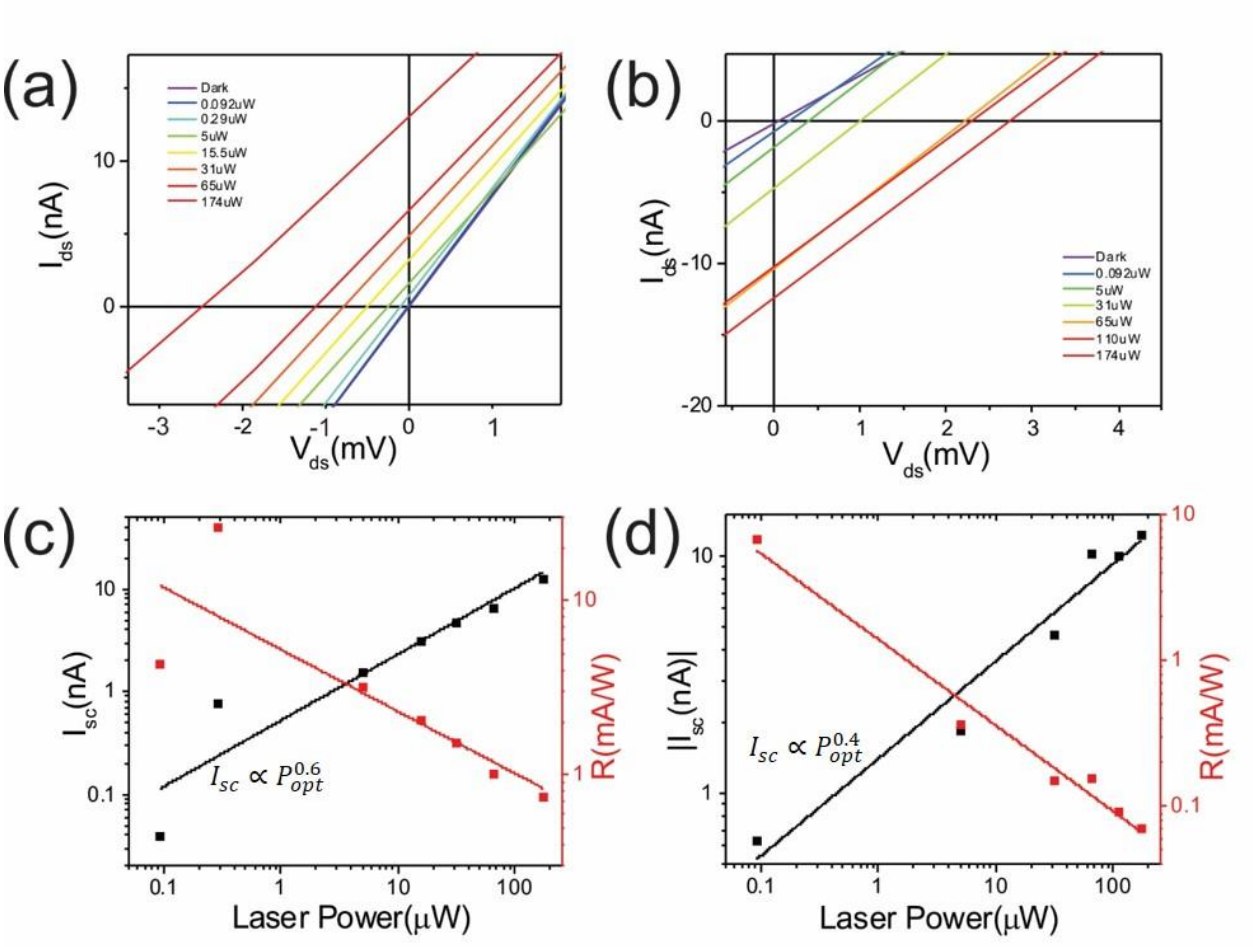

Figure 6.7. Dependence of photovoltaic effect on illumination power. Output characteristics of (a) $Gr_B/WS_2(1L)/MoS_2(1L)/Gr_T$ and (b) $Gr_B/MoS_2(1L)/WS_2(1L)/Gr_T$ vertical device with increasing illumination light power (532nm) with the V_g = -60V. (c-d) The dependence of short-circuit current (I_{sc}) and photoresponsivity of (c) $Gr_B/WS_2(1L)/MoS_2(1L)/Gr_T$ and (d) $Gr_B/MoS_2(1L)/WS_2(1L)/Gr_T$ vertical device on the illumination light power. The black and red lines are the fitting curves for the I_{sc} and responsivity.

6.3 Conclusion

In summary, we have successfully realized the fabrication of graphene/TMD-HB/graphene vertical devices. By making use of the type-II energy band formed between WS_2 and MoS_2, the photogenerated electrons (holes) are quickly separated and transfer from WS_2 (MoS_2) to MoS_2 (WS_2) when illuminated with 532 nm light, so that the photovoltaic effect can be induced in the vertical devices. We also discovered that the stacking sequence of WS_2 and

MoS_2 determines the sign of the photovoltage. The back-gate voltage can effectively modulate the photovoltaic effect by tuning the interlayer electron-hole recombination rate.

6.4 Contribution Statement

Wenshuo Xu, Qianyang Zhang and Linlin Hou provided WS_2 and MoS_2 samples. Dr. Yuewen Sheng provided graphene for this study. Wenshuo Xu also helped with the materials transfer. Hefu Huang and Dr. Viktoryia Shautsova discussed with me about some of the results.

Chapter 7 Conclusion and Future Outlook

In this DPhil thesis, I investigated the electronics and optoelectronics application of 2D materials, especially graphene, WS_2 and MoS_2. Novel properties could be induced by creating ultrathin vertical heterostructure with 2D materials. Here we summarize our main results and discuss the prospects for the future research.

7.1 Thesis Summary

In Chapter 4, I fabricated field-effect transistors on monolayer WS_2 with and without grain boundaries to investigate the influences brought by the high angle tilt GBs (19.5°) to the electrical properties of WS_2 FET. Three types of devices were demonstrated for comparison: FET with pristine WS_2, WS_2+$GB_{//}$, WS_2+$GB_{\perp}$ as the conductive channels. A negative shift of the threshold voltage of around 7V was observed for devices with WS_2+$GB_{//}$ compared with pristine WS_2. This negative shift was due to the n-doping effect at the GB, which was further confirmed with PL and KPM mapping at the GB. This finding reveals that the GB can have different conducting properties compared with pristine WS_2.

In Chapter 5, ultrathin vertical heterostructure arrays with graphene as transparent electrodes and WS_2 monolayers and bilayers as active light-active components were present for photo-detection study. Tunneling barriers were formed between WS_2 and top and bottom

graphene electrodes. The asymmetric tunneling barrier and the long lifetime excitons facilitate the generation of the photovoltage in the bilayer WS_2 devices. In monolayer WS_2 devices, because of the short exciton lifetime, photovoltaic effect is very weak. Our finding reveals the importance of controlling the number of layers of sandwiched photoactive material in the vertical devices.

Finally, in Chapter 6, vertical heterostructure devices consisting graphene-sandwiched vertical WS_2/MoS_2 heterostructure was demonstrated. The design of such a device was based on the gathered insights on the interlayer charge transfer between 2D crystals, and the understanding of the underlying mechanisms of photocurrent generation in photoconductors. Utilizing the interlayer excitonic formation and long photocarrier lifetimes at the WS_2/MoS_2 heterostructure, photovoltaic effect was achieved and the sign of the photovoltage is related to the WS_2 and MoS_2 stacking sequence. This work makes full use of the unique features brought by the type-II band alignment of TMD heterointerfaces for photodetection and photovoltaic application. The finding of this work reveals the possibility of stacking different 2D materials to tailor opto-electronic properties for specific applications.

7.2 Future Outlook

Devices based on 2D materials stacked vertical heterostructures are still under prospect discovery. In my work, all the artificial heterostructures are fabricated on SiO_2/Si substrate. As the 2D materials we used, TMDs and graphene, are transparent under visible light and flexible, it shows great potential for fabricating the vertical heterostructure on flexible substrates to be used as flexible and transparent photodetectors, solar cells and wearable devices. Besides, the artificial vertical heterostructure is not only confined within 2D materials, but can also combine 0D, 1D, 2D materials for other applications.

When talking about the challenges, first comes the problems within the materials themselves. The defects in the CVD synthesized 2D materials still remain as a hinder for the real application, as it brings variation to the materials properties and causes degradation to materials. Besides, 2D materials are very sensitive to the environment, which impacts the performance of devices based on these materials. Second comes the vertical heterostructure fabrication. Even though multiple techniques have been proposed for the vertical heterostructure fabrication, various problems still remain for each method, especially to ensure the clean interface and the ability to stack various materials. I believe vertical heterostructures will have a broad application in the future, not only for the electronic and optoelectronic application, but also for the biosensors, energy storage and so on.

Appendix A Supporting Information of Chapter 5

A.1. Photoresponse of $Gr_B/WS_2(1L)/Gr_T$ and statistical data of the I_{sc} and V_{oc}

Figure A1(a) is the photoresponse of the $Gr_B/WS_2(1L)/Gr_T$ stack to reduced light intensity (0.1μW) illumination under ambient condition. During the measurement process, the source-drain bias was fixed at 1V, and gate voltage applied was 0V. Before illumination, dark current was at 19.71μA. When the light illuminated on the device, the current gradually decreased to and stabilized at 19.56μA. The current increased again when the light was turned off. This photoresponse measurement proves that the negative photocurrent detected under reduced light intensity in **Figure 5.5**c is originated from absorption of light, rather than the measurement variation.

Figure A1(b) depicts the distribution of the short-circuit-current density (J_{sc}) of 10 devices of monolayer and bilayer WS_2 sandwiched between graphene when $V_g = 0$ V. We find that the number of layers of WS_2 has a large influence of the J_{sc}. Even though the J_{sc} in each category may have fluctuation, the difference between the J_{sc} of monolayer and bilayer WS_2 devices is obvious. The devices with bilayer WS_2 show a 10 times higher J_{sc} compared with their counterpart with monolayer WS_2 on average.

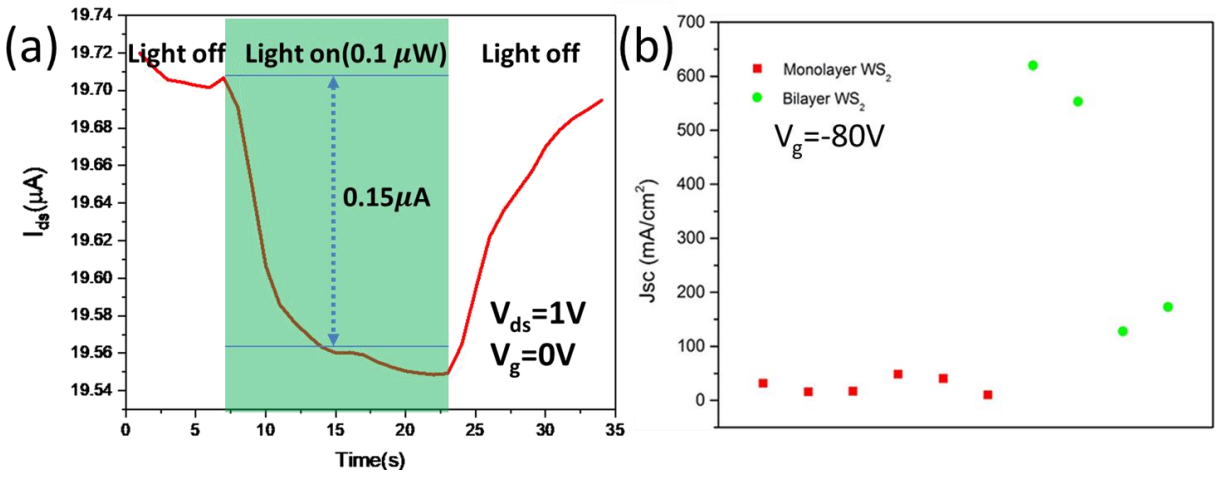

Figure A1. (a) Photoresponse of $Gr_B/WS_2(1L)/Gr_T$ photodetectors to green light. (V_{ds} = 1V, V_g = 0V, P_{opt} = 0.1μW, λ = 532nm) (b) Statistics of short-circuit current density of $Gr_B/WS_2(1L)/Gr_T$ (Red) and $Gr_B/WS_2(2L)/Gr_T$ (Green) devices illuminated with the same light power and under gate voltage at -80V.

Appendix B Supporting Information of Chapter 6

B.1. Optical microscope images of the Gr_B/TMD-HB/Gr_T

Figure B1 shows the optical images of the $Gr_B/WS_2(2L)/Gr_T$, $Gr_B/WS_2(1L)/MoS_2(1L)/Gr_T$, $Gr_B/MoS_2(1L)/WS_2(1L)/Gr_T$, $Gr_B/WS_2(1L)/Gr_T$, $Gr_B/MoS_2(1L)/Gr_T$ and $Gr_B/WS_2(2L)/MoS_2(1L)/Gr_T$ vertical heterostructures. The side view schematic diagrams are displayed right above the optical images to show the stacking sequence of the TMDs and graphene in the hetero-junction. In the optical images, the Gr_T and Gr_B are marked with white color, while the WS_2 and MoS_2 domains are marked with bluish and reddish colors, respectively. It is very clear that the widths of the graphene ribbons are not consistent in different stacks, it was due to the fabrication astigmatism problem. But this variation does not affect the photovoltaic results and discussions, as the laser spot size we used for photocurrent study is ~2μm, which is much smaller than even the narrowest ribbon we got in the experiment.

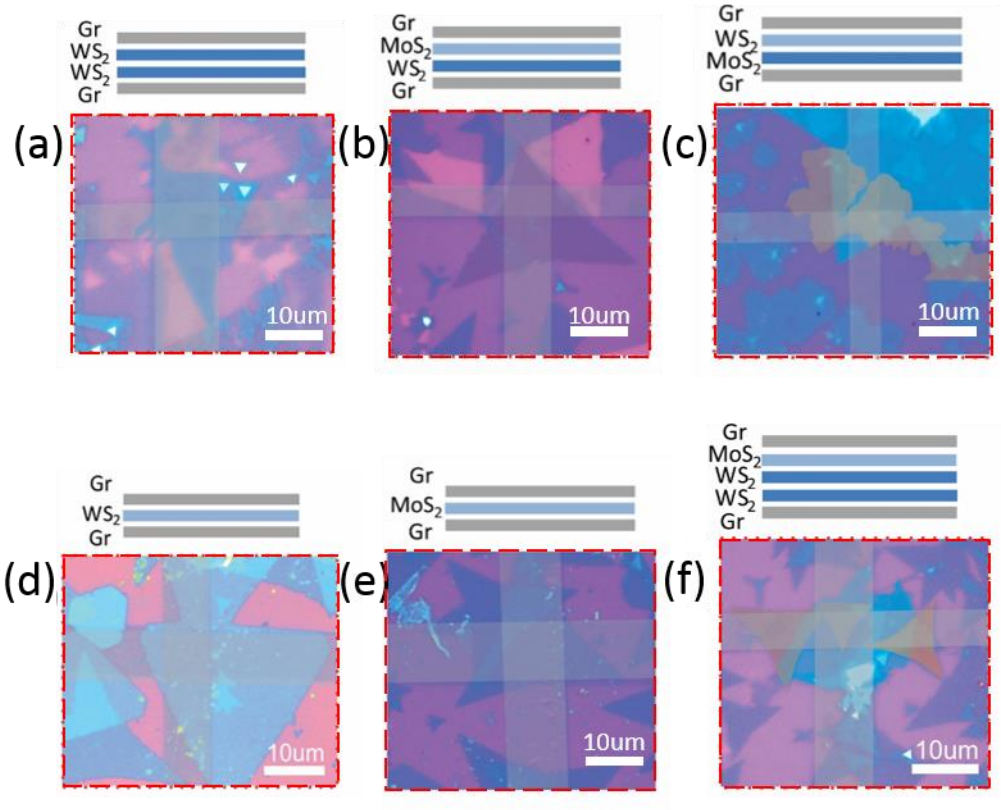

Figure B1. Optical microscope image of vertical stacked structures of (a) $Gr_B/WS_2(2L)/Gr_T$, (b) $Gr_B/WS_2(1L)/MoS_2(1L)/Gr_T$, (c) $Gr_B/MoS_2(1L)/WS_2(1L)/Gr_T$ (d) $Gr_B/WS_2(1L)/Gr_T$, (e) $Gr_B/MoS_2(1L)/Gr_T$ and (f) $Gr_B/WS_2(2L)/MoS_2(1L)/Gr_T$ and the corresponding schematic diagram to exhibit the stacking sequences.

Table B.1. Gr_B/TMD/Gr_T photodetectors, their short-circuit current and open-circuit voltage (number of samples, average, standard deviation, maximum value) statistics under ambient conditions (V_g = -60V, P_{opt} = 270μW, λ= 532nm).

Device structures	**$Gr_B/WS_2(2L)/Gr_T$**	**$Gr_B/WS_2/MoS_2/Gr_T$**	**$Gr_B/MoS_2/WS_2/Gr_T$**
Number of samples	1	4	4
Average$\|I_{sc}\|$[nA]	90	88	67
σ $\|I_{sc}\|$ [nA]	xxx	36	46
Max $\|I_{sc}\|$ [nA]	90	129	140
Average $\|V_{oc}\|$ [mV]	1.7	1.7	1.6
σ $\|V_{oc}\|$ [mV]	xxx	0.78	0.9
Max $\|V_{oc}\|$ [mV]	1.7	2.7	2.8

References

1. S. Das Sarma, S. Adam, E. H. Hwang, E. Rossi, Electronic transport in two-dimensional graphene. *Rev. Mod. Phys.* **83**, 407–470 (2011).
2. Q. H. Wang, K. Kalantar-Zadeh, A. Kis, J. N. Coleman, M. S. Strano, Electronics and optoelectronics of two-dimensional transition metal dichalcogenides. *Nat. Nanotechnol.* **7**, 699–712 (2012).
3. G. Zhang, Y.-W. Zhang, Thermal properties of two-dimensional materials. *Chinese Phys. B*. **26**, 34401 (2017).
4. R. Zhang, R. Cheung, in *Two-dimensional Mater. Charact. Potential Appl.* (IntechOpen, United Kingdom) 200–246 (2016).
5. K. Liu, J. Wu, Mechanical properties of two-dimensional materials and heterostructures. *J. Mater. Res.* **31**, 832–844 (2016).
6. Geim A, Novoselov K, The rise of graphene. *Nat. Mater.* **6**, 183–191 (2007).
7. P. Blake *et al.*, Graphene-based liquid crystal device. *Nano Lett*. **8**, 1704–1708 (2008).
8. Y. Xu, H. Bai, G. Lu, C. Li, G. Shi, Flexible graphene films via the filtration of water-soluble noncovalent functionalized graphene sheets. *J. Am. Chem. Soc*. **130**, 5856–5857 (2008).
9. M. F. El-Kady, Veronica Strong, S. Dubin, R. B. Kaner, Laser scribing of high-performance and flexible graphene-based electrochemical capacitors. *Science* **335**, 1326–1330 (2012).
10. J. D. Fowler *et al.*, Practical chemical sensors from chemically derived graphene. *ACS Nano* **3**, 301–306 (2009).
11. F. Schedin *et al.*, Detection of individual gas molecules adsorbed on graphene. *Nat. Mater.* **6**, 652–655 (2007).
12. S. H. Bae *et al.*, Graphene-based transparent strain sensor. *Carbon N. Y.* **51**, 236–242 (2013).
13. A. Sakhaee-Pour, M. T. Ahmadian, A. Vafai, Potential application of single-layered graphene sheet as strain sensor. *Solid State Commun.* **147**, 336–340 (2008).

14. F. Schwierz, Graphene transistors. *Nat. Nanotechnol.* **5**, 487–496 (2010).

15. A. H. Castro Neto, F. Guinea, N. M. R. Peres, K. S. Novoselov, A. K. Geim, The electronic properties of graphene. *Rev. Mod. Phys.* **81**, 109–162 (2009).

16. Y. Zhang *et al.*, Direct observation of a widely tunable bandgap in bilayer graphene. *Nature* **459**, 820–823 (2009).

17. M. Y. Han, B. Ozyilmaz, Y. Zhang, P. Kim, Energy band-gap engineering of graphene nanoribbons. *Phys. Rev. Lett.* **98**, 1–4 (2007).

18. S. Y. Zhou *et al.*, Substrate-induced band gap opening in epitaxial graphene. *Nat. Mater.* **6**, 770–775 (2007).

19. O. Lopez-Sanchez, D. Lembke, M. Kayci, A. Radenovic, A. Kis, Ultrasensitive photodetectors based on monolayer MoS_2. *Nat. Nanotechnol.* **8**, 497–501 (2013).

20. D. Kufer, G. Konstantatos, Highly sensitive, encapsulated MoS_2 photodetector with gate controllable gain and speed. *Nano Lett.* **15**, 7307-7313 (2015):

21. H. E. Sliney, Solid lubricant materials for high temperatures - a review. *Tribol. Int.* **15**, 303–315 (1982).

22. Y. Wang *et al.*, Strain-induced direct-indirect bandgap transition and phonon modulation in monolayer WS_2. *Nano Res.* **8**, 2562–2572 (2015).

23. A. L. Elías *et al.*, Controlled synthesis and transfer of large-area WS_2 sheets: from single layer to few layers. *ACS Nano* **7**, 5235–5242 (2013).

24. P. Avouris, Graphene: electronic and photonic properties and devices. *Nano Lett.* **10**, 4285–4294 (2010).

25. D. Reddy, L. F. Register, G. D. Carpenter, S. K. Banerjee, Graphene field-effect transistors. *J. Phys. D. Appl. Phys.* **44**, 313001 (2011).

26. P. Suvarnaphaet, S. Pechprasarn, Graphene-based materials for biosensors: A review. *Sensors* **17**, 2161 (2017).

27. F. Bonaccorso, Z. Sun, T. Hasan, A. C. Ferrari, Graphene photonics and optoelectronics. *Nat. Photonics* **4**, 611–622 (2010).

28. K. S. Novoselov *et al.*, Two-dimensional gas of massless Dirac fermions in graphene. *Nature* **438**, 197–200 (2005).

29. W. Zhu, V. Perebeinos, M. Freitag, P. Avouris, Carrier scattering, mobilities, and electrostatic potential in monolayer, bilayer, and trilayer graphene. *Phys. Rev. B - Condens. Matter Mater. Phys.* **80**, 1–8 (2009).

30. K. I. Bolotin *et al.*, Ultrahigh electron mobility in suspended graphene. *Solid State Commun.* **146**, 351–355 (2008).

31. J.-H. Chen, C. Jang, S. Xiao, M. Ishigami, M. S. Fuhrer, Intrinsic and extrinsic performance limits of graphene devices on SiO_2. *Nat. Nanotechnol.* **3**, 206–209 (2008).

32. C. R. Dean *et al.*, Boron nitride substrates for high-quality graphene electronics. *Nat. Nanotechnol.* **5**, 722–726 (2010).

33. J. Y. Hwang, C. C. Kuo, L. C. Chen, K. H. Chen, Correlating defect density with carrier mobility in large-scaled graphene films: Raman spectral signatures for the estimation of

defect density. *Nanotechnology* **21**,465705 (2010).

34. H. S. Song *et al.*, Origin of the relatively low transport mobility of graphene grown through chemical vapor deposition. *Sci. Rep.* **2**, 1–6 (2012).

35. R. R. Nair *et al.*, Fine structure constant defines visual transparency of graphene. *Science* **320**, 1308 (2008).

36. V. Thareja *et al.*, Electrically tunable coherent optical absorption in graphene with ion gel. *Nano Lett.* **15**, 1570–1576 (2015).

37. Q. Bao, K. P. Loh, Graphene photonics, plasmonics, and broadband optoelectronic devices, *ACS Nano* **6**, 3677–3694 (2012).

38. P. Blake *et al.*, Making graphene visible. *Appl. Phys. Lett.* **91**, 603124 (2007).

39. N. Liu *et al.*, Ultratransparent and stretchable graphene electrodes. *Sci. Adv.* **3**, e1700159 (2017).

40. G. Jo *et al.*, The application of graphene as electrodes in electrical and optical devices. *Nanotechnology* **23**, 112001 (2012).

41. P. Li *et al.*, Graphene-based transparent electrodes for hybrid solar cells. *Front. Mater.* **1**, 1–7 (2014).

42. K. Patel, P. K. Tyagi, Multilayer graphene as a transparent conducting electrode in silicon heterojunction solar cells. *AIP Adv.* **5**, 077165 (2015).

43. D. Song *et al.*, Unveiling pseudospin and angular momentum in photonic graphene. *Nat. Commun.* **6**, 1–7 (2015).

44. M. Chhowalla *et al.*, The chemistry of two-dimensional layered transition metal dichalcogenide nanosheets. *Nat. Chem.* **5**, 263–275 (2013).

45. B. Radisavljevic, A. Radenovic, J. Brivio, V. Giacometti, A. Kis, Single-layer MoS_2 transistors. *Nat. Nanotechnol.* **6**, 147–50 (2011).

46. Z. He, W. Que, Molybdenum disulfide nanomaterials: structures, properties, synthesis and recent progress on hydrogen evolution reaction. *Appl. Mater. Today* **3**, 23–56 (2016).

47. J. A. Wilson, A. D. Yoffe, The transition metal dichalcogenides discussion and interpretation of the observed optical, electrical and structural properties. *Adv. Phys.* **18**, 193–335 (1969).

48. D. Ovchinnikov, A. Allain, Y. S. Huang, D. Dumcenco, A. Kis, Electrical transport properties of single layer WS_2. *ACS Nano* **8**, 8174–8181 (2014).

49. P. C. Yeh *et al.*, Layer-dependent electronic structure of an atomically heavy two-dimensional dichalcogenide. *Phys. Rev. B - Condens. Matter Mater. Phys.* **91**, 1–6 (2015).

50. Y. Zhang *et al.*, Direct observation of the transition from indirect to direct bandgap in atomically thin epitaxial $MoSe_2$. *Nat. Nanotechnol.* **9**, 111–115 (2014).

51. I. G. Lezama *et al.*, Indirect-to-direct band gap crossover in few-layer $MoTe_2$. *Nano Lett.* **15**, 2336–2342 (2015).

52. A. Splendiani *et al.*, Emerging photoluminescence in monolayer MoS_2. *Nano Lett.* **10**, 1271–1275 (2010).

53. K. F. Mak, C. Lee, J. Hone, J. Shan, T. F. Heinz, Atomically thin MoS_2: a new direct-gap semiconductor. *Phys. Rev. Lett.* **105**, 136805 (2010).

54. Z. Y. Zhu, Y. C. Cheng, U. Schwingenschlögl, Giant spin-orbit-induced spin splitting in two-dimensional transition-metal dichalcogenide semiconductors. *Phys. Rev. B - Condens. Matter Mater. Phys.* **84**, 1–5 (2011).

55. J. A. Reyes-Retana, F. Cervantes-Sodi, Spin-orbital effects in metal-dichalcogenide semiconducting monolayers. *Sci. Rep.* **6**, 1–10 (2016).

56. K. Kaasbjerg, K. S. Thygesen, K. W. Jacobsen, Phonon-limited mobility in n-type single-layer MoS_2 from first principles. *Phys. Rev. B - Condens. Matter Mater. Phys.* **85**, 1–16 (2012).

57. B. Radisavljevic, A. Kis, Mobility engineering and a metal-insulator transition in monolayer MoS_2. *Nat. Mater.* **12**, 815–20 (2013).

58. S. Li, K. Wakabayashi, Y. Xu, S. Nakaharai, K. Komatsu, Thickness-dependent Interfacial coulomb scattering in atomically thin field-effect transistors. *Nano Lett.* **13**, 3546–3552 (2013).

59. X. Li *et al.*, Performance potential and limit of MoS_2 transistors. *Adv. Mater.* **29**, 1547–1552 (2015).

60. E. H. Hwang, S. Adam, S. Das Sarma, Carrier transport in two-dimensional graphene layers. *Phys. Rev. Lett.* **98**, 2–5 (2007).

61. S. Kim *et al.*, High-mobility and low-power thin-film transistors based on multilayer MoS_2 crystals. *Nat. Commun.* **3**, 1011 (2012).

62. S. A. Han, R. Bhatia, S.-W. Kim, Synthesis, properties and potential applications of two-dimensional transition metal dichalcogenides. *Nano Converg.* **2**, 17 (2015).

63. K. F. Mak, K. He, J. Shan, T. F. Heinz, Control of valley polarization in monolayer MoS_2 by optical helicity. *Nat. Nanotechnol.* **7**, 494–498 (2012).

64. T. Cheiwchanchamnangij, W. R. L. Lambrecht, Quasiparticle band structure calculation of monolayer, bilayer, and bulk MoS_2. *Phys. Rev. B - Condens. Matter Mater. Phys.* **85**, 1–4 (2012).

65. B. Zhu, X. Chen, X. Cui, Exciton binding energy of monolayer WS_2. *Sci. Rep.* **5**, 9218 (2014).

66. A. R. Klots *et al.*, Probing excitonic states in suspended two-dimensional semiconductors by photocurrent spectroscopy. *Sci. Rep.* **4**, 1–7 (2014).

67. A. Castellanos-Gomez, H. S. J. van der Zant, G. A. Steele, Folded MoS_2 layers with reduced interlayer coupling. *Nano Res.* **7**, 572–578 (2014).

68. J. Park *et al.*, Layer-modulated synthesis of uniform tungsten disulfide nanosheet using gas-phase precursors. *Nanoscale.* **7**, 1308–1313 (2015).

69. S. Mouri, Y. Miyauchi, K. Matsuda, Tunable photoluminescence of monolayer MoS_2 via chemical doping. *Nano Lett.* **13**, 5944–5948 (2013).

70. H. Nan *et al.*, Strong photoluminescence enhancement of MoS_2 through defect engineering and oxygen bonding. *ACS Nano* **8**, 5738–5745 (2014).

71. J. Gao *et al.*, Aging of transition metal dichalcogenide monolayer. *ACS Nano* **10**, 2628–

2635 (2016).

72. K. F. Mak *et al.*, Tightly bound trions in monolayer MoS_2, *Nat. Mater*. **12**, 207–211 (2013).

73. H. Zeng *et al.*, Photoluminescence emission and Raman response of monolayer MoS_2, $MoSe_2$, and WSe_2. *Sci. Rep.* **3**, 4908–4916 (2013).

74. A. Berkdemir *et al.*, Identification of individual and few layers of WS_2 using Raman spectroscopy. *Sci. Rep.* **3**, 1–8 (2013).

75. H. Zeng *et al.*, Optical signature of symmetry variations and spin-valley coupling in atomically thin tungsten dichalcogenides. *Sci. Rep*. **3**, 1608 (2013).

76. S. Sasaki *et al.*, Growth and optical properties of Nb-doped WS_2 monolayers. *Appl. Phys. Express* **9**, 71201 (2016).

77. L. Yuan, L. Huang, Exciton dynamics and annihilation in WS_2 2D semiconductors. *Nanoscale* **7**, 7402–7408 (2015).

78. K. Wei, Y. Liu, H. Yang, X. Cheng, T. Jiang, Large range modification of exciton species in monolayer WS_2. *Appl. Opt.* **55**, 6251 (2016).

79. S. Najmaei *et al.*, Vapour phase growth and grain boundary structure of molybdenum disulphide atomic layers. *Nat. Mater.* **12**, 754–9 (2013).

80. T. H. Ly *et al.*, Misorientation-angle-dependent electrical transport across molybdenum disulfide grain boundaries. *Nat. Commun.* **7**, 10426 (2016).

81. A. M. van der Zande *et al.*, Grains and grain boundaries in highly crystalline monolayer molybdenum disulphide. *Nat. Mater.* **12**, 554–61 (2013).

82. Y. L. Huang *et al.*, Bandgap tunability at single-layer molybdenum disulphide grain boundaries. *Nat. Commun.* **6**, 6298 (2015).

83. X. Zhou *et al.*, 2D Layered material-based van der Waals heterostructures for optoelectronics. *Adv. Funct. Mater.* **28**, 1–28 (2018).

84. W. J. Zhang, Q. X. Wang, Y. Chen, Z. Wang, A. T. S. Wee, Van der Waals stacked 2D layered materials for optoelectronics. *2D Mater.* **3**, 17 (2016).

85. X. Zhou *et al.*, Tunneling diode based on WSe_2/SnS_2 heterostructure incorporating high detectivity and responsivity. *Adv. Mater.* **30**, 1703286 (2018).

86. A. V. Kretinin *et al.*, Electronic properties of graphene encapsulated with different two-dimensional atomic crystals. *Nano Lett.* **14**, 3270–3276 (2014).

87. S. J. Haigh *et al.*, Cross-sectional imaging of individual layers and buried interfaces of graphene-based heterostructures and superlattices. *Nat. Mater.* **11**, 764–767 (2012).

88. C. R. Woods *et al.*, Commensurate-incommensurate transition in graphene on hexagonal boron nitride. *Nat. Phys.* **10**, 451–456 (2014).

89. C. Zhang *et al.*, Interlayer couplings, Moiré patterns, and 2D electronic superlattices in MoS_2/WSe_2 hetero-bilayers. *Sci. Adv.* **3**, 1–8 (2017).

90. N. Huo *et al.*, Novel optical and electrical transport properties in atomically thin WSe_2/MoS_2 p-n heterostructures. *Adv. Electron. Mater.* **1**, 1–7 (2015).

91. J. C. W. Song, A. V. Shytov, L. S. Levitov, Electron interactions and gap opening in graphene superlattices. *Phys. Rev. Lett.* **111**, 1–5 (2013).

92. C.-H. H. Lee *et al.*, Atomically thin p-n junctions with van der Waals heterointerfaces. *Nat. Nanotechnol.* **9**, 676–681 (2014).

93. A. Nourbakhsh, A. Zubair, M. S. Dresselhaus, T. Palacios, Transport properties of a MoS_2/WSe_2 heterojunction transistor and its potential for application. *Nano Lett.* **16**, 1359–1366 (2016).

94. M. Buscema, G. a. Steele, H. S. J. van der Zant, A. Castellanos-Gomez, The effect of the substrate on the Raman and photoluminescence emission of single-layer MoS_2. *Nano Res.* **7**, 561–571 (2014).

95. J. Kang, S. Tongay, J. Zhou, J. Li, J. Wu, Band offsets and heterostructures of two-dimensional semiconductors. *Appl. Phys. Lett.* **102**, 012111 (2013).

96. S. Tongay *et al.*, Tuning interlayer coupling in large-area heterostructures with CVD-grown MoS_2 and WS_2 monolayers. *Nano Lett.* **14**, 3185–3190 (2014).

97. P. Rivera *et al.*, Observation of long-lived interlayer excitons in monolayer $MoSe_2$-WSe_2 heterostructures. *Nat. Commun.* **6**, 4–9 (2015).

98. X. Hong *et al.*, Ultrafast charge transfer in atomically thin MoS_2/WS_2 heterostructures. *Nat. Nanotechnol.* **9**, 682–686 (2014).

99. H. Tan *et al.*, Doping graphene transistors using vertical stacked monolayer WS_2 heterostructures grown by chemical vapor deposition. *ACS Appl. Mater. Interfaces*. **8**, 1644–1652 (2016).

100. H. Fang *et al.*, Strong interlayer coupling in van der Waals heterostructures built from single-layer chalcogenides. *Proc. Natl. Acad. Sci.* **111**, 6198–6202 (2014).

101. N. B. Mohamed *et al.*, Long radiative lifetimes of excitons in monolayer transition-metal dichalcogenides MX_2 (M=Mo, W; X=S, Se). *Appl. Phys. Express* **11**, 15201 (2018).

102. K. S. Novoselov, A. Mishchenko, A. Carvalho, A. H. Castro Neto, 2D materials and van der Waals heterostructures. *Science* **353**, aac9439 (2016).

103. H. Qiu *et al.*, Electrical characterization of back-gated bi-layer MoS_2 field-effect transistors and the effect of ambient on their performances. *Appl. Phys. Lett.* **100**, 123104 (2012).

104. D. Braga, I. Gutie, H. Berger, A. F. Morpurgo, Quantitative determination of the band gap of WS_2 with ambipolar ionic liquid gated transistors. *Nano Lett.* **12**, 5218–5223 (2012).

105. W. Bao, X. Cai, D. Kim, K. Sridhara, M. S. Fuhrer, High mobility ambipolar MoS_2 field-effect transistors: substrate and dielectric effects. *Appl. Phys. Lett.* **102**, 42104 (2013).

106. S. Das, H. Y. Chen, A. V. Penumatcha, J. Appenzeller, high performance multilayer MoS_2 transistors with scandium contacts. *Nano Lett.* **13**, 100–105 (2013).

107. Y. Liu *et al.*, Toward barrier free contact to molybdenum disulfide using graphene electrodes. *Nano Lett.* **15**, 3030–3034 (2015).

108. H. Schmidt *et al.*, Transport properties of monolayer MoS_2 grown by chemical vapour deposition. *Nano Lett*. **4**, 1909–1913 (2014).

109. G. H. Lee *et al.*, Highly stable, dual-gated MoS_2 transistors encapsulated by hexagonal boron nitride with gate-controllable contact, resistance, and threshold voltage. *ACS Nano*. **9**, 7019–7026 (2015).

110. T. Georgiou *et al.*, Field-effect tunneling transistor based on vertical graphene heterostructures. *Science* **335**, 947–950 (2012).

111. T. Georgiou *et al.*, Vertical field-effect transistor based on graphene-WS_2 heterostructures for flexible and transparent electronics. *Nat. Nanotechnol.* **8**, 100–103 (2012).

112. R. Cheng *et al.*, Electroluminescence and photocurrent generation from atomically sharp WSe_2/MoS_2 heterojunction p-n diodes. *Nano Lett.* **14**, 5590–5597 (2014).

113. T. Roy *et al.*, Dual-gated MoS_2/WSe_2 van der Waals tunnel diodes and transistors. *ACS Nano* **9**, 2071–2079 (2015).

114. T. Roy *et al.*, 2D-2D tunneling field-effect transistors using WSe_2 /$SnSe_2$ heterostructures. *Appl. Phys. Lett.* **108**, 83111 (2016).

115. H. Tan *et al.*, Lateral graphene-contacted vertically stacked WS_2/MoS_2 hybrid photodetectors with large gain. *Adv. Mater.* **29**, 1–8 (2017).

116. L. Britnell *et al.*, Strong light-matter Interactions in heterostructures of atomically thin films. *Science* **340**, 1311–1314 (2013).

117. M. C. Lemme *et al.*, Gate-activated photoresponse in a graphene p-n junction. *Nano Lett.* **11**, 4134–4137 (2011).

118. M. Massicotte *et al.*, Photo-thermionic effect in vertical graphene heterostructures. *Nat. Commun.* **7**, 1–7 (2016).

119. R. Yan *et al.*, Esaki diodes in van der Waals heterojunctions with broken-gap energy band alignment. *Nano Lett.* **15**, 5791–5798 (2015).

120. Q. A. Vu *et al.*, Tuning carrier tunneling in van der Waals heterostructures for ultrahigh detectivity. *Nano Lett.* **17**, 453–459 (2017).

121. W. J. Yu *et al.*, Unusually efficient photocurrent extraction in monolayer van der Waals heterostructure by tunnelling through discretized barriers. *Nat. Commun.* **7**, 13278 (2016).

122. Y.-H. Lee *et al.*, Synthesis of large-area MoS_2 atomic layers with chemical vapor deposition. *Adv. Mater.* **24**, 2320–2325 (2012).

123. Y. Gong *et al.*, Vertical and in-plane heterostructures from WS_2/MoS_2 monolayers. *Nat. Mater.* **13**, 1135 (2014).

124. Y. Gong *et al.*, Two-step growth of two-ddimensional $WSe_2/MoSe_2$ heterostructures. *Nano Lett.* **15**, 6135–6141 (2015).

125. Y. Liu *et al.*, Van der Waals heterostructures and devices. *Nat. Rev. Mater.* **1**, 16042 (2016).

126. N. Huo *et al.*, Novel and enhanced optoelectronic performances of multilayer MoS_2-WS_2 heterostructure transistors. *Adv. Funct. Mater.* **24**, 7025–7031 (2014).

127. K. Wang *et al.*, Interlayer coupling in twisted WSe_2/WS_2 bilayer heterostructures revealed by optical spectroscopy. *ACS Nano* **10**, 6612–6622 (2016).

128. B. I. Yakobson, N. Alem, G. Stone, M. Terrones, Dislocation motion and grain boundary migration in two- dimensional tungsten disulphide. *Nat. Commun*. **5**, 4867 (2014).

129. Y. Rong *et al.*, Controlling sulphur precursor addition for large single crystal domains of WS_2. *Nanoscale* **6**, 12096–12103 (2014).

130. S. Wang *et al.*, Shape evolution of monolayer MoS_2 crystals grown by chemical vapor deposition. *Chem. Mater.* **26**, 6371–6379 (2014).

131. Y. Rong *et al.*, Controlled preferential xxidation of grain boundaries in monolayer tungsten disulfide for direct optical imaging. *ACS Nano* **9**, 3695–3703 (2015).

132. Y. Chang *et al.*, Monolayer $MoSe_2$ grown by chemical vapor deposition for fast photodetection. *ACS Nano* **8**, 8582–8590 (2014).

133. E. Scalise, M. Houssa, G. Pourtois, V. Afanasev, A. Stesmans, Strain-induced semiconductor to metal transition in the two-dimensional honeycomb structure of MoS_2. *Nano Res.* **5**, 43–48 (2012).

134. V. Q. Bui, T.-T. Pham, D. A. Le, C. M. Thi, H. M. Le, A first-principles investigation of various gas (CO, H_2O, NO, and O_2) absorptions on a WS_2 monolayer: stability and electronic properties. *J. Phys. Condens. Matter*. **27**, 305005 (2015).

135. N. Huo *et al.*, Photoresponsive and gas sensing field-effect transistors based on multilayer WS_2 nanoflakes. *Sci. Rep.* **4**, 5209 (2014).

136. A. S. Mcdonnell, R. Addou, R. M. Wallace, C. L. Hinkle, Defect dominated doping and contact resistance in MoS_2. *ACS Nano* **8**, 2880–2888 (2014).

137. O. F. Siebel, M. C. Schneider, C. Galup-Montoro, MOSFET threshold voltage: definition, extraction, and some applications. *Microelectronics J.* **43**, 329–336 (2012).

138. Y. A. Wu *et al.*, Large single crystals of graphene on melted copper using chemical vapor deposition. *ACS Nano* **6**, 5010–5017 (2012).

139. H. Tan *et al.*, Ultrathin 2D photodetectors utilizing chemical vapor deposition grown WS_2 with graphene electrodes. *ACS Nano* **10**, 7866–7873 (2016).

140. Z. He *et al.*, Biexciton formation in bilayer tungsten disulfide. *ACS Nano* **10**, 2176–2183 (2016).

141. N. Huo *et al.*, Interlayer coupling and optoelectronic properties of ultrathin two-dimensional heterostructures based on graphene, MoS_2 and WS_2. *J. Mater. Chem. C*. **3**, 5467–5473 (2015).

142. H.-Y. Y. Chiu, V. Perebeinos, Y.-M. M. Lin, P. Avouris, Controllable p-n junction formation in monolayer graphene using electrostatic substrate engineering. *Nano Lett.* **10**, 4634–9 (2010).

143. S. Ryu *et al.*, Atmospheric oxygen binding and hole doping in deformed graphene on a SiO_2 substrate. *Nano Lett.* **10**, 4944–4951 (2010).

144. J. M. Beebe, B. Kim, J. W. Gadzuk, C. D. Frisbie, J. G. Kushmerick, Transition from direct tunneling to field emission in metal-molecule-metal junctions. *Phys. Rev. Lett.* **97**, 1–4 (2006).

145. W. Zhang *et al.*, Ultrahigh-gain photodetectors based on atomically thin graphene-MoS_2 heterostructures. *Sci. Rep.* **4**, 3826 (2014).

146. M. Bernardi, M. Palummo, J. C. Grossman, Extraordinary sunlight absorption and one nanometer thick photovoltaics using two-dimensional monolayer materials. *Nano Lett.* **13**, 3664–3670 (2013).

147. Gabor, N. M. et al. Hot carrier–assisted intrinsic photoresponse in graphene. *Science* **334**, 648–652 (2011).

148. X. Xu, N. M. Gabor, J. S. Alden, A. M. Van Der Zande, P. L. McEuen, Photo-thermoelectric effect at a graphene interface junction. *Nano Lett.* **10**, 562–566 (2010).

149. P. Steinleitner *et al.*, Direct observation of ultrafast exciton formation in a monolayer of WSe_2. *Nano Lett.* **17**, 1455–1460 (2017).

150. F. Ceballos, Q. Cui, M. Z. Bellus, H. Zhao, Exciton formation in monolayer transition metal dichalcogenides. *Nanoscale* **8**, 11681–11688 (2016).

151. Z. Ye *et al.*, Probing excitonic dark states in single-layer tungsten disulphide. *Nature* **513**, 214–218 (2014).

152. Y. Guo *et al.*, Probing the dynamics of the metallic-to-semiconducting structural phase transformation in MoS_2 crystals. *Nano Lett.* **15**, 5081–5088 (2015).

153. Z. He *et al.*, Layer-dependent modulation of tungsten disulfide photoluminescence by lateral electric fields. *ACS Nano* **9**, 2740–2748 (2015).

154. T. Borzda *et al.*, Charge photogeneration in few-layer MoS_2. *Adv. Funct. Mater.* **25**, 3351–3358 (2015).

155. T. Chu, H. Ilatikhameneh, G. Klimeck, R. Rahman, Z. Chen, Electrically tunable bandgaps in bilayer MoS_2. *Nano Lett.* **15**, 8000–8007 (2015).

156. D. H. Luong *et al.*, Tunneling photocurrent assisted by interlayer excitons in staggered van der Waals hetero-bilayers. *Adv. Mater.* **29**, 1701512 (2017).

157. D. Azhikodan, T. Nautiyal, S. Shallcross, S. Sharma, An anomalous interlayer exciton in MoS_2. *Sci. Rep.* **6**, 37075 (2016).

158. Y. Zhou *et al.*, Utilizing interlayer excitons in bilayer WS_2 for increased photovoltaic response in ultrathin graphene vertical cross-bar photodetecting tunneling transistors. *ACS Nano* **12**, 4669–4677 (2018).

159. Y. Xue *et al.*, Scalable production of a few-layer MoS_2/WS_2 vertical heterojunction array and its application for photodetectors. *ACS Nano* **10**, 573–580 (2015).

160. A. J. Cho, S. D. Namgung, H. Kim, J. Y. Kwon, Electric and photovoltaic characteristics of a multi-layer $ReS_2/ReSe_2$ heterostructure. *APL Mater.* **5**, 076101 (2017).

161. M. M. Furchi, A. Pospischil, F. Libisch, J. Burgdörfer, T. Mueller, Photovoltaic effect in an electrically tunable van der Waals heterojunction. *Nano Lett.* **14**, 4785–4791 (2014).

162. J. He *et al.*, Electron transfer and coupling in graphene-tungsten disulfide van der Waals heterostructures. *Nat. Commun.* **5**, 5622 (2014).

163. C. Gong *et al.*, Band alignment of two-dimensional transition metal dichalcogenides: Application in tunnel field effect transistors. *Appl. Phys. Lett.* **103**, 053513 (2013),.

164. W. Li *et al.*, Electric field modulation of the band structure in MoS_2/WS_2 van der Waals heterostructure. *Solid State Commun.* **250**, 9–13 (2017).

165. G. Konstantatos *et al.*, Hybrid graphene quantum dot phototransistors with ultrahigh gain. *Nat. Nanotechnol.* **7**, 363–368 (2012).

166. M. M. Furchi, D. K. Polyushkin, A. Pospischil, T. Mueller, Mechanism of photoconductivity in atomically thin MoS_2. *Nano Lett*. **14**, 6165–6170 (2014).

167. L. Zhong *et al*., Defect engineering of two-dimensional transition metal dichalcogenides. *2D Materials* **3(2***)*, 022002 (2016).